



THE UNIVERSITY OF
WAIKATO
Te Whare Wānanga o Waikato

Research Commons

<http://waikato.researchgateway.ac.nz/>

Research Commons at the University of Waikato

Copyright Statement:

The digital copy of this thesis is protected by the Copyright Act 1994 (New Zealand).

The thesis may be consulted by you, provided you comply with the provisions of the Act and the following conditions of use:

- Any use you make of these documents or images must be for research or private study purposes only, and you may not make them available to any other person.
- Authors control the copyright of their thesis. You will recognise the author's right to be identified as the author of the thesis, and due acknowledgement will be made to the author where appropriate.
- You will obtain the author's permission before publishing any material from the thesis.

Wavelength Tuneable Frequency Domain Photon Migration Spectrometer for Tissue-like Media

A thesis submitted for the
degree of

Doctor of Philosophy

at

The University of Waikato

by

BIJU CLETUS



THE UNIVERSITY OF
WAIKATO
Te Whare Wānanga o Waikato

May 2010

Abstract

Frequency domain spectrometers use intensity modulated light to quantitatively interrogate turbid media. The modulation frequencies employed are in the radiofrequency range. Intensity modulated light launched into a turbid medium generates photon density fluctuations with wave like character that oscillates at the modulation frequency. These density fluctuations are named diffuse photon density waves, and it has been shown that the amplitude and phase of the photon density wave inside the medium depends on its optical properties. Hence by measuring the amplitude and phase of the photon density wave the optical properties of the medium can be estimated. This is the basic working principle of a frequency domain photon migration spectrometer.

Frequency domain spectrometers fabricated with laser diodes are limited to discrete wavelengths thereby making compromises on the information about the media under test. In this research a wavelength tuneable frequency domain spectrometer was constructed by modulating the output intensity of a titanium: sapphire laser using an acousto-optic modulator. A low noise avalanche photodiode module in conjunction with a lock-in amplifier was used to measure the amplitude attenuation and phase lag inside a turbid sample. The frequency domain spectrometer was tested for accuracy and precision by estimating the optical properties of an important tissue simulation phantom, Intralipid®, at a representative wavelength 790 nm. The results indicated that the spectrometer estimates absorption with an accuracy of 10%. The instrument estimates the absorption and reduced scattering coefficients with a precision of 3% and 6%, respectively.

Optical properties of Intralipid® were measured from 710-850 nm in the therapeutic window. The results were compared with published data

measured by other methods and similar frequency domain techniques. The absorption coefficient agrees within 10% with results from a time domain measurement. The reduced scattering coefficient was within the error limits of other reported measurements. At 750 nm the reduced scattering agrees within 5% with the results from a continuous wave, time domain and within 1% from another frequency domain measurement, and at 811 and 849 nm this agreement is within 9%. A Mie theory prediction of the reduced scattering coefficient based on a measurement of the particle size distribution by a Mastersizer 2000 is larger than the frequency domain results by 6%.

The spectrometer was used to determine the optical temperature coefficient of Intralipid®, exploring its potential as a non invasive temperature monitoring device. The measured minute change in the absorption coefficient suggests a minimum observable temperature change of $\pm 4^{\circ}\text{C}$, which for most practical applications means that the precision needs to improve. The effect of glucose on the optical properties of Intralipid® indicates that the absorption coefficient decreases steadily at 730 nm up to 1000mg/dL. The reduced scattering coefficient decreases with increasing glucose concentration at most of the wavelengths.

This work quantified the absorption and reduced scattering of Intralipid® over a larger wavelength range (in the therapeutic window) than before. This is the first time the effects of temperature on the optical properties of a turbid medium monitored with a frequency domain spectrometer. Specific information about the precision and accuracy which can be achieved with the current technology is documented. Current precision is not sufficient for many applications that would benefit from separation of absorption and scattering.

Acknowledgements

I am deeply indebted to my supervisors Assoc. Prof. Rainer Künnemeyer and Dr. Paul Martinsen (Scientist, HortResearch) for their guidance, never-ending encouragement and enthusiasm. I am grateful for your extraordinary kindness, patience, support and above all for imparting knowledge. You were more than supervisors right from the very beginning. I could not have wished for better supervisors.

I would also like to thank HortResearch Scientists, Dr. Andrew McGlone and Dr. Robert Jordan for their support and encouragement during the research.

I would like to thank Nihal Kularatna, Senior Lecturer, Department of Engineering for the encouragement during the research.

I would like to express my sincere thanks to technical officers Stewart Finlay and Pawan Shrestha, at the Department of Engineering, for the support from the very beginning of the research.

The help from technical staff at HortResearch is also greatly acknowledged.

I would like to thank University of Waikato for the doctoral scholarship and HortResearch for letting me use their facilities and providing financial support for the research.

Finally to my parents and in-laws, thank you for your love, support and prayers throughout the years. To my dearest daughter Belcita, thank you for your big smiles and words of affection that kept me cheerful throughout this work and my wife Anila, you always stood beside me with love and respect that have led me to where I am.

Contents

Contents	7
LIST OF FIGURES.....	11
CHAPTER 1 INTRODUCTION.....	17
CHAPTER 2 LIGHT TRANSPORT IN TURBID MEDIA	21
2.1 Introduction	21
2.2 Transparent versus turbid samples	21
2.3 Light propagation models	24
2.3.1 Mie theory	24
2.3.2 Kubelka-Munk theory	25
2.3.3 Monte Carlo simulations	26
2.3.4 Finite element method	28
2.4 Radiative transport equation	29
2.4.1 Diffusion approximation.....	33
2.4.2 Diffusion coefficient	35
2.4.3 Frequency-domain solution to diffusion equation	36
2.4.4 Multi frequency measurements	43
2.4.5 Multi distance measurements.....	44
2.4.6 Accuracy of results obtained from diffusion approximation ...	46
2.5 Therapeutic window and typical optical property values	49
2.6 Tissue simulation phantoms.....	50
2.7 Summary.....	53
CHAPTER 3 PHOTON MIGRATION INSTRUMENTATION	55
3.1 Introduction	55
3.2 Continuous intensity measurements.....	57
3.3 Time domain measurements.....	65
3.4 Frequency domain measurements	74
3.4.1 Modulation.....	75
3.4.2 Detection.....	79
3.5 Reported instrumentation	84
3.6 Combination of instrumentations	93
3.7 Summary.....	95
CHAPTER 4 FREQUENCY DOMAIN SPECTROMETER	97

4.1	Introduction.....	97
4.2	Experiment setup.....	97
4.3	Light source	100
4.4	Acousto-optic modulator	103
4.5	Avalanche photodiode module and detection electronics	105
4.6	Performance testing	106
4.6.1	Phase and amplitude variation after acousto-optic modulator 106	
4.6.2	Detected signal.....	108
4.6.3	Phase and amplitude measurements	110
4.6.4	Phase-amplitude crosstalk.....	112
4.6.5	Accuracy and precision.....	115
4.7	Summary	119
CHAPTER 5 OPTICAL PROPERTIES OF INTRALIPID®.....		121
5.1	Introduction.....	121
5.2	Method	121
5.4	Amplitude and phase measurements	123
5.5	Intralipid particle size measurements.....	124
5.6	Absorption and reduced scattering coefficient estimation	125
5.7	Validating optical property measurements.....	128
5.8	Influence of glucose on the optical properties of Intralipid.....	135
5.8.1	Method	135
5.8.2	Influence on absorption.....	136
5.8.3	Influence on reduced scattering	137
5.8.4	Possibility of glucose monitoring in turbid media.....	138
5.9	Summary	140
CHAPTER 6 TEMPERATURE DEPENDENCE OF OPTICAL PROPERTIES OF INTRALIPID®		143
6.1	Introduction.....	143
6.2	Method	143
6.3	Optical property temperature dependence.....	145
6.4	Optical temperature coefficients	150
6.5	Summary	155
CHAPTER 7 CONCLUSION & FUTURE WORK		157
APPENDIX I.....		161
	Calculation of error in optical properties	161

APPENDIX II LabView Codes	163
LabView code for lock-in Amplifier	163
LabView front panel - translation stage	164
Temperature control VI	165
MATLAB Codes	166
Matlab code running the FDPM Spectrometer	166
Function connecting the translation stage	168
Function connecting lock-in amplifier	168
Function to move the translation stage	168
Function to get data out of lock-in amplifier	168
Function to disconnect translation stage	169
Function to close connection to lock-in amplifier	169
Code monitoring the temperature effects on optical properties	169
Function connecting the temperature control	170
Function to collect measurements	170
Function to change solution temperature	171
Function to calculate optical properties	171
APPENDIX III	173
Mathcad-Intralipid® Mie scattering	173
REFERENCES	181

LIST OF FIGURES

Figure 1 Optical processes in an (a) absorbing and (b) scattering media.	22
Figure 2 Light scattering by a particle with radius, a , and refractive index n' embedded in a medium with refractive index n .	24
Figure 3 Cylindrical differential volume element of the medium along photon propagation direction.	31
Figure 4 Photon density wave generated (concentric semi-circles) inside a turbid medium by intensity modulated light.	37
Figure 5 Wavelength of photon density waves plotted against modulation frequency for a medium with three different reduced scattering coefficients.	38
Figure 6 Time evolution of intensity modulated light illustrates the measurable quantities in the frequency domain.	39
Figure 7 Variation of modulation depth against source-detector separation for modulation frequencies of 50 and 100 MHz. The plot illustrates the effect of absorption of the medium on modulation. The dashed line correspond to a medium with absorption coefficient 0.1 cm^{-1} and the solid line to a medium with absorption 0.02 cm^{-1} , both having the same reduced scattering coefficient.	41
Figure 8 Phase variation plotted against source detector separation. The dotted and solid lines correspond to medium with different absorption coefficient and same reduced scattering coefficient.	43
Figure 9 Infinite (a) and semi infinite (b) medium geometries in photon migration measurements.	46
Figure 10 Source and image geometry for partial current and extrapolated boundary approach taken from Haskell et al. (1994).	47
Figure 11 Absorption spectra of haemoglobin, oxy-haemoglobin (Prahl 1998) and water (Hale and Querry 1973) plotted against wavelength.	49
Figure 12 Absorption (a) and reduced scattering (b) coefficients of some fruits and vegetables plotted against wavelength (Qin and Lu 2008).	50
Figure 13 Absorption coefficients of two major components of Intralipid, water (Kou et al. 1993) and soybean oil (Hollis 2002), plotted against wavelength.	52
Figure 14 Photon migration instrument.	55
Figure 15 Continuous intensity measurements.	57

List of Figures

Figure 16 Fibre probes, (a) and (b), used by Bays et al. (1996) to make optical property measurements; (b) is similar to fibre probes used in photodynamic therapy (reproduced).	59
Figure 17 Fibre probe used by Nichols et al. (1997) for optical property measurement (reproduced).	60
Figure 18 Fibre probe geometry used by Bevilacqua et al. (1999) to make optical property measurements.	62
Figure 19 A short light pulse propagating through a scattering medium spreading into ballistic, snakelike and diffuse photons.	66
Figure 20 Time resolved instrumentation reported by Andersson-Engels et al. (1993) (reproduced).	68
Figure 21 Schematic diagram of time resolved transmittance measurement by Brewster and Yamada (1995).	69
Figure 22 Principle of time correlated single photon counting (Becker et al. 2004).	70
Figure 23 Schematic diagram of acousto optic modulator operating in the Bragg regime (ISOMET Corporation).	77
Figure 24 Schematic diagram of photomultiplier tube.	80
Figure 25 Block diagram of heterodyne detection system reported by Fishkin et al. (1996).	83
Figure 26 Frequency domain spectrophotometer reported by Fishkin et al. (1996) (reproduced).	88
Figure 27 Schematic diagram of the constructed frequency domain photon migration spectrometer.	97
Figure 28 Photograph and schematic diagram of the acousto-optic modulator used in the experiment setup with focusing lens and fibre coupling mechanism.	99
Figure 29 Laser system Coherent Verdi-V5 with biasing electronics for the diode array (Verdi-V5).	100
Figure 30 Laser head optical schematic of Nd:YVO ₄ .	101
Figure 31 The output power variation of titanium-sapphire laser plotted against wavelength (Palmer 2003).	102
Figure 32 Schematics of titanium sapphire laser cavity.	102
Figure 33 Acousto optic modulator and the fixed frequency driver (reproduced from Brimrose, USA, product catalogue).	104
Figure 34 Block diagram of avalanche photodiode module (reproduced from APD MODULE C5331, Instruction Manual, Hamamatsu Photonics K.K.).	105
Figure 35 Experiment setup to monitor phase variation across the modulated beam.	107

Figure 36	Variation of intensity and phase of the modulated beam measured at a distance of 15 cm from the output aperture of the acousto-optic modulator.	108
Figure 37	Frequency spectrum of detected signal at two optode separations (a) 10 mm, (b) 30 mm and (c) indicates the first harmonic. This corresponds to a typical scan of the optode from 10 to 30 mm at a source modulation frequency of 50 MHz.	109
Figure 38	AC amplitude (a) and phase (b) of photon density wave measured by the lock-in amplifier plotted against source-detector separation.	110
Figure 39	Amplitude and phase variation measured and predicted by theory. Simulated based on equations 27 and 28 for a medium with absorption 0.024 cm^{-1} and reduced scattering 16 cm^{-1} at a source modulation frequency of 50 MHz.	111
Figure 40	(a) Logarithm of AC amplitude multiplied by source detector separation plotted against source detector separation. (b) Phase in radian plotted against source detector separation. The subplot shows the residuals for a linear regression to the amplitude and phase data.	111
Figure 41	Experiment setup to measure phase amplitude crosstalk. The variable neutral density filter was rotated to make phase and amplitude measurements from the sample keeping the source and detector fixed.	113
Figure 42	Phase plotted against amplitude attenuation at three source detector separations. The laser power is attenuated by rotating the neutral density filter at fixed source detector separation. The error bars represent ± 1 standard deviation.	114
Figure 43	Room temperature variation inside the lab monitored using a thermocouple thermometer (Fluke 52 II, Fluke Corporation, USA) with airconditioner operating.	115
Figure 44	Effect of room temperature variation on the amplitude and phase measurements made by the lock-in amplifier. The line indicates a change in room temperature due to turning the air conditioner on.	116
Figure 45	Amplitude and phase of the modulation measured over a 10 minute period by the locin amplifier. These measurements were made by placing the source and detector fibres facing each other in air. The second subplot shows the direct unmodulated source power measured by a power meter.	117
Figure 46	Five repeated measurements of (a) absorption and (b) reduced scattering coefficients made at 790 nm at source modulation frequency 50 MHz. The error bars represent standard deviation for 10 repeated measurements of amplitude and phase corresponding to each data point.	118
Figure 47	Intralipid 20% bottle along with the sample container setup.	121
Figure 48	Complete experimental setup.	122

- Figure 49 Amplitude (a) and phase (b) data recorded by the lock-in amplifier are plotted against source detector separation. These data corresponds to a wavelength of 750 nm at five different Intralipid concentrations. 123
- Figure 50 (a) Logarithm of source-detector separation times normalized AC amplitude and (b) normalized phase variation versus source-detector separations at 750 nm for five Intralipid concentrations. 124
- Figure 51 Volume fraction of Intralipid 20% particles measured with a Mastersizer 2000. This distribution is used in our Mie theory calculations. Data by van Staveren et al. (van Staveren et al. 1991), converted to volume fraction, are included for comparison. 125
- Figure 52 Absorption coefficient of Intralipid. Data reported by Piffery et al. (Pifferi et al. 2007) are included for comparison. The error bars indicate 95% confidence interval. 126
- Figure 53 Reduced scattering coefficient of Intralipid. The solid lines correspond to Mie theory estimates, based on our particle size measurements, for 0.95, 2.59 and 4.0% lipid concentration. The error bars indicate 95% confidence interval. 127
- Figure 54 Difference between reduced scattering estimated by Mie theory and frequency domain measurements plotted against wavelength. 128
- Figure 55 Absorption coefficient of Intralipid at 750 nm plotted against water concentration along with literature data. The dotted lines indicate 95% confidence interval for the linear fit. 129
- Figure 56 Discrepancy between extrapolated absorption at a water concentration equivalent to 0.53% Intralipid absorption reported by Pifferi et al. (2007) plotted against wavelength. 129
- Figure 57 Extrapolated absorption coefficient (triangular markers with error bars) for water from Intralipid measurements versus wavelength. The solid curve represents water absorption data reported by Kou et al.(1993). The error bars correspond to ± 2 standard deviations. 130
- Figure 58 Discrepancy between extrapolated water absorption from our measurements and the pure water absorption data reported by Kou et al. (1993) plotted against wavelength. 131
- Figure 59 Reduced scattering coefficient at 750 nm versus Intralipid concentration. The error bars indicate 95% confidence intervals. The solid line is a linear fit to the experimental data. The dashed line shows the Mie theory results. 132
- Figure 60 Reduced scattering coefficient (triangular markers with error bars) values for a 2% solution of Intralipid plotted against wavelength. The solid line corresponds to the Mie theory values calculated based on our particle size measurement. Data reported at 750 nm is staggered a little to make them visible. The error bars indicate 95% confidence interval. 134
- Figure 61 Calculated absorption coefficient of Intralipid with high concentrations of glucose solution. 136

Figure 62 Reduced scattering coefficients of Intralipid at higher glucose concentrations plotted against wavelength.	137
Figure 63 Absorption coefficient estimated at 730 nm plotted against glucose concentration in Intralipid. The red line corresponds to a linear fit to the data . The dotted line indicates 95% confidence interval for the fit.	138
Figure 64 Absorption coefficient estimated at higher concentrations (magenta data points) plotted against concentration. The linear fit does not include the magenta data points.	139
Figure 65 The setup measuring temperature dependence of optical properties of Intralipid. The photograph demonstrates the careful arrangement to prevent water evaporation during heating the Intralipid solution.	144
Figure 66 Absorption coefficient at 22°C (triangle), 30°C (hexagram), 35°C (circle) and 40°C (diamond) plotted against wavelength. The change in absorption around 740, 800 and 840 nm is indicated by arrows.	146
Figure 67 Reduced scattering coefficient measured at different temperatures plotted against wavelength. A linear, least-squares fit at 40 °C (red) and 22 °C (black) show the trend (dashed lines).	147
Figure 68 Absorption coefficient at 740 and 840 nm plotted against temperature. The red circles correspond to the heating cycle data and the blue asterisks to the cooling cycle. The solid line is a least square fit to all the data, and the dashed line indicates a 68% confidence interval. The error bars give ± 1 standard deviation.	148
Figure 69 Reduced scattering coefficient at 740 and 840 nm plotted against temperature. The red circles indicate heating and blue asterisks cooling cycles. The solid lines are least square fits to heating and cooling data. The error bars and confidence interval show ± 1 standard deviation.	148
Figure 70 Absorption (a) and reduced scattering (b) coefficient variation at 800 nm plotted against temperature. The error bars and confidence intervals indicate ± 1 standard deviation.	149
Figure 71 Temperature coefficient of absorption for 1.8% solution of Intralipid plotted against wavelength. Temperature coefficient for pure water reported by Hollis, Langford et al. and the temperature coefficient for Intralipid (1%) by McGlone et al. are also included. Error bars indicate 68% confidence intervals.	151
Figure 72 Temperature coefficient for reduced scattering coefficient plotted against wavelength. The red line shows a linear fit to the temperature coefficient.	152
Figure 73 Front panel of LabView program controlling lock-in amplifier.	163
Figure 74 VI corresponding to front panel shown in Figure 73.	163

List of Figures

<i>Figure 75 Labview program controlling translation stage.</i>	164
<i>Figure 76 VI corresponding to front panel shown in Figure 75.</i>	164
<i>Figure 77 Front panel of LabView program controlling Intralipid temperature.</i>	165
<i>Figure 78 VI corresponding to front panel shown in Figure 77.</i>	165

CHAPTER 1 INTRODUCTION

The study of light transport in highly scattering media has been a focus of intense research because of its applications in diverse scientific fields ranging from biomedical to agriculture. The use of light as an analytical tool is gaining importance due to its potentially non destructive nature, even though the lower depth of penetration is a concern (Knight and Draper 2008). The observed therapeutic window (700 to 900 nm wavelength range) in the near infrared (Jobsis-vanderVliet 1999) wavelength region together with the use of optical clearing agents may provide an answer to this concern (Tuchin 2005). In biomedical applications light is used for both diagnosis and treatment. Optical microscopy is a primary example of the application of light in diagnosis.

The importance of study of light transport in turbid media, like tissue, is further emphasized by the following medical application. Pulse oximeters estimate the oxygen content in blood and are based on the principle that light absorption changes with blood oxygen content as a function of wavelength (Millikan 1942). Optical coherence tomography (Huang et al. 1991), diffuse optical tomography (Gibson et al. 2005), and photo acoustic imaging (Xu and Wang 2006) constitute some of the biomedical imaging modalities used for diagnosis. Photodynamic therapy (Wilson and Patterson 2008) is a treatment method used to kill cancer cells with the help of light sensitive drugs. Lasers find therapeutic applications in numerous other medical fields like cardiology, dentistry, dermatology, ophthalmology, etc.

In the agriculture and food industry near-infrared light is used for non-destructive testing and quality analysis (Huang et al. 2008). Diffuse near infra-red instruments are used to determine fat, moisture and protein

content in various meats (Tøgersen et al. 1999). Near infra-red spectroscopy can also be used to determine sodium chloride in cured meat (Begley et al. 1984). Near infra-red spectroscopy is used in the determination of sugar content in many fruits like peaches and mandarins (Kawano et al. 1993). The ever growing applications of light, especially lasers, in the medical field have led to theoretical models of interaction of light with tissue and introduction of the term 'photon migration'. These developments introduce a new field of study named "Biomedical Optics". Biomedical optical spectroscopy is of particular importance as it acts as a basic building block for other applications like imaging.

Depending on the instrumentation employed to determine the optical properties, photon migration spectrometers are divided into two categories: space or time resolved. In the space resolved or continuous wave method the intensity of a light source inside a turbid medium is measured at different source-detector separations to calculate the optical properties. The time resolved instrumentation can either be in the time or frequency domain. In the time domain the temporal broadening of an ultra short pulse, usually picoseconds, of light transmitted or reflected from a turbid sample is used to estimate the optical properties.

Frequency domain photon migration spectroscopy employs an intensity modulated light source to optically characterise a turbid sample. The intensity modulation frequency is usually in the radiofrequency range. After it was first suggested in the early 1990's (Fishkin et al. 1991), this is a well developed spectroscopic technique now used to characterize turbid samples like tissue non-invasively. The frequency domain spectroscopic technique uncouples absorption from scattering when determining the optical properties of turbid media which potentially allows more accurate recovery of optical coefficients. The optical properties estimated from the frequency domain spectroscopic measurements can also be used to

construct low resolution images. A brain imaging system (Imagent™) based on frequency domain measurements is available in the market for use in real clinical situations.

Wavelength tuneability offers significant advantages in spectroscopy of turbid media over discrete wavelength measurements (Hull et al. 1998). Frequency domain spectrometers using diode laser sources are inexpensive and easy to fabricate. However, they are limited to discrete wavelengths constrained by the availability of laser diodes. Frequency domain spectrometers constructed with wavelength tuneable lasers can overcome this limitation, yet there is no tuneable instrument available.

This thesis describes the fabrication of a frequency domain spectrometer with a wavelength tuneable titanium-sapphire laser whose output is modulated with an acousto-optic modulator. Theoretical aspects of the frequency domain method along with photon migration instrumentation reported to date are discussed in detail in chapters 2 and 3. A detailed description of the construction of the wavelength tuneable spectrometer is included in chapter 4.

The constructed spectrometer was used to estimate the optical properties of Intralipid®, an important tissue simulating phantom. The instrument performance was validated by making optical property measurements in different dilutions of Intralipid® in distilled water. The measured reduced scattering coefficient was compared with a separate estimate based on measurement made by a commercial particle size analyser. Our system was developed with the intension of making measurements in blood. The measured absorption coefficient varies from 0.008 to 0.045 cm⁻¹. Over the wavelength range of interest the absorption for blood falls well within this range. The acousto optic modulator efficiency falls drastically after 900 nm; measurements above this wavelength are difficult with the

present setup. The results have been published (Cletus et al. 2009) and are described in detail in chapter 5.

Chapter 5 also describes influences of glucose on the optical properties of Intralipid®. This was done by adding different concentrations of glucose solutions to Intralipid®. These measurements were motivated by the possibility of making non-invasive glucose measurements using frequency domain photon migration spectroscopy. This may find application in blood glucose monitoring as well as monitoring the sugar content in agricultural produce like fruits and also in non-invasive food quality analysis.

The optical properties of Intralipid® solution were determined at different temperatures in the range 30 to 40°C. These measurements were made as a preliminary step towards applications in in-vivo temperature monitoring in clinical situations. These results are in print (Cletus et al. 2010) and chapter 6 gives a comprehensive description of this.

Finally, chapter 7 presents our conclusions on the performance evaluation of the constructed frequency domain spectrometer and discusses the future work.

CHAPTER 2

LIGHT TRANSPORT IN TURBID MEDIA

2.1 Introduction

A simple model like the Beer-Lambert law, which is adequate to provide a complete description of light transport in an absorbing medium, fails to describe light transport in a highly scattering medium. More general models, like radiative transport theory, were used to account for multiple scattering and the directional nature of the scattering. This chapter gives a brief overview of the various models used to describe light transport in turbid media and describes the radiative transport theory and the transport of intensity modulated light in detail.

2.2 Transparent versus turbid samples

The Beer-Lambert law relates the intensity of light transmitted through a sample to its absorption by the sample. Absorption is often directly related to concentration and conventional spectrophotometers employ this relationship to estimate the concentration of a sample. This situation is illustrated in Figure 1(a) where the transmitted light intensity is given by the Beer-Lambert law:

$$I = I_0 e^{-c\epsilon L}, \tag{1}$$

where I_0 is the incident intensity, L corresponds to the pathlength the incident light travels through the sample, c is the concentration and ϵ the extinction coefficient.

The concentration and extinction coefficient are usually combined as an absorption coefficient, μ_a :

$$\mu_a = c\epsilon = \frac{1}{L} \ln\left(\frac{I_0}{I}\right). \tag{2}$$

The absorption coefficient can also be thought of as the probability of photon absorption in a medium per unit length.

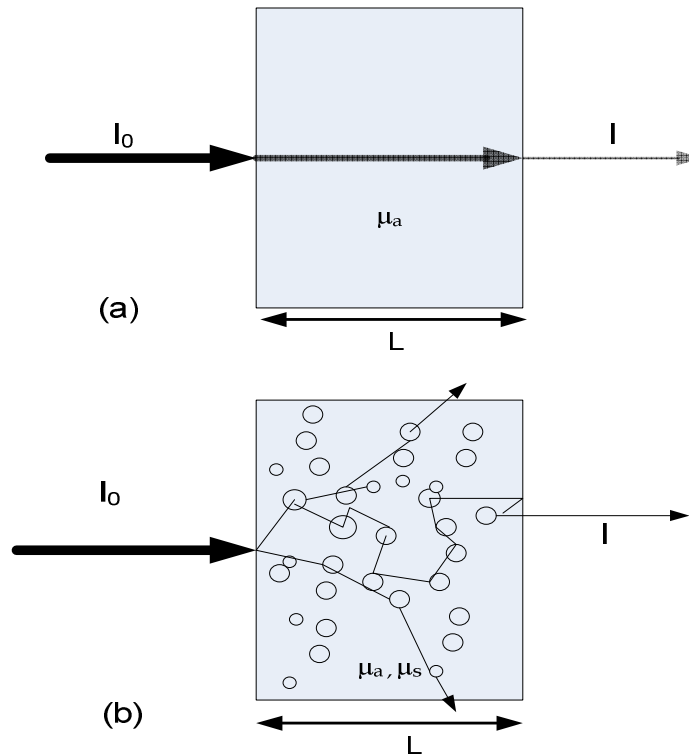


Figure 1 Optical processes in an (a) absorbing and (b) scattering media.

In a purely absorbing medium the pathlength is equivalent to the sample thickness. In the case of a scattering media, the pathlength, the incident light travels through the sample, is no longer equal to the sample thickness, L , as illustrated in Figure 1 (b), and a fraction of light is scattered out of the volume without being detected. The pathlength variation limits the application of the Beer-Lambert law to non-scattering samples. For a medium with scattering coefficient, μ_s , defined as the probability of photon scattering in a medium per unit length, equation 1 is modified to:

$$I = I_0 e^{-(\mu_a + \mu_s)L} \quad 3$$

Attempts were made to modify Beer-Lambert law to account for the scattering in applications like remote sensing, where due to cloud, fog and rain the atmosphere becomes turbid (Tam and Zardecki 1982). Early near-infrared spectroscopic techniques used the attenuation of light by absorbing constituents to characterize a turbid sample based on the Beer-Lambert law. As this failed to account for the scattering components, modifications were proposed to the Beer-Lambert law to account for the pathlength factor. Delpy et al. (1988) suggested a modified Beer-Lambert law for the attenuation(A):

$$A = -\log\left(\frac{I}{I_0}\right) = B\mu_a d + G, \quad 4$$

where B is a pathlength factor depending on absorption, scattering as well as the scattering phase function G , an unknown factor that depends on the geometry, and d is the geometrical distance between the source and detector.

Thus the average or differential pathlength, $\langle L \rangle$, was defined by introducing a differential path length factor as:

$$B = \frac{\langle L \rangle}{d}. \quad 5$$

Sassaroli and Fantini (2004) introduced a correction factor to the modified Beer-Lambert law denoted as average mean pathlength, $\overline{\langle L \rangle}$. Kocsis et al. (2006) assessed the cross talk of scattering on absorption in a cerebral cortex tissue and established that the percentage change of scattering and absorption has an equal effect on the attenuation of light. The Beer-Lambert law was found to be applicable for media with a small number of scatterers, and the application limit depends on the scattering particle parameters (Dick 1998).

2.3 Light propagation models

The modified Beer-Lambert law is an empirical description of light transport through absorbing and scattering media. This section gives an overview of the various non-empirical models that are more closely related to the physical properties of light.

2.3.1 Mie theory

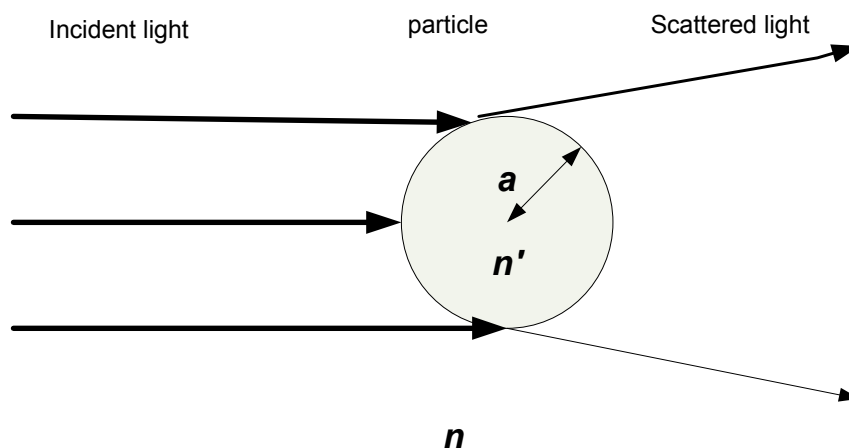


Figure 2 Light scattering by a particle with radius, a , and refractive index n' embedded in a medium with refractive index n .

In Mie scattering light is scattered by particles larger than the light wavelength, predominantly in the forward direction as illustrated in Figure 2. Mie theory (Mie 1908) describes the scattering of an electromagnetic field by spherical particles using Maxwell's equations. Mie theory is used to calculate the solution of Maxwell's equations inside and outside the sphere with undetermined coefficients and determines these coefficients by applying boundary conditions on the spherical surface. For a spherical particle the Mie theory can be used to calculate the scattering efficiency, the anisotropy and scattering cross section. The scattering cross section in the case of a single scatterer is its scattering capability. This cross section is like an effective area of the scattering particle and can be larger or smaller than the geometric cross section. The scattering efficiency is usually defined as the scattering cross section

divided by the geometric cross section of the scatterer. The scattering anisotropy, g , is defined as the average scattering angle distribution weighted over the probability of each scattering angle. The scattering coefficient and reduced scattering coefficient can be computed from the above results. Mie theory gives useful results even for non-spherical particles by approximating them to equivalent spheres. Chalut et al. (2008) demonstrated that even for spheroids with extreme aspect ratio Mie theory based models can be used to estimate the size of spheroid scatterers quite accurately.

Mie theory calculations are usually done for purely scattering media with no absorption. The theory has been extended to spherical particles embedded in an absorbing medium (Fu and Sun 2001; Sudiarta and Chylek 2001). This indicates that Mie theory can be applied to tissues with high albedos ($\mu_a \ll \mu'_s$). Mie theory can also be used to estimate the optical properties of turbid media even though it treats single scattering only. Mie theory assumes no shadowing, which is generally correct if the spacing between particles is 3 to 5 particle diameters (van de Hulst 1981). In the case of highly scattering media this condition is not always satisfied and leads to erroneous results.

2.3.2 Kubelka-Munk theory

The two flux theory by Kubelka and Munk (1931; Kubelka 1948) characterises a medium by its effective absorption and scattering coefficients, K and S ; where K is the attenuation of the diffuse fluxes resulting from absorption, while the coefficient, S , describes the net scattering of flux between the forward and the backward directions. This theory assumes that a light beam travelling in the transmitted direction decreases in intensity due to absorption and scattering and gains intensity from a scattering process of a beam coming from the other direction. Thus it relates the optical properties of a medium to the measurable

transmission and reflection of light. The applicability of Kubelka-Munk theory is limited to simple slab geometries and to weakly or non absorbing media (Vargas and Niklasson 1997). The theory has been revised with statistical analysis and applied to light propagation in various turbid media (Yang and Kruse 2004; Yang and Miklavcic 2005). The Kubelka-Munk theory is not widely used in the analysis of highly scattering media, especially in tissue optics, compared to the other models discussed here. The reason for this is the poor accuracy of results obtained by this theory (Mudgett and Richards 1971).

2.3.3 Monte Carlo simulations

Monte Carlo simulation is another statistical method used to solve light propagation in highly scattering media (Prahl et al. 1989; Wang et al. 1995). A brief tutorial about this method can be found in Jacques (2008). The Monte Carlo model describes light propagation as a random walk between points of absorbers and scatterers. The probability of absorption and scattering events happening depends on the optical properties of the medium: μ_a and μ_s . In the simulation the photon packet is monitored until it escapes the medium or its statistical weight is below a certain threshold. By this procedure the fluence rate distribution, diffuse reflectance and transmittance can be recorded (Splinter and Hooper 2007).

The Monte Carlo method is considered to be the “gold standard” for solving light transport problems in turbid media. This method does not suffer from any inaccuracy compared to the diffusion equation and nearly any geometry can be simulated. It has the drawback of being computationally very time consuming (Rogers 2006; Binzoni et al. 2008).

Kienle and Patterson (1996) showed that absorption and reduced scattering coefficients can be determined with errors smaller than 1% and 2% using a single Monte Carlo simulation from time resolved reflectance

data from a semi-infinite and infinite turbid medium. They also demonstrated that knowledge of the refractive index improves the accuracy of the optical properties derived. They concluded that the Monte Carlo method can also be applied to the frequency domain by numerical Fourier transformation of the time resolved reflectance data.

Graff et al. (1993) demonstrated that Monte Carlo results can be used again with the same phase function and albedos in situations where total attenuation is different from the simulated attenuation if geometric dimensions are scaled. Palmer and Ramanujam (2006) reported a fast Monte Carlo based method to extract the optical properties of turbid media. They showed that this method is valid for media with a wide range of optical properties provided a single phantom calibration measurement is made. The method was insensitive to the wavelength used to extract the optical properties in the ultra-violet and visible region, but in the near-infrared it resulted in an increase in the mean rms error. This model was applied to breast cancer diagnosis (Palmer et al. 2006). The extracted optical properties showed statistically significant differences between normal and malignant breast tissues. However, the requirement of *a priori* knowledge of absorbers and scatterers present in the tissue was considered a limitation of the model.

Other developments include the adaptation of multicanonical Monte Carlo (Berg 1998) to the classical Monte Carlo method to improve the efficiency (Bilenca et al. 2005). With the adaptation of the multicanonical Monte Carlo method, which was originally proposed for first order phase transitions (Berg and Neuhaus 1992), Bilenca et al. obtained a six to seven fold improvement in computational time compared to classical methods even at very low probability density functions. The results of their simulations were in very good agreement with diffusion theory and the classical Monte Carlo method.

Xu et al. (2006) calculated optical properties (absorption and reduced scattering coefficients) from frequency domain measurements based on four models. They showed that Monte Carlo was the best model, which recovered the optical properties within 10% error irrespective of the scattering albedos investigated. Their results indicated that the diffusion theory model was able to recover the optical properties within 10% error, provided the reduced scattering is 10 times higher than the absorption.

2.3.4 Finite element method

The finite element method is another numerical method used to solve the radiative transport (detailed discussion in section 2.4) equation (Arridge and Schweiger 1995; Arridge et al. 1993; Schweiger et al. 1995). The finite element method solves partial differential equations in complex geometries; more details about the mathematical formulations can be found in Lapidus and Pinder (1999). Arridge et al. used the finite element method to solve the diffusion approximation (discussed in section 2.4.1) to the radiative transport equation and derived the photon density inside an object. They have also derived the photon flux using boundary conditions and made a comparison between Monte Carlo and finite element calculations. The results showed that the finite element method is twenty times faster than the Monte Carlo method for time domain measurements and 550 times faster in the case of continuous intensity measurements.

The finite element solution of the diffusion equation was later extended to the frequency domain case (Schweiger and Arridge 1997) in irregular geometries and inhomogeneous distributions of absorption and scattering parameters. Schweiger and Arridge found that the numerical stability of the model depends on the mesh resolution, error limit of the conjugate gradient method, optical properties of the simulated media and the modulation frequency. The conjugate gradient method refers to an iterative scheme for symmetric and positive definite problems. Good

agreement in results obtained with the Monte Carlo and finite element method for a cylindrical phantom embedded with some absorbers has been demonstrated by Sassaroli et al. (1999).

There is also the random walk theory which introduced the term “photon migration” (Bonner et al. 1987; Gandhjbakhche et al. 1995). In random walk theory the tissue continuum is replaced by a cubic lattice with a step size inversely proportional to the scattering coefficient, and photons can move isotropically between adjacent lattice points (Gandhjbakhche et al. 1995). Random walk theory has been successfully applied to derive the optical properties of abnormalities within the tissue (2000; Chernomordik et al. 2002).

2.4 Radiative transport equation

The deterministic methods use the radiative transport equation (Ishimaru 1978b; Welch and vanGemert 1995). In this method the light transport in turbid media is analysed with the solution to the radiative transport equation (which is considered equivalent to the numerical Monte Carlo method) by the diffusion approximation. The strength of diffusion theory to analyse light transport in turbid media has been reported by many groups (Karagiannes et al. 1989; Kaltenbach and Kaschke 1993; Shen et al. 2007). A comprehensive overview of diffuse light transport is also reported by Jacques and Pogue (2008). In diffusion theory the photons injected into turbid media lose their directional nature after multiple scattering events. Thus it becomes similar to optical energy diffusing down a concentration gradient and laws of diffusion become applicable. A more detailed discussion of the diffusion approximation to the radiative transport theory is provided in this section along with the special case of modulated diffusion.

Radiative transfer theory was first used in astrophysics (Chandrasekhar 1960) to study light propagation from distant galaxies through galactic dust and planetary debris and also in nuclear physics to study the neutron transport in nuclear reactors. A good review of the historical development of the application of radiative transfer theory to various disciplines can be found in Shore (2002). Later the radiative transport theory became an integral part in the analysis of light transport in highly scattering media, like tissue. As the equation was difficult to solve, approximate solutions were developed with the help of assumptions. Here we first write down the radiative transport equation and show with the help of some approximations how it is transformed to the standard diffusion equation. Later on in this section we describe how optical properties of the medium can be estimated from the solutions of the standard diffusion equation based on some experimentally measurable quantities.

The two basic assumption of radiative transport theory are:

1. that the migrating particles (in our case the photons) do not interact with each other, and
2. that conservation of energy applies.

Consider a source that injects photons into a macroscopically homogeneous medium consisting of absorbers and scatterers. The radiative transport equation can be derived by considering a stationary differential cylindrical volume of length, ds , along the photon propagation direction, \hat{s} , as shown in Figure 3 (Wang and Wu 2007; Ishimaru 1978b). The radiative transport equation (RTE) gives the change in energy in the volume element within the solid angle per unit time:

$$\frac{\partial L(\vec{r}, \hat{s}, t)}{v \partial t} = -\hat{s} \cdot \nabla L(\vec{r}, \hat{s}, t) - \mu_t L(\vec{r}, \hat{s}, t) + \mu_s \int_{4\pi} L(\vec{r}, \hat{s}', t) P(\hat{s}', \hat{s}) d\Omega' + S(\vec{r}, \hat{s}, t), \quad 6$$

where \vec{r} denotes the position, \hat{s} is the unit vector along the photon propagation, \hat{s}' the unit vector along the scattering direction, $d\Omega$ and $d\Omega'$ are the corresponding solid angles, and t denotes the time. The speed of photons in the medium is v . L is the radiance and is the energy flow per normal area and solid angle and has the unit ($\text{W m}^{-2} \text{sr}^{-1}$). μ_t is the total extinction coefficient equal to the sum of the absorption and scattering coefficient. In derivation of equation 6 effects such as polarization and nonlinearity are ignored, and only elastic scattering is considered.

For a time-invariant light source the term on the left hand side of Equation 6 is zero. The first term on the right hand side is the loss due to photons diverging out of the volume element. The second term corresponds to the extinction due to both absorption and scattering. The third term is the contribution from photons scattered into the solid angle $d\Omega$ from $d\Omega'$. The last term corresponds to the source strength. The third term contains the phase function, $P(\hat{s}', \hat{s})$, such that the product $P(\hat{s}', \hat{s}) d\Omega$ is the probability of light with propagation direction \hat{s}' being scattered into $d\Omega$ with

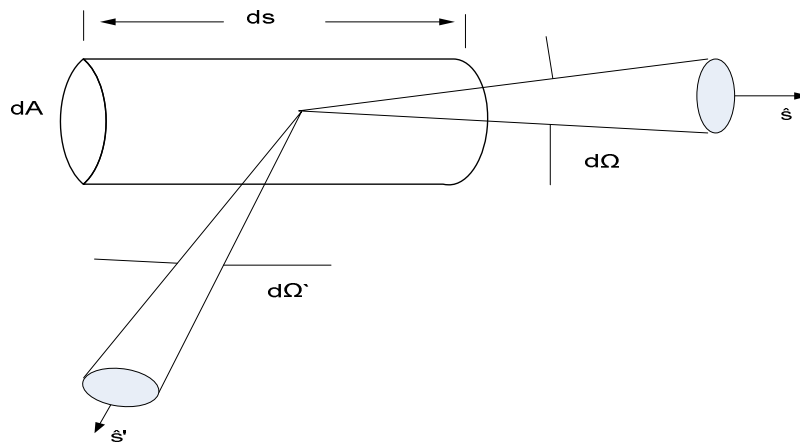


Figure 3 Cylindrical differential volume element of the medium along photon propagation direction.

direction \hat{s} .

The phase function depends only on the angle between scattered and incident directions so that:

$$P(\hat{s}', \hat{s}) = P(\hat{s}' \cdot \hat{s}), \quad 7$$

where $(\hat{s}' \cdot \hat{s})$ is equal to the cosine of the angle between \hat{s}' and \hat{s} . Thus to account for the directionality of the scattering event the anisotropy parameter, g , is introduced (Jacques et al. 1987) and defined as:

$$g = \int_{4\pi} (\hat{s}' \cdot \hat{s}) P(\hat{s}' \cdot \hat{s}) d\Omega = \langle \cos(\theta) \rangle \quad 8$$

Anisotropy, g , then is the average cosine of the angle between the scattering and incident directions.

A more common way to express the radiative transport equation is in terms of *angular photon density*. Which is easy enough to follow and as we are going to deal with photon density in the coming chapters, it is used instead of radiance and fluence. We would like to provide the equations that relate radiance and fluence rate to photon density. We found different notations in use to denote the photon propagation in literature: radiance, fluence rate (intensity), current density and photon density. The following equations show the relationship between them.

Fluence rate, Φ , is the energy flow per unit area and unit time and is related to radiance, L , by:

$$\Phi = \int_{4\pi} L d\Omega \quad 9$$

Current density, J , is the net energy flow per unit area and unit time and is the vector equivalent of fluence rate. Photon density, U , is the number of photons propagating per unit volume. Photon density can be written as

$$U = \frac{\Phi}{ch\nu}, \quad 10$$

where $h\nu$ is the energy of a single photon, and c is the speed of light.

2.4.1 Diffusion approximation

To solve the radiative transport equation a number of simplifying assumptions are needed.

The two assumptions made (along with those described in section 2.4) to obtain the diffusion approximation are:

1. The spherical harmonic expansion of radiance is limited to the first order. This condition is mathematically written as:

$$L(\vec{r}, \hat{s}, t) = \frac{1}{4\pi} \Phi(\vec{r}, t) + \frac{3}{4\pi} \vec{J}(\vec{r}, t) \cdot \hat{s} \quad 11$$

We assume the scattering to be isotropic. This is referred to as the P₁-approximation. The P₁-approximation provides accurate results as long as the measurements are made in regions far from boundaries and sources (Jacques and Pogue 2008).

2. The fractional change in current density in one transport mean free path is much less than unity

$$\left(\frac{1}{v(\mu_a + \mu'_s)} \right) \left(\frac{1}{|\vec{J}(\vec{r}, t)|} \left| \frac{\partial \vec{J}(\vec{r}, t)}{\partial t} \right| \right) \ll 1, \quad 12$$

where μ_s' is the reduced (transport) scattering coefficient and is given by

$$\mu_s' = \mu_s(1 - g) \quad 13$$

$$l_t' = \frac{1}{\mu_a + \mu_s'} \quad 14$$

is the transport mean free path.

These approximations lead to Fick's law:

$$\vec{J}(\vec{r}, t) = -D\nabla\Phi(\vec{r}, t) \quad 15$$

which describes the diffusion of photons in a scattering medium. The diffusion coefficient, D , is given by:

$$D = \frac{1}{3(\mu_a + \mu_s')} \quad 16$$

The photon diffusion coefficient is discussed in section 2.6.

Using the approximations provided by equations 11 and 12 equation 16 reduces to the diffusion equation:

$$\frac{\partial\Phi(\vec{r}, t)}{\partial t} + \mu_a\Phi(\vec{r}, t) - D\nabla^2\Phi(\vec{r}, t) = S(\vec{r}, t) \quad 17$$

Rewriting equation 17 in terms of photon density U on the basis of equation 10 gives:

$$\frac{\partial U(\vec{r}, t)}{\partial t} + \nu\mu_a U(\vec{r}, t) - \nu D\nabla^2 U(\vec{r}, t) = S(\vec{r}, t) \quad 18$$

Even though photon density and flux are proportional (Liu et al. 1993), the photon density analysis is shown to yield slightly better results regarding experimentally measurable quantities (Ducros et al. 2008). Inversion procedures to calculate the optical properties of turbid media can be developed from solutions of equation 18.

2.4.2 Diffusion coefficient

There is an argument in the literature whether equation 16 is correct. Furutsu and Yamada (1994) suggested a diffusion coefficient independent of absorption. Durduran et al. (1997) using the Monte Carlo method also suggested that the diffusion coefficient is independent of absorption. The authors concluded that the discrepancy between Monte Carlo results and diffusion theory is less than 5% for an absorption independent diffusion coefficient and is as high as 20% in the case of an absorption dependant diffusion coefficient. Bassani et al. (1997) also provided numerical and experimental evidence that the diffusion coefficient is independent of absorption. The numerical simulations were carried out by solving the radiative transport equation by Monte Carlo code. The experimental evidence was provided by making measurements on polystyrene spheres suspended in water and Intralipid 10% at various added absorber concentrations.

In contrast Rinzema et al. (1998) rejected the idea of absorption independence of the diffusion coefficient with results of measurements on latex particles suspended in water with added absorbers. Aronson and Corngold (1999) criticised Durduran et. al.'s idea by concluding that there is no medium in which the diffusion coefficient is independent of absorption. Aronson and Corngold provided an explanation for the results obtained in Bassani et. al.'s experiments in polystyrene sphere suspension. The mean spacing between the spheres was found to be 4 μm , and it was large compared to the wavelength used (634 nm). These conditions were

sufficient to apply the radiative transport theory. A similar inter particle spacing estimate was unavailable for Intralipid in the experiments of Bassani et al. Further Graff and Bosch (2000) supported the idea of absorption dependence of the diffusion coefficient.

Cai et al. (2002) suggested that the diffusion coefficient is independent of absorption but is time dependant and showed that the diffusion coefficient cannot be evaluated by scattering alone.

In the tissue therapeutic window absorption is two orders of magnitude smaller than scattering. Consequently the inclusion or exclusion of absorption in the expression for diffusion coefficient makes no change to our results. However, in media with higher absorption the diffusion coefficient needs to take absorption into account to get robust results for optical properties.

2.4.3 Frequency-domain solution to diffusion equation

The use of intensity modulated light to estimate the optical properties of turbid media by means of the diffusion equation was first suggested by Fishkin et al. (1991). The diffusion equation was solved for a homogeneous infinite medium (Fishkin and Gratton 1993) by assuming a sinusoidally intensity modulated point source of the form

$$S(\vec{r}, t) = \delta(r)S[1 + Me^{-i(\omega t + \theta)}], \quad 19$$

where $\delta(r)$ is the Dirac-delta function, M the modulation depth, ω is the angular frequency of modulation, θ is some arbitrary phase and S is the unmodulated source amplitude. Fiskin and Gratton obtained the photon density at a distance, r , from the source at time, t , as:

$$U(\vec{r}, t) = \frac{S}{4\pi\nu Dr} e^{-r\left(\frac{\mu_a}{D}\right)^{\frac{1}{2}}} + \frac{SM}{4\pi\nu Dr} e^{\left\{-r\left(\frac{\nu^2\mu_a^2 + \omega^2}{\nu^2 D^2}\right)^{\frac{1}{4}} \cos\left[\frac{1}{2} \tan^{-1}\left(\frac{\omega}{\nu\mu_a}\right)\right]\right\}} e^{\left\{ir\left(\frac{\nu^2\mu_a^2 + \omega^2}{\nu^2 D^2}\right)^{\frac{1}{4}} \sin\left[\frac{1}{2} \tan^{-1}\left(\frac{\omega}{\nu\mu_a}\right)\right] - i(\alpha t + \theta)\right\}} \quad 20$$

The solution of the diffusion equation with a source described by equation 19 was found to be a scalar highly damped spherical wave as illustrated in Figure 4 and was called a photon density wave (PDW). For a non absorbing medium the photon density wave is characterized by a phase velocity (V_{PDW}) and wavelength (λ_{PDW}) which is dependent on the modulation frequency and optical properties of the medium. The photon density wave is independent of the electromagnetic wave features.

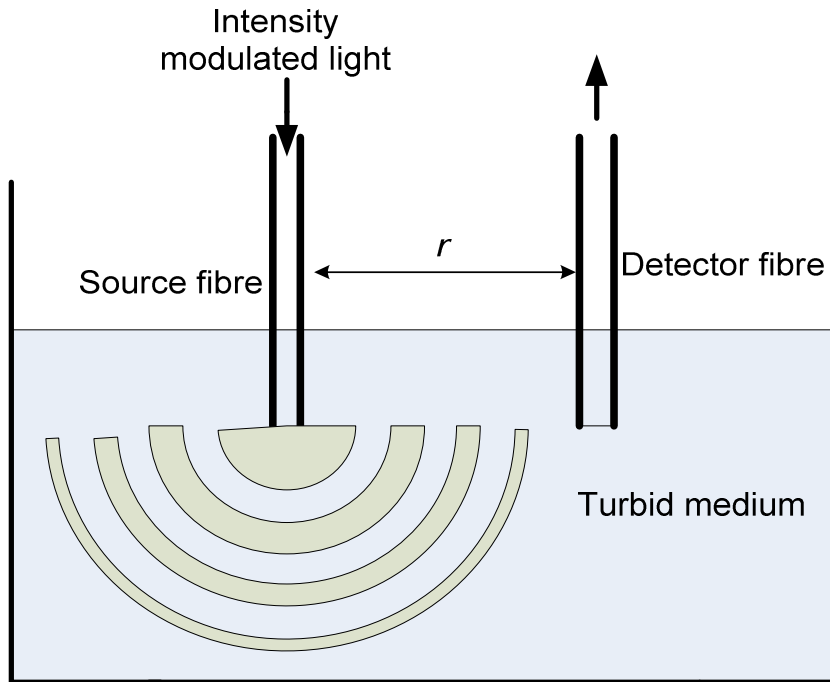


Figure 4 Photon density wave generated (concentric semi-circles) inside a turbid medium by intensity modulated light.

Diffuse photon density waves demonstrate wave like characteristics such as interference (Schmitt et al. 1992), diffraction (Fishkin and Gratton 1993), refraction (O'Leary et al. 1992) and scattering (Boas et al. 1994). The above

solution was derived for an infinite medium. Solutions have also been reported in semi-infinite (Fantini et al. 1994b; Fishkin and Gratton 1993), infinite slab, cylindrical and spherical geometries (Arridge et al. 1992).

The wavelength and phase velocity of the photon density wave for a non absorbing medium are given by the following equations (Fishkin and Gratton 1993):

$$\lambda_{PDW} = 2\pi \left(\frac{2\nu D}{\omega} \right)^{\frac{1}{2}}, \quad 21$$

$$V_{PDW} = (2\nu D \omega)^{\frac{1}{2}}. \quad 22$$

Figure 5 illustrates the wavelength of the photon density wave at various modulation frequencies for media with different reduced scattering coefficients. The wavelength at fixed modulation frequency is smaller for a

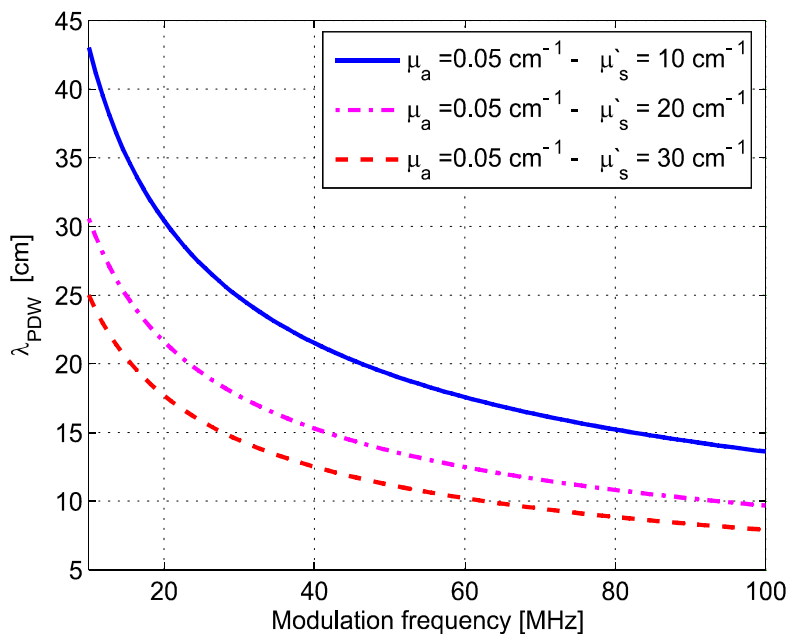


Figure 5 Wavelength of photon density waves plotted against modulation frequency for a medium with three different reduced scattering coefficients.

medium with higher scattering coefficient. The time evolution of intensity modulated light in a multiple scattering medium is illustrated in Figure 6. A detector placed at a short distance from the source will measure a light signal with a modulation frequency that is the same as that of the source. Due to absorption and scattering of the medium, the detected signal will be reduced in amplitude and shifted in phase.

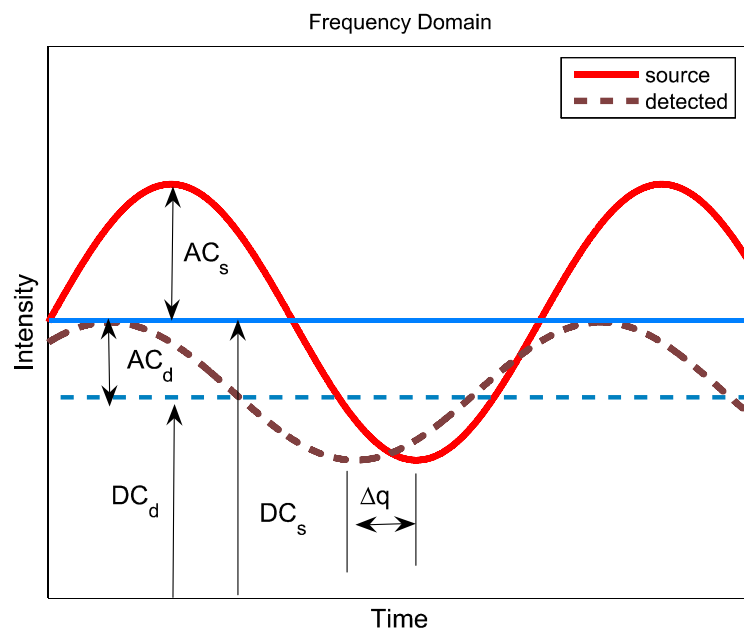


Figure 6 Time evolution of intensity modulated light illustrates the measurable quantities in the frequency domain.

Any two of the following quantities measured in the frequency domain are sufficient to extract the optical properties of the medium (Fantini et al. 1995).

- The phase delay (Φ) of the detected signal relative to source.
- The time invariant average intensity, termed as the *DC* component (*DC*).
- The amplitude of photon density oscillations, termed as the *AC* component (*AC*).

The following equations give these measurable quantities in an infinite medium (Sun et al. 2002):

$$\Phi = r \left(\frac{v^2 \mu_a^2 + \omega^2}{v^2 D^2} \right)^{\frac{1}{4}} \sin \left[\frac{1}{2} \tan^{-1} \left(\frac{\omega}{v \mu_a} \right) \right], \quad 23$$

$$\ln[rDC] = -r \left(\frac{\mu_a}{D} \right)^{\frac{1}{2}} + \ln \left(\frac{S}{4\pi v D} \right), \quad 24$$

$$\ln[rAC] = -r \left(\frac{v^2 \mu_a^2 + \omega^2}{v^2 D^2} \right)^{\frac{1}{4}} \cos \left[\frac{1}{2} \tan^{-1} \left(\frac{\omega}{v \mu_a} \right) \right] + \ln \left(\frac{SM}{4\pi v D} \right). \quad 25$$

To estimate the optical properties from equations 23 to 25 we need to eliminate error arising out of unknown source contributions. Consider the photon density wave measured at two different positions r and r_0 . Then equation 23 to 25 can be rewritten as (Sun et al. 2002):

$$DC_{rel} = \frac{DC(r)}{DC(r_0)} = \frac{r_0}{r} e^{\left[-(r-r_0) \left(\frac{\mu_a}{D} \right)^{\frac{1}{2}} \right]}, \quad 26$$

$$AC_{rel} = \frac{AC(r)}{AC(r_0)} = \frac{r_0}{r} e^{\left\{ -(r-r_0) \left(\frac{v^2 \mu_a^2 + \omega^2}{v^2 D^2} \right)^{\frac{1}{4}} \cos \left[\frac{1}{2} \tan^{-1} \left(\frac{\omega}{v \mu_a} \right) \right] \right\}} \quad 27$$

$$\Phi_{rel} = \Phi(r) - \Phi(r_0) = (r - r_0) \left(\frac{v^2 \mu_a^2 + \omega^2}{v^2 D^2} \right)^{\frac{1}{4}} \sin \left[\frac{1}{2} \tan^{-1} \left(\frac{\omega}{v \mu_a} \right) \right]. \quad 28$$

The relative modulation or modulation depth can be written as

$$M_{rel} \equiv \frac{AC_{rel}}{DC_{rel}}. \quad 29$$

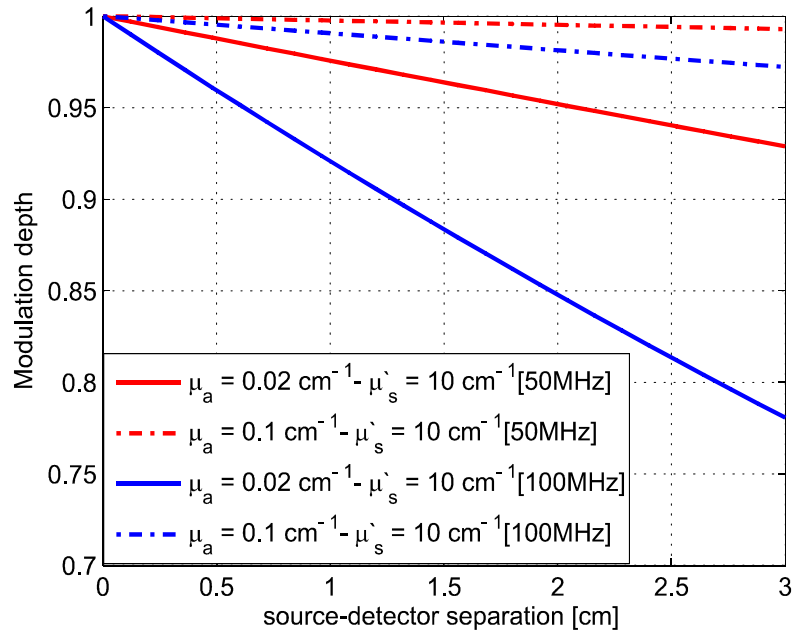


Figure 7 Variation of modulation depth against source-detector separation for modulation frequencies of 50 and 100 MHz. The plot illustrates the effect of absorption of the medium on modulation. The dashed line correspond to a medium with absorption coefficient 0.1 cm^{-1} and the solid line to a medium with absorption 0.02 cm^{-1} , both having the same reduced scattering coefficient.

Figure 7 and Figure 8 illustrate the simulated modulation and normalised phase variation of photon density waves up to a source detector separation of 3 cm based on equations described above, at a modulation frequency of 50 MHz, absorption coefficient of 0.02 and 0.1 cm^{-1} and reduced scattering coefficient of 10 cm^{-1} (typical of tissue in the therapeutic window). These figures show that the absorption of the medium increases the relative change in phase and modulation becomes less significant for small source detector separation at lower modulation frequencies. Thus at lower modulation frequency and at moderately high absorption coefficients, more sensitive instrumentation is needed to measure the change in phase and amplitude. This condition can also be understood from Figure 5. For example at 50 MHz modulation the wavelength of the photon density wave is of the order of 15 to 20 cm. The instrument must be sensitive enough to observe the change in phase and amplitude in a

detector scan of the order of 2 cm. Thus the sensitivity of frequency domain instruments depends on the modulation frequency (Fantini et al. 1995).

Equations 26 to 29 can be rewritten as follows:

$$\ln\left(\frac{r}{r_0} DC_{rel}\right) = -(r - r_0) \left[3\mu_a (\mu_a + \mu_s') \right]^{\frac{1}{2}}, \quad 30$$

$$\ln\left(\frac{r}{r_0} AC_{rel}\right) = -(r - r_0) \left(\frac{3\mu_a (\mu_a + \mu_s')}{2} \right)^{\frac{1}{2}} \left[\sqrt{1 + \left(\frac{\omega}{v\mu_a} \right)^2} + 1 \right]^{\frac{1}{2}}, \quad 31$$

$$\Phi_{rel} = (r - r_0) \left(\frac{3\mu_a (\mu_a + \mu_s')}{2} \right)^{\frac{1}{2}} \left[\sqrt{1 + \left(\frac{\omega}{v\mu_a} \right)^2} - 1 \right]^{\frac{1}{2}}, \quad 32$$

and

$$\ln(M_{rel}) = -(r - r_0) \sqrt{\frac{3\mu_a (\mu_a + \mu_s')}{2}} \left[\sqrt{2} - \left(\sqrt{1 + \left(\frac{\omega}{v\mu_a} \right)^2} + 1 \right)^{\frac{1}{2}} \right]. \quad 33$$

Equations 30 to 33 are used to calculate the absorption and reduced scattering coefficients. It is evident that all the quantities mentioned are relative measurements. Thus in the frequency domain we can calculate absolute optical properties from relative measurements eliminating many sources of bias. Since we have two unknowns and three equations, measuring any two of the frequency domain parameters will lead to the estimation of μ_a and μ_s' . There are two approaches in the frequency domain by which we can estimate absorption and reduced scattering coefficients. These are called the multi-frequency and multi-distance approaches.

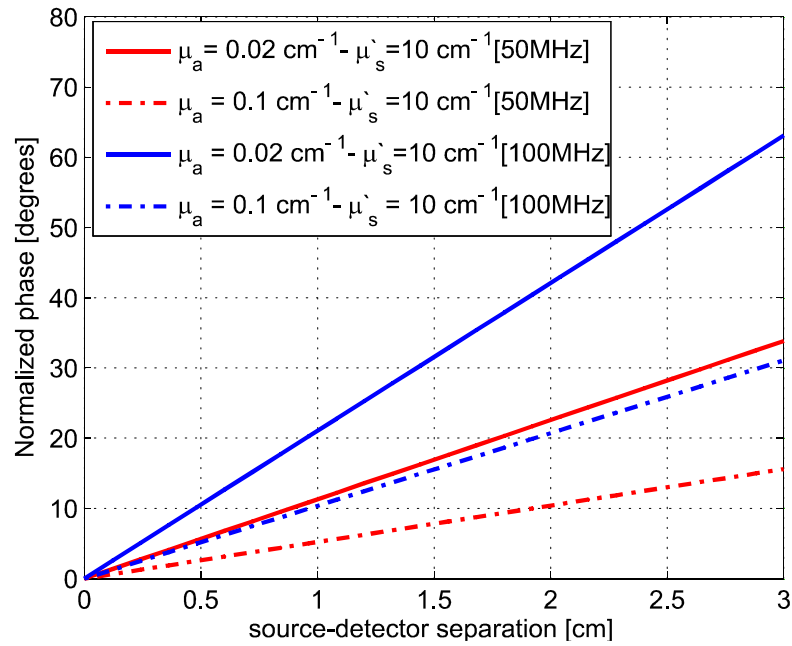


Figure 8 Phase variation plotted against source detector separation. The dotted and solid lines correspond to medium with different absorption coefficient and same reduced scattering coefficient.

2.4.4 Multi frequency measurements

The multi frequency method measures the AC_{rel} , DC_{rel} and Φ_{rel} as functions of modulation frequency. At fixed source detector separations ($r-r_0$) the AC amplitude, DC amplitude and phase are nonlinear functions of modulation frequency. In this method the amplitude attenuation and phase shift are measured at fixed source-detector separation as modulation frequency is varied. A nonlinear regression of the phase shift and modulation is used to calculate the absorption and reduced scattering coefficients (Pham et al. 2000; Sun et al. 2002).

For this method we first need to eliminate the instrument response, i.e. the phase and amplitude changes by the instrument alone. For this, a measurement needs to be made in a medium with optical properties known *a priori*. This assumes that the instrument response function is the same for the calibration medium and medium under investigation. A detailed description of the non linear fitting procedure in multi frequency measurements can be found in Huang (2004). Fitting any of the measured

quantities, like amplitude, attenuation or phase lag, is enough to extract the optical properties. However, the simultaneous use of phase and amplitude data improves the robustness and fidelity of the fit (Pham et al. 2000). In the multi-frequency method, the most accurate and precise estimation of reduced scattering coefficient is provided by fitting the phase data in combination with AC or DC amplitude attenuation (Huang 2004). The reduced scattering coefficients were calculated with a precision of 0.24% and accuracy of 2.7% using multi-frequency measurements.

2.4.5 Multi distance measurements

In contrast to the multi-frequency method, the multi-distance approach uses relative measurements, thereby eliminating the need to know the instrument response. The multi-distance method measures any two of the AC_{rel} , DC_{rel} and Φ_{rel} as functions of source-detector separations at a fixed modulation frequency. Equations 30 to 33 demonstrate that at constant modulation frequency, $\ln[(r/r_0)DC_{rel}]$, $\ln[(r/r_0)AC_{rel}]$ and Φ_{rel} are linearly related to $(r-r_0)$. Then the slopes of a linear regression of $\ln[(r/r_0)DC_{rel}]$, $\ln[(r/r_0)AC_{rel}]$ and Φ_{rel} against $(r-r_0)$ can be written as follows

$$m_{DC} = -(3\mu_a(\mu_a + \mu_s'))^{\frac{1}{2}}, \quad 34$$

$$m_{AC} = -\sqrt{\frac{3}{2}\mu_a(\mu_a + \mu_s')} \left[\sqrt{1 + \left(\frac{\omega}{v\mu_a}\right)^2} + 1 \right]^{\frac{1}{2}}, \quad 35$$

$$m_{\Phi} = \sqrt{\frac{3}{2}\mu_a(\mu_a + \mu_s')} \left[\sqrt{1 + \left(\frac{\omega}{v\mu_a}\right)^2} - 1 \right]^{\frac{1}{2}}. \quad 36$$

Optical properties can be calculated from any of the following combinations (1) $m_{DC} + m_{AC}$, (2) $m_{DC} + m_{\Phi}$, (3) $m_{AC} + m_{\Phi}$ using (Fantini et al. 1994a; Sun et al. 2002):

$m_{DC} + m_{AC}$:

$$\mu_a = \frac{\omega}{\nu} \left\{ \left[2 \left(\frac{m_{AC}}{m_{DC}} \right)^2 - 1 \right]^2 - 1 \right\}^{\frac{1}{2}}, \quad 37$$

$$\mu'_s = \frac{m_{DC}^2}{3\mu_a} - \mu_a. \quad 38$$

$m_{DC} + m_{\Phi}$:

$$\mu_a = \frac{\omega}{\nu} \left\{ \left[2 \left(\frac{m_{\Phi}}{m_{DC}} \right)^2 + 1 \right]^2 - 1 \right\}^{\frac{1}{2}}, \quad 39$$

$$\mu'_s = \frac{m_{DC}^2}{3\mu_a} - \mu_a. \quad 40$$

$m_{AC} + m_{\Phi}$:

$$\mu_a = \frac{\omega}{2\nu} \left[\frac{m_{\Phi}}{m_{AC}} - \frac{m_{AC}}{m_{\Phi}} \right], \quad 41$$

$$\mu'_s = \frac{m_{AC}^2 - m_{\Phi}^2}{3\mu_a} - \mu_a. \quad 42$$

The important features of the multi-distance approach have been demonstrated by Fantini et al. (1995). Gerken and Faris (1999) performed optical property measurements in a mixture of acrylic hollow spheres in water using the multi distance approach. They calculated the absorption and reduced scattering coefficients using all three measurement combinations mentioned above. Gerken and Faris obtained less accurate results for the *DC* and *AC* slope combination at higher absorption values compared to the other measurement methods. The multi distance method

using *AC* or *DC* and phase slopes provides the most accurate and robust optical property measurements in the modulation frequency range 50 to 100 MHz (Huang 2004).

2.4.6 Accuracy of results obtained from diffusion approximation

Diffusion theory is least accurate near the source where the two approximations—*isotropic source* and *scatter's dominance of absorption*—are not valid. However in the far field, the diffusion approximation describes the light propagation quite well. Moreover, despite these limitations, the model has been applied to estimate optical properties successfully both theoretically and experimentally. Martelli et al. (2000) investigated the accuracy of results obtained from diffusion theory for an isotropic point source in a weakly absorbing homogeneous medium, by comparing with Monte Carlo results. For weakly absorbing media the discrepancy between optical properties obtained from the diffusion approximation and Monte Carlo were within 1% or 10% for weakly ($\mu_a=0.01 \text{ cm}^{-1}$) and strongly ($\mu_a=0.1 \text{ cm}^{-1}$) absorbing media, respectively. The boundary conditions were not considered in this comparison, and they expected the errors to increase if the boundary conditions were considered.

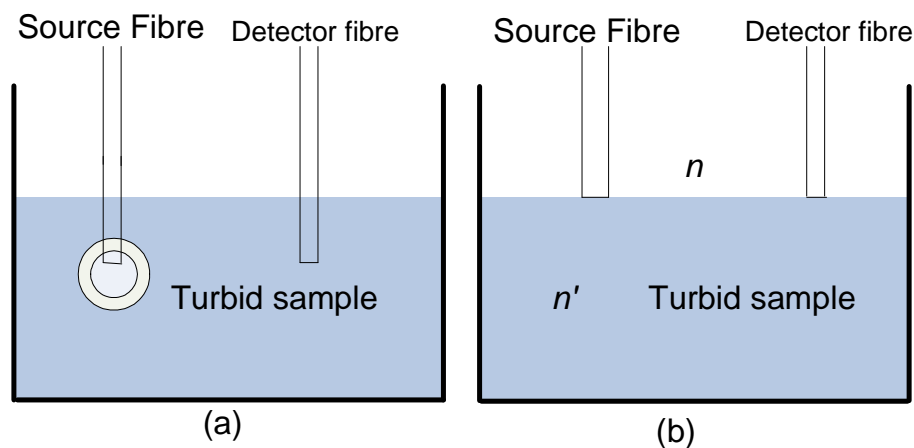


Figure 9 Infinite (a) and semi infinite (b) medium geometries in photon migration measurements.

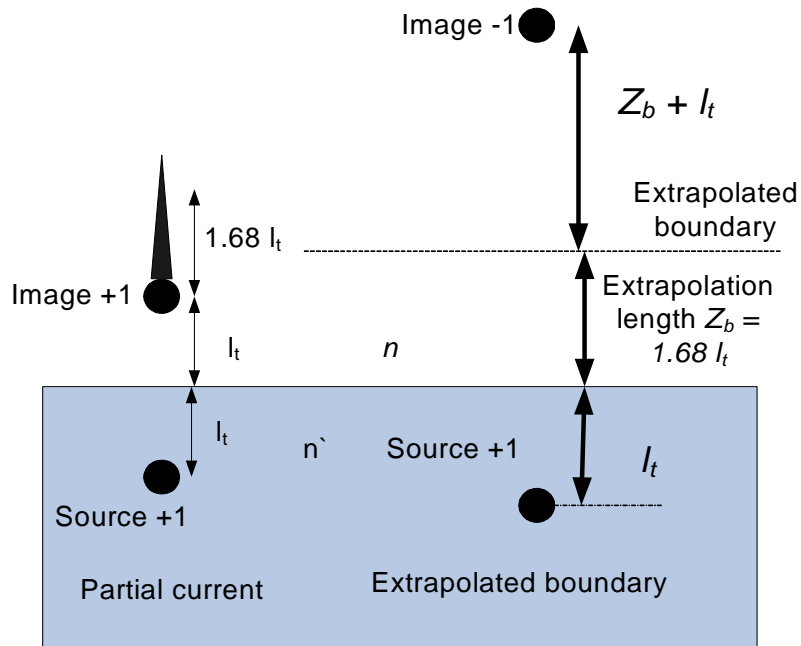


Figure 10 Source and image geometry for partial current and extrapolated boundary approach taken from Haskell et al. (1994).

A boundary is the encounter of a change in refractive index. This could be walls of the container in an experiment situation or air-tissue boundary for in-vivo measurements. This problem was dealt with boundary conditions for the diffusion of light (Haskell et al. 1994; Aronson 1995). The diffusion theory for an infinite isotropic homogeneous medium is illustrated in Figure 9 (a). In real clinical or many other measurement situations the concept of an infinite medium with a uniform refractive index is going to break down. For example when the frequency domain technique is used to non-invasively monitor optical properties of a tissue sample, an air-tissue boundary needs to be considered as indicated in Figure 9 (b).

Haskell et al. (1994) demonstrated errors of more than 50% if boundary conditions were neglected in non-invasive measurements. Haskell et al. concluded that the non-invasive measurement of thick tissues needed rigorous analysis of boundary conditions and suggested a unified-partial current-extrapolated boundary approach as illustrated in Figure 10. In the partial current and extrapolated boundary approaches, the fluence rate is

analysed by including images of the source. In Figure 10 the positive and negative sign, before the source and its image, stands for photon flux going out of the medium and reflected into the medium at a boundary. Aronson (1995) provided a modification to the extrapolation length based on relative refractive index.

Martí-López et al. (2004) introduced a new diffusion coefficient by incorporating a divergence coefficient for a point source. They defined three propagation regions namely near field, middle field and far field depending on the distance from a point source and concluded that the inaccuracy of the diffusion equation near a point source is due to the missing divergence term. The near field solutions incorporating the divergence term were compared with near field Monte Carlo simulations and found to be in good agreement. This supports their view that the missing divergence term is an important source of error near the source.

The accuracy of the diffusion approximation close to a source has been improved for frequency domain photon migration by proposing a δ - P_1 approximation. You et al. (2005) introduced a Dirac delta function (Joseph et al. 1976) to both the radiance and phase function approximation in radiative transport equations. They compared the results from δ - P_1 approximation and standard diffusion approximations to Monte Carlo simulation results and found that δ - P_1 results were superior. Another important observation was the ability of the δ - P_1 method to provide excellent phase delay predictions over a wide range of source-detector separations and media with ratio of scattering to absorption coefficients from 1, 3, 30, and 300. The δ - P_1 model was able to recover the optical properties of solid and liquid phantoms, from spatially resolved reflectance measurements, within $\pm 22\%$ and $\pm 18\%$ errors, while for the standard diffusion theory these errors were $\pm 29\%$ and $\pm 25\%$; respectively (Seo et al. 2008).

2.5 Therapeutic window and typical optical property values

The validity of the light propagation models discussed here strongly depends on the range of optical properties (μ_a and μ_s') of the media. The typical range of optical property values encountered in tissue optics is discussed in this section. In the near infrared wavelength range, the main absorbers in human tissue are haemoglobin, oxy-haemoglobin and water. The absorption spectra of these three main components are plotted in Figure 11.

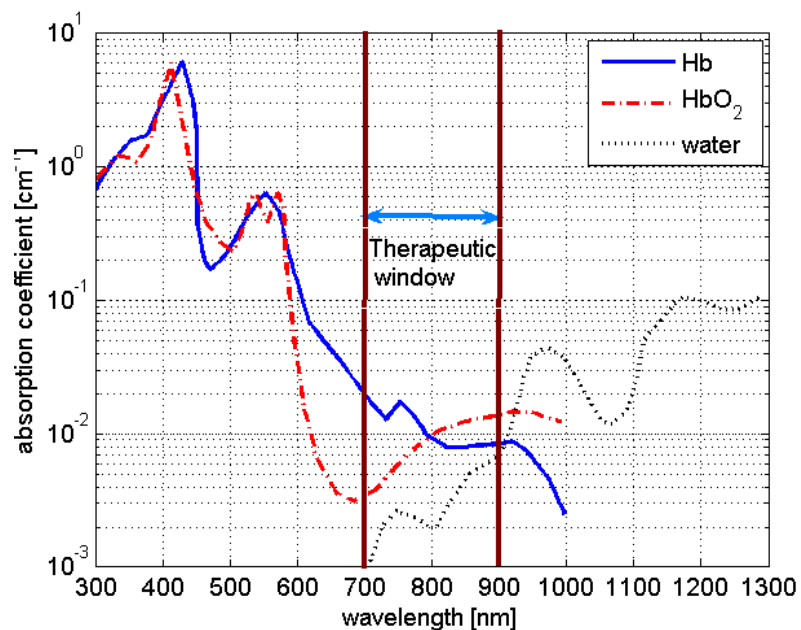


Figure 11 Absorption spectra of haemoglobin, oxy-haemoglobin (Prahl 1998) and water (Hale and Query 1973) plotted against wavelength.

From Figure 11 there is an obvious window between 700 nm, below which haemoglobin absorption increases drastically, and 900 nm, above which water absorption increases rapidly. In this region light penetrates a few centimetres inside tissue, making the wavelength region ideal for diagnosis and treatment. In biomedical photonics this wavelength range is usually called the “therapeutic window” (Jobsis-vanderVliet 1999). In the near infrared region typical tissue absorption ranges from 0.02 cm^{-1} to 0.3 cm^{-1} . In the therapeutic window the tissue is highly scattering and the

reduced scattering coefficient of biological tissue ranges from 2 to 20 cm^{-1} (Cheong et al. 1990).

The absorption and scattering properties of some fruit and vegetable tissues are plotted in Figure 12. In fruit and produce, the strong absorber chlorophyll dominates below 700nm and water again shows up at 900 nm, thus making the “window” applicable to spectroscopy of agricultural produce.

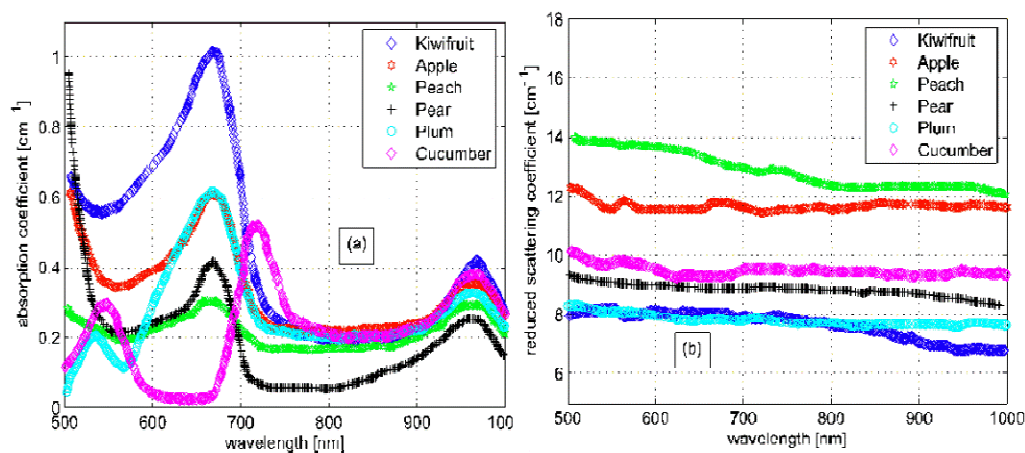


Figure 12 Absorption (a) and reduced scattering (b) coefficients of some fruits and vegetables plotted against wavelength (Qin and Lu 2008).

2.6 Tissue simulation phantoms

In biomedical optical research materials that mimic the optical properties of biological tissue are used to study light transport. These materials are termed as tissue simulating ‘Phantoms’. The ever growing clinical applications of light and instrumentation development have resulted in the need for new tissue simulation phantoms. Pogue and Patterson (2006) give a comprehensive overview of the tissue simulation phantoms used in biomedical optics research. Usually the scattering and absorbing particles are added to a base substance to fabricate a phantom. This base substance can be liquid or solid. Some of the liquid phantoms are milk, oil, fat or lipid added to water. Titanium dioxide scatterers embedded in polystyrene resin is an example of a solid phantom. Intralipid® (used in

this research) is a commercially available liquid phantom and widely used in biomedical optics research.

Intralipid is sterile fat emulsion, milky white in colour, used intravenously to feed weak patients providing the body with energy and fat. Intralipid can be diluted to make the optical scattering properties similar to many biological tissues also adding dye to make absorption properties similar. The emulsion is made of soybean oil, egg lecithin, glycerine and water. The scattering property of Intralipid arises due to the encapsulation of soybean oil by a monolayer membrane of lecithin. The name Intralipid, “inside the lipid”, arises from this property (van Staveren et al. 1991).

Intralipid is available in glass bottles or plastic bags in three strengths namely 10%, 20% and 30% indicating the lipid content. This means, Intralipid 10% contains 10 grams of lipid per 100 ml of solution. The constituents of a 500 mL, Intralipid[®]-20% bottle are as follows.

- Soybean oil 100 g 107.88 ml
- Lecithin 6 g 5.82 ml
- Glycerine 11 g 8.72 ml
- Water 376.85 g 377.5782 ml

Optical properties of Intralipid have been reported by many groups using different photon migration methods over different wavelength regions (van Staveren et al. 1991; Flock et al. 1992; Michels et al. 2008). The optical absorption of two major Intralipid components in the near-infrared wavelength region is illustrated in Figure 13. The reduced scattering coefficient of Intralipid was found to obey a power law

dependence on wavelength given by $\mu'_s = 9.3\lambda^{-1.4} - 1.6\lambda^{-2.4}$ (van Staveren et al. 1991).

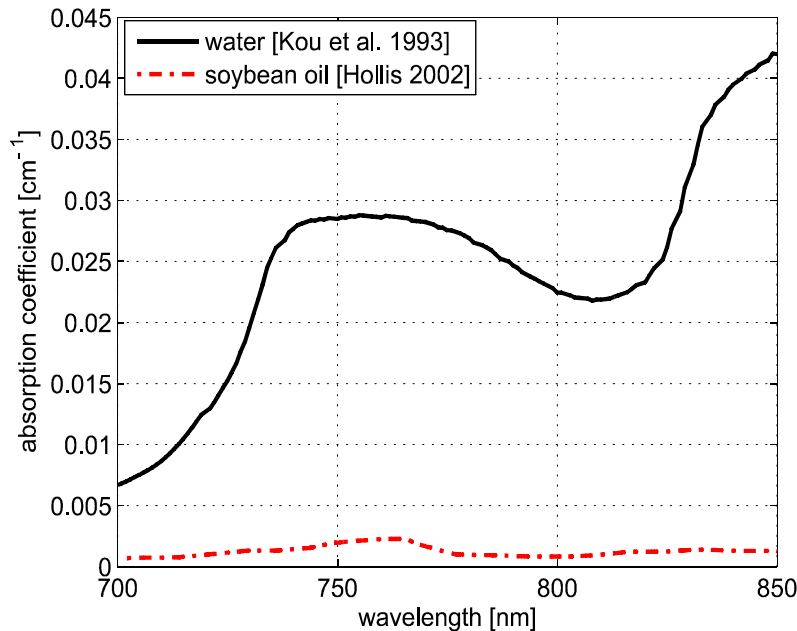


Figure 13 Absorption coefficients of two major components of Intralipid, water (Kou et al. 1993) and soybean oil (Hollis 2002), plotted against wavelength.

Temperature induced changes in the optical properties of Intralipid® have also been reported. Kakuta et al. (2008) reported the temperature dependence of absorbance at 1440 nm using a spectrophotometer and proposed a method to measure the temperature of turbid aqueous solutions, but did not recover the absorption coefficient. McGlone et al. (2007) determined the temperature dependence of absorption and reduced scattering coefficients of Intralipid® using continuous wave photon migration measurements from 700 to 1000 nm. The authors relied on measurement of attenuation close to the source to separate scattering and absorption. The changes in absorption coefficients due to temperature were attributed to water (Collins 1925; Langford et al. 2001) the main absorbing species in Intralipid® (Flock et al. 1992; van Staveren et al. 1991). Kakuta et al. found a discrepancy in absorption between heating and cooling cycle measurements and linked it to irreversible changes in the

scattering properties of the micelles. McGlone et al. observed a lack of repeatability, during heating and cooling, in temperature induced changes in the reduced scattering properties.

2.7 Summary

The basics of various light propagation models in turbid media have been discussed along with the diffusion theory in detail. The solution of the photon diffusion equation for modulated light transport in turbid medium are strongly damped spherical harmonic waves. It is shown that the absorption (μ_a) and reduced scattering (μ_s') coefficients of a turbid medium can be estimated by measuring the diffuse photon density wave generated inside the medium by an intensity modulated light source. The accuracy of the optical properties estimated based on diffusion approximation is discussed by reviewing the literature. The light propagation model using diffusion approximation to radiative transport equation estimates the optical properties within 10% when measurements are made away from sources and boundaries.

CHAPTER 3

PHOTON MIGRATION INSTRUMENTATION

3.1 Introduction

This chapter gives a brief overview of the various geometries, instrumentation methods and sensors for photon migration measurements. Almost all photon migration instruments comprise a light source, a detector and an interpreter as shown in Figure 14.

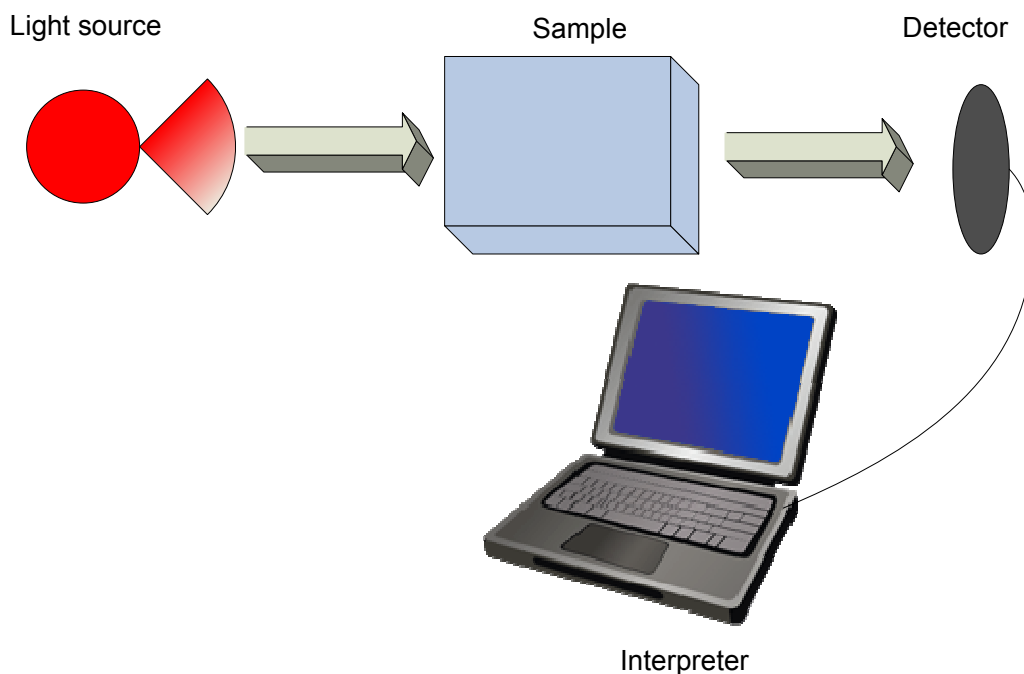


Figure 14 Photon migration instrument.

Sources used in the instrumentation range from incandescent light bulbs to picosecond lasers. Light emitting diodes and laser diodes are two types of universal sources used, because of their compact nature, low cost and ease to intensity modulate. Detectors are selected based on the operating wavelength of the source and the light levels encountered after reflection or transmission from the sample. A wide range of detectors has been employed for photon migration instruments from ordinary photodiodes to

ultra sensitive micro channel plate photomultiplier tubes. Avalanche photodiode and photomultiplier tubes are two most commonly used detectors in photon migration instruments because of their ability to detect low light levels. Time domain instruments sometimes use streak cameras and charge coupled detector devices. The interpreter in most cases is a computer in conjunction with some extra signal processing electronics.

A review of the earlier stages of instrumentation development can be found in Chance (1991). Following the range of experimental methods discussed in chapter 2, the instrumentation falls into three general categories: continuous intensity (space resolved), time domain and frequency domain (Delpy and Cope 1997; Rolfe 2000). Each category dictates its own approaches to lighting. For continuous intensity measurements, the source emits light at constant amplitude and the light intensity at a position a few centimetres away from the incident point is measured. In the time domain, an ultra short light pulse, usually pulse width in the picosecond range, is applied to the scattering medium and the emerging intensity is detected as a function of time. In the frequency domain the source intensity is modulated to radio frequencies and the intensity and phase shift of the detected light are measured. The frequency domain and time domain approaches are identical mathematically, linked through the Fourier transform (Hoshi 2005).

There has been some effort to assess the performance of the instrumentation in the measurement of optical properties exploring accuracy, linearity, noise, stability and reproducibility (Pifferi et al. 2005). On the basis of these properties Pifferi et al. proposed a protocol named Optical Methods for Medical Diagnosis and Monitoring of Diseases (MEDPHOT). This protocol defined accuracy as the capability of the instrument to measure a quantity as close as possible to the conventionally accepted true value. Linearity of the instrument was assessed by making

measurements in a set of phantoms containing absorbers and scatterers at a number of concentrations. The plots of measured optical property against concentration were considered a measure of linearity and also were able to reveal any coupling between the absorption and scattering measurements. The definition of noise was related to the sensibility of the instrument as it was the lowest detectable change in a measured quantity. Stability of the instrument setup was assessed by making measurements on the same phantom at subsequent time intervals. For the reproducibility check measurements were done on the same phantom under the same experimental conditions on different days. A phantom based on epoxy resin with TiO_2 powder as scatterers and black toner as absorbers was distributed to research institutes in five countries. Of the eight instruments tested two were continuous wave and the rest was time domain. No frequency domain instrumentation was tested in this study.

3.2 Continuous intensity measurements

In continuous intensity type instrumentation, the intensity reflected from

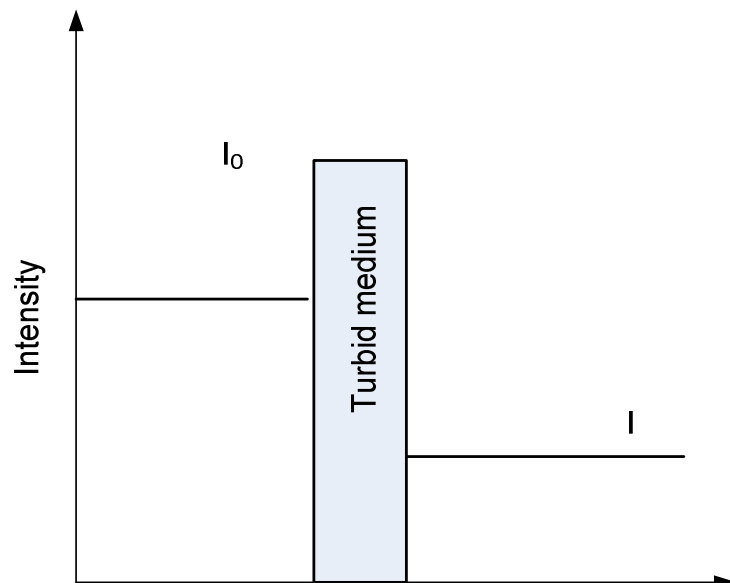


Figure 15 Continuous intensity measurements.

or transmitted through the turbid medium is measured as illustrated in Figure 15. The intensity of the light source is denoted as I_0 , and after interacting with the turbid medium the intensity reduces to I . Continuous wave instruments measure this reduction in intensity to estimate the optical properties. The continuous intensity measurements can be accomplished at fixed source detector separations, measuring the intensity at various wavelengths, or at multiple source detector separations.

Reynolds et al. (1976) calculated the diffuse reflectance of blood using a tungsten light source and optical fibres for light delivery and detection. The detector fibre coupled to a photomultiplier tube with output connected to a lock-in amplifier recorded the voltage generated; this setup was used to monitor the oxygen content in blood. They got agreement between theoretical and experimental results within 10% indicating the potential of the instrumentation design. A similar setup was used by Farrell et al. (1992) with photodiodes for light detection. The probe contained ten 400 μm optical fibres, one of them acting as the source fibre. The detector fibres were placed at distances ranging from 1 to 10 mm from the source fibre. Farrell et al. made optical property measurements in lipid emulsion at various concentrations by placing the fibre probe on the surface of the liquid. Their results were within 5 to 10% accurate to other reported values of optical properties. Continuous intensity instrumentation has been reported by many groups using laser diodes, halogen lamp and other continuous wave lasers as sources and with photodiodes, photomultiplier tubes and CCD cameras as detectors (Bays et al. 1996; Nichols et al. 1997; Bevilacqua et al. 1999; Kienle et al. 1996).

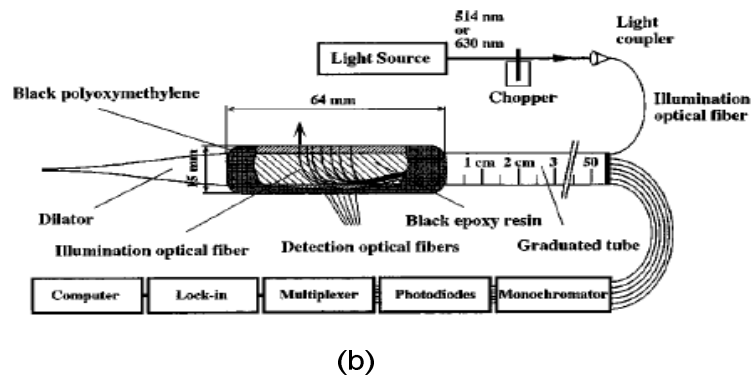
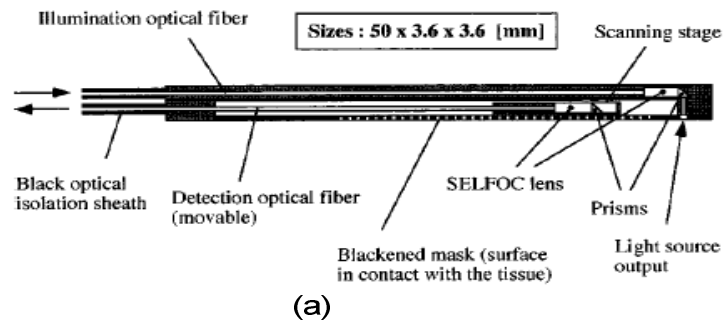


Figure 16 Fibre probes, (a) and (b), used by Bays et al. (1996) to make optical property measurements; (b) is similar to fibre probes used in photodynamic therapy (reproduced).

Bays et al. (1996) used a fibre probe as shown in Figure 16 (a) with two optical fibres, with the first fibre fixed to the probe and acting as a source fibre for the light delivery. The second fibre was moveable and measures the backscattered light at different distances from the illumination point. These fibre movements were controlled by a computer. The diffusively reflected light was detected by a photomultiplier tube and the amplified signal was detected by the lock-in technique. Bays et al. used this setup to calculate the optical properties of polyoxymethylene samples from diffuse reflectance. They calculated the effective attenuation coefficient and reduced scattering at 633 nm with accuracies of 21% and 32%, respectively. Bays et al. used another fibre probe as shown in Figure 16 (b), similar in geometries to that used in photodynamic therapy, and made optical property measurements, at wavelengths 514 and 630 nm, of the inner wall of the oral cavity. With the preliminary results obtained from

these measurements they were able to optimize the photodynamic therapy parameters for early superficial cancers in oral cavity tissue. This demonstrates even relatively low precision measurements can provide useful results.

Nichols et al. (1997) used a circular fibre optic probe with fifteen 200 μm fibres arranged on the perimeter of a 2 cm diameter circle as shown in Figure 17.

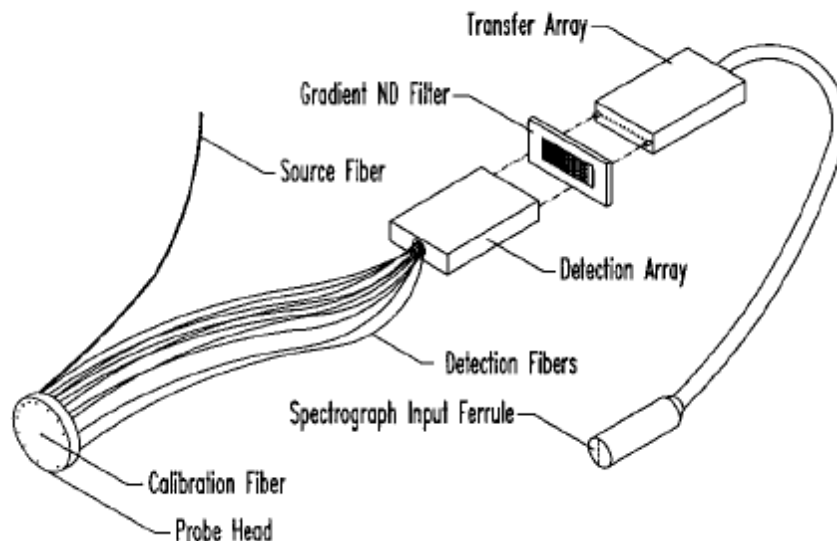


Figure 17 Fibre probe used by Nichols et al. (1997) for optical property measurement (reproduced).

The source fibre was also mounted on the circular probe such that the detector fibres were located at radial distance of 1 to 20 mm from the source fibre. Another fibre, 400 μm in diameter, mounted in the centre of the circular probe was used for calibration. A 250 W tungsten halogen lamp was used as the source; the fibre coupling delivered a power of 200-250 μW through 10 nm bandpass filters in the wavelength range 550-850 nm. The detection fibres were imaged through a low resolution, high dispersion grating onto a cooled CCD camera. This arrangement was used

to record the diffuse reflectance at different wavelengths. Optical property measurements were conducted in Lyposin-II at various absorber concentrations. The absorption and reduced scattering coefficients estimated from these measurements were compared with the Monte Carlo calculations. This comparison found the absorption coefficients were within 10 to 13% and the reduced scattering coefficient within 5 to 8% of the values of Monte Carlo calculations. This instrument setup had a lower limit of the absorption coefficient that can be accurately measured of 0.001 cm^{-1} . However this setup measured absorption coefficients as high as 0.35 cm^{-1} with an accuracy of 10%.

Kienle et al. (1996) used a He-Ne laser at 633 nm and a laser diode at 751 nm as source in separate experiments to estimate the optical properties of bovine muscle, adipose, chicken muscle, and liver tissue by measuring the diffuse reflectance. The laser beam was deflected onto the specimen by a mirror at an angle of incidence of 5° to 10° to avoid specular reflections. A CCD camera, with a 14 bit analogue to digital converter, giving a dynamic range of approximately 10^4 was used to detect the diffusively reflected light. In some of their experiments linear polarisers were used in the path of light delivery and detection to study the effect of state of polarisation on diffuse reflectance. The performance of the setup was evaluated by making optical property measurements in tissue simulating phantom Intralipid containing an absorber. Kienle et al.'s results demonstrated that diffusion theory does not provide an accurate calculation of diffuse reflectance at distances between 2 and 12 mm from the source. This was contrary to results obtained by Jacques et al. (1993) and another notable difference was the error reported in absorption and scattering. Jacques et al. reported larger errors in reduced scattering than absorption coefficient, but Kienle et al. observed the opposite.

Bevilacqua et al. (1999) used laser diode sources and an optical fibre probe as shown in Figure 18 to make diffuse reflectance measurements and calculated the optical properties of Intralipid and normal and abnormal human brain tissue.

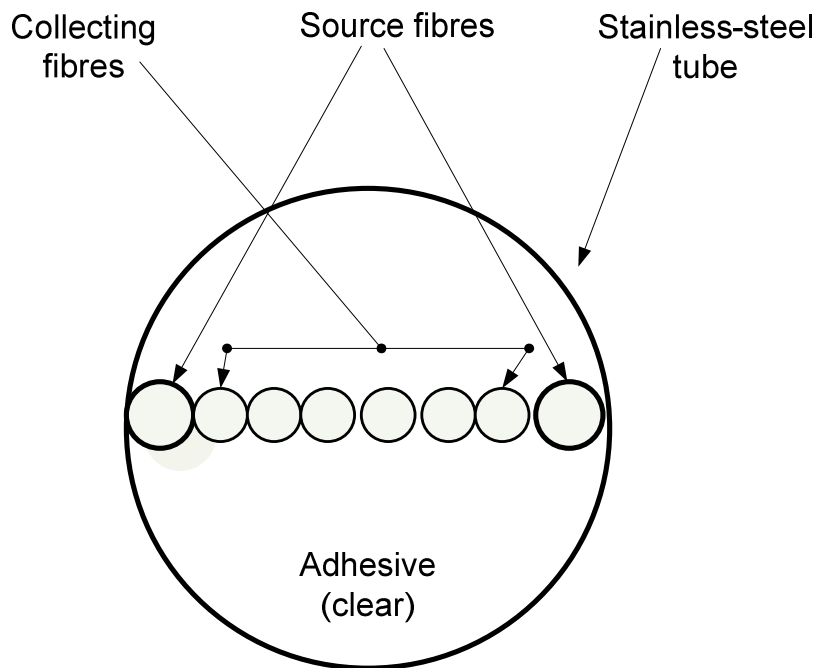


Figure 18 Fibre probe geometry used by Bevilacqua et al. (1999) to make optical property measurements.

The probe consists of a linear array of optical fibres with $200\ \mu\text{m}$ core diameters and numerical aperture of 0.37 in air. Two source fibres used to illuminate the tissue were positioned symmetrical to the collection fibres. Four laser diodes (674, 811, 849 and 956 nm) were used in conjunction with an optical switch to illuminate the tissue. Two additional laser diodes at 675 and 825 nm were used in the Intralipid measurements. The backscattered light collected by the fibre array was imaged using a linear CCD. The entire system was controlled by a computer. The measurement in human brain tissue demonstrated excellent discrimination between normal and abnormal tissues. They got agreement of the order of 10% to 25% between the spatially resolved reflectance and frequency domain photon migration measurements in the case of reduced scattering

coefficient of cortex and skull. The absorption coefficient measured by frequency domain method was 50% smaller compared to spatially resolved reflectance measurements. This was attributed to the sensitivity of spatially resolved technique to haemoglobin concentration at small source detector separation. However the frequency domain measurements interrogated a large tissue volume averaging the absorption coefficient.

Dam et al. (2001) reported a probe for reflectance measurement which consists of a source optical fibre (200 μm) in the centre of a circular disc surrounded by equally spaced detector fibres (250 μm) in concentric rings. The fibres corresponding to each concentric ring are bundled and terminated in separate silicone photodiodes. The source fibre was coupled to four different fibres connected to laser diodes emitting 660, 785, 805 and 974 nm. The data acquisition and analysis was done with a digital signal processing board connected to the silicon diodes, laser diode sources and a computer. Measurements made in Intralipid-ink phantoms were able to extract absorption and reduced scattering coefficients with an accuracy of 11% and 4% respectively at all wavelengths except at 660 nm. The maximum error for absorption 660 nm was found to be 18%. This setup was used to measure the optical properties of skin tissue, and they got consistent results for all wavelengths except 660 nm.

A continuous wave spectroscopic system using laser diodes and photodiode detectors was reported by Hulvershorn et al. (2003). This system was used in a magnetic resonance image scanner to monitor the oxygen saturation state in human brain. This instrument was able to estimate the difference in concentration of oxyhaemoglobin and deoxyhaemoglobin with an accuracy of 10%.

Van Staveren et al. (1991) reported the absorption, anisotropy and scattering coefficients of Intralipid by making continuous wave

measurements at four wavelengths. These measurements were made by immersing the source fibre in tissue simulating phantom and measuring the fluence rate at different distances using another fibre. Three continuous wave laser sources were used in this study namely He-Ne, Ar⁺, and Nd:YAG. The detection setup incorporated a photodiode and lock-in amplifier. Zaccanti et al. (2003) used a similar setup with a He-Ne laser source. A photomultiplier tube was used as a detector. Fluence rate measurements were made with the source and detector fibres immersed in the medium. The experimental results for scattering coefficient and scattering anisotropy were within 6% of those calculated from Mie theory.

Martelli and Zaccanti (2007) used a similar setup by replacing the He-Ne laser source van Staveren used with a laser diode and made fluence rate measurements in tissue simulating phantom with a standard error less than 1%. The absorption and reduced scattering coefficients of Intralipid 20% were measured with errors lower than 2% and 5% respectively.

Table 1 Summary of continuous wave measurements [PMT-photomultiplier, PD-photodiode, CCD-charge coupled device, LD-laser diode]

Work by	Light Source	Detector	Medium	Results
Reynolds et al. (1976)	Tungsten lamp	PMT	Human blood	oxygen content in blood with an error within 10%
Van Staveren et al. (1991)	He-Ne, Ar ⁺ and Nd:YAG Lasers	PMT	Intralipid 10%	Highly cited characterization of Intralipid – μ_s errors of order of 4%
Farrell et al. (1992)	Tungsten lamp	PD	Indian ink in Liposyn	μ_a & μ_s within 5% to 10%
Kienle et al. (1996)	He-Ne and LD	CCD Camera	Tissue and Intralipid	SDE does not provide accurate results near source (2 to 12 mm)
Bays et al. (1996)	Argon ion, He-Ne or dye laser	PMT	Tissue phantom oral cavity tissue	μ_t & μ_s with 21% and 32% accuracy
Nichols et al. (1997)	Tungsten halogen lamp	CCD camera	Liposyn II	μ_a error 10% μ_s error 8%
Bevilacqua et al. (1999)	LD	CCD array	Intralipid, brain tissue	normal and abnormal tissue discriminated
Dam et al. (2001)	LD	PD	Intralipid skin tissue	accuracy μ_a 11% μ_s 4%
Zaccanti et al. (2003)	He-Ne Laser	PMT	Intralipid	errors μ_a 2% μ_s 5%
Martelli and Zaccanti (2007)	He-Ne Laser	PMT	Intralipid	fluence rate with standard error < 1%

A continuous wave near infrared system for monitoring the brain hemodynamic of newborns was reported (Bozkurt et al. 2005). This was a portable, low cost system operating with batteries. The system employed a light emitting diode with adjustable power output as source. They used monolithic photodiode/preamplifier integrated circuits for detection. The source and detector was arranged using a flexible circuit technology to fit the optode to the curved surface of head. The validity of the instrumentation was tested by making measurements in tissue simulation phantom Intralipid as well as newborns in a clinical environment. These measurements indicated that the system can be used to monitor functional changes in blood volume and oxygenation.

3.3 Time domain measurements

Time resolved instrumentation employs a short (picoseconds) light pulse to interrogate the turbid medium. The emerging pulse intensity from the medium under investigation is detected as a function of time as illustrated in Figure 19. This pulse envelope is stretched and attenuated as the light is scattered and absorbed by the medium. The journey taken by the photons can be classified into three categories: ballistic, snakelike and diffuse. Ballistic photons, the first to arrive at the detector, pass through the sample without being scattered. Ballistic photons are only observed in transmission geometries with optically aligned source and detector. As the concentration of scatterers and sample thickness increases, the number of ballistic photons decreases and in many samples no ballistic photons may be detected.

Snake photons, after experiencing a few scattering events, travel in near straight paths and arrive after the ballistic ones as shown in Figure 19. The important point about ballistic and snake photons is that they retain a “memory” of their initial generation direction. Snake photons are used in imaging applications of turbid media. Gopal et al. (1999) demonstrated by

experiments and Monte Carlo simulations that by monitoring snake photons images can be recovered to a depth far in excess predicted by diffusion theory. Diffuse photons experience multiple scattering as a result their pathlength is altered significantly. In addition to the reduction in intensity this method records the photon arrival time. With the additional parameter the quantification of optical properties can be much improved (Hoshi 2005).

Theoretical details of the pulse propagation in turbid medium can be found in (Ishimaru 1978b). Ishimaru introduced the term “Diffusion” (Ishimaru 1978a).

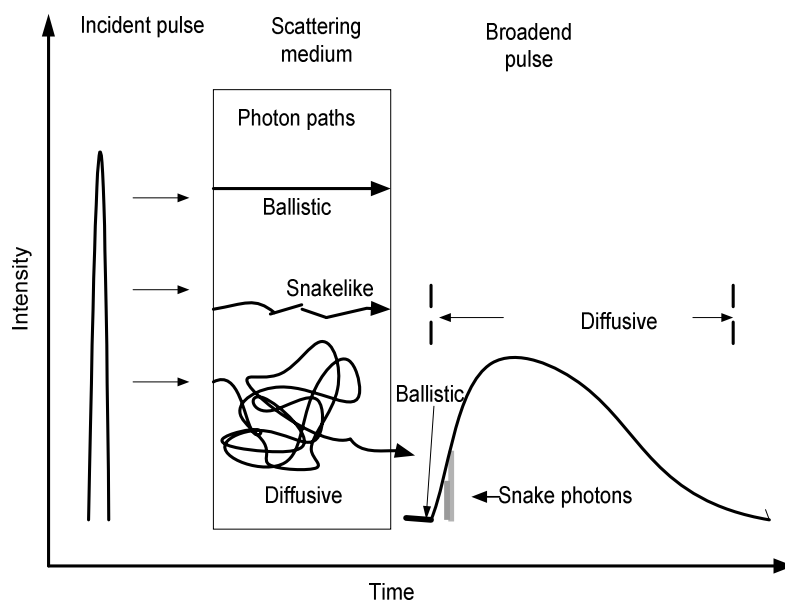


Figure 19 A short light pulse propagating through a scattering medium spreading into ballistic, snakelike and diffuse photons.

Chance et al. (1988) used a system where a dye laser emitting 130 ps pulses was used to illuminate a tissue. The detector placed 3 cm from the source observed a pulse broadened to 600 ps. The scattered light was collected by a 3 mm fibre bundle and detected by a two stage micro channel plate. The time resolution of the system was 150 ps. This system

was used to monitor the change in haemoglobin and myoglobin in ischemic muscle.

Delpy et al. (1988) used a mode locked krypton ion laser emitting 100 ps pulses and made measurements in tissue phantom and rat brain. The system employed a streak camera and silicon photodiode at the detector stage. They introduced the temporal point spread function for the pulse propagation in turbid media. The setup included another ultrafast dye laser, which was pumped by the source laser. The streak camera was also triggered by the source laser. The temporal spread was calculated by autocorrelation methods. A Monte Carlo simulation showed excellent agreement between the temporal point spread function and the differential path length analysis and further verified the temporal point spread function by making measurements in a medium with known optical properties. Delpy et al. carried out path length measurements in rat brain and concluded that these path lengths permit the quantification of cerebral oxygenation derived from near infrared spectroscopy.

Andersson-Engels et al. (1993) reported time resolved instrumentation as illustrated in Figure 20 with an argon-ion-laser pumped passively mode locked Ti:Sapphire laser emitting 100 fs pulses with an average power of 1 W. They reported measurements with transmitted pulse in porcine muscle 14 mm thick in a confocal geometry. A cooled (-30°C) CCD streak camera was used as a detector. This experimental setup employed a water cuvette and gratings to adjust pulse width and energy. The output pulse was spectrally chirped to 260 fs duration. This chirping reduces the peak power from 120 kW to 8 W. Another pair of gratings compressed the pulse to 200 fs and produced pulses at 792 nm with peak power of 1.1 TW. The high peak power pulses were focused onto a 30 mm thick water cuvette, which resulted in pulses over the entire visible and near infrared region due to self phase modulation. The emerging pulses had the same pulse

width and beam qualities of the incoming laser. The pulses were collected, filtered and focused to the sample to make measurements. The pulses transmitted through a 14 mm thick porcine muscle were collected and recorded. The recorded image was able to reveal the haemoglobin absorption between 540 and 580 nm and below 470 nm. Thus by using a short pulse this method was able to record the absorption and scattering properties of tissue over the whole visible spectral range. By shifting the wavelength, this technique could be extended into near-infrared wavelengths.

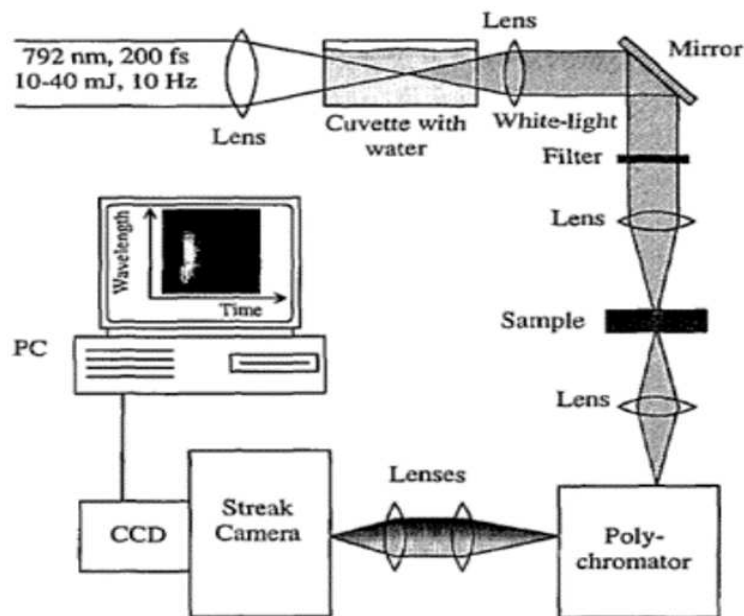


Figure 20 Time resolved instrumentation reported by Andersson-Engels et al. (1993) (reproduced).

Time resolved transmittance measurements were also reported in aqueous latex particle suspensions. Brewster and Yamada (1995) used a pulsed laser diode, operating at 784 nm, as a source and an optical oscilloscope measured the transmitted pulse. The schematic diagram is illustrated in Figure 21. The optical oscilloscope represents a combination of a streak camera and a sampling oscilloscope. The source pulse had a full width at half maximum of 50 ps. The incident laser beam was collimated and a

small fraction of which was split-off and used to convolute the transmitted pulse. The transmittance profiles measured were compared with Monte Carlo simulations. This comparison showed that the long-time asymptotic log pulse slope and rms pulse width are described by analytical expressions of diffusion theory. The nonhomogenous properties of the medium were not considered in this study. Though, most of the real tissue samples are nonhomogenous.

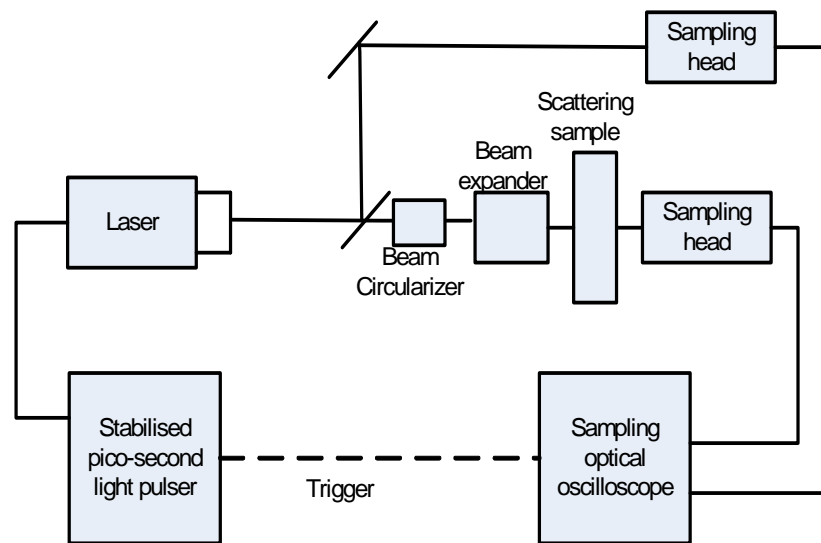


Figure 21 Schematic diagram of time resolved transmittance measurement by Brewster and Yamada (1995).

Berg et al. (1996) reported time resolved transillumination measurements in plastic tissue like phantoms with a mode locked argon-ion laser pumping a dye laser. The pulse length (6 ps) was measured with autocorrelator. The 670 nm laser output had a repetition rate of 10 MHz. Optical fibres were used to illuminate the sample and collect the transmitted pulse. The transmitted light was collected by a 600 μm fibre and focused to the detector through an interference filter to reduce ambient light. A fast micro channel plate photomultiplier tube was used to detect the light. Time-correlated single-photon counting was used to accurately detect the transmitted pulse. This method is accurate and is very efficient so it is used in most time domain instruments at present.

Time correlated single photon counting is based on the detection of single photons of a repetitive light signal, the measurement of the detection times of the individual photons and the reconstruction of the waveform from the individual time measurements as illustrated in Figure 22 (Becker et al. 2004).

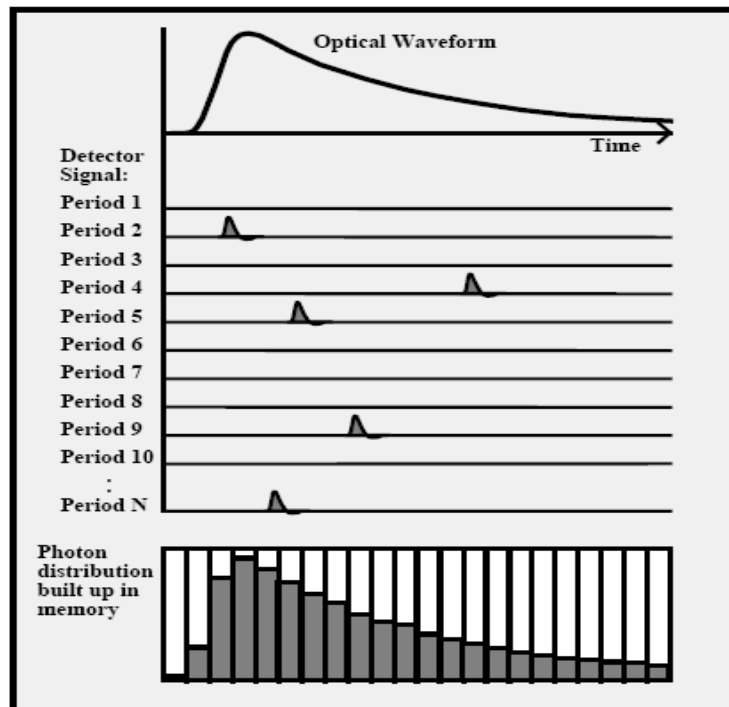


Figure 22 Principle of time correlated single photon counting (Becker et al. 2004).

A computer simulation was proposed by Bays et al. to model the light transport in tissue and compared to experimental results in phantom measurements. They found that this simulation model can solve the diffusion equation numerically and can be applied to study tissue inhomogeneities.

Cubeddu et al. (1997) also reported time resolved transmittance measurements in a solid tissue phantom using time-correlated single-photon counting. This measurement was made in a solid phantom prepared from highly purified agar powder dissolved in distilled water added with Intralipid and India ink. Output pulses from argon pumped

mode-locked dye laser (650 nm) was coupled to 1 mm fibre and delivered to the sample. An identical fibre collects the light transmitted through the sample delivering it to a micro channel plate photomultiplier tube. Time correlated single photon counting was used for the signal analysis. The optical property measurements indicated that the prepared solid phantom has good repeatability among different preparations.

Time of flight measurements were reported in tissue simulating phantom Intralipid® by Bondani et al. (2003). They used a diode pumped Nd:vanadate laser emitting 9 ps pulses at 1064 nm as a source. The 1064 nm light was converted to its second harmonic at 532 nm using a KDP crystal. Graded index lenses were used to couple and collect the light emerging from the sample. Light collected by the grin lens was coupled to a single mode fibre and delivered to a single-photon avalanche diode for detection. More details about single-photon avalanche diode detection technique can be found in Cova et al. (1996). Using this setup Bondani et al. estimated the reduced scattering coefficient of Intralipid at various concentrations (from 1% to 10% weight to volume). They found that the dependence of reduced scattering on the concentration of scattering sample is nonlinear and has a quadratic dependence.

A dual wavelength (690 and 820 nm) multi-channel time resolved system using 16 sources and 64 collection points was reported by Contini et al. (2006). The lasers were coupled to graded index optical fibres through a coupling system incorporating a neutral density filter and variable attenuator and a standard fibre coupler. The system employed the time correlated single photon counting technique and four channel compact photomultiplier tubes for detection. The system was controlled by a computer through custom made software. The system was tested against linearity, noise, stability and reproducibility (Pifferi et al. 2005) by comparing measurements of absorption and reduced scattering

coefficients in a solid phantom specified in Pifferi et al. (2005). The instrument performance was also evaluated by making measurements of hemodynamic parameters in left and right forearm muscle and optical response of human brain.

A broadband time domain spectroscopic system for the measurement of absorption and scattering was reported by Pifferi et al. (2007). This system was fully automated and operated with mode-locked lasers tuneable in the 550-1050 nm range. An acousto-optic modulator was used for the mode-locking purpose in this system. The detection was again based on time-correlated single photon counting mentioned earlier with a photomultiplier tube as detector. This system was tested against all the five criteria-accuracy, linearity, noise, stability and reproducibility-mentioned (Pifferi et al. 2005) for photon migration instrumentation. The accuracy of the measurement was tested by making optical property measurement in a water solution of Intralipid, then comparing the measured absorption coefficient to that of pure water absorption. This procedure showed a maximum error of 27% around 730 nm and a median error of 7% around the whole wavelength range. Even though the calculated reduced scattering was linear at lower absorption coefficient, high values of absorption produces an offset of the linearity plot. The poor performance of the system regarding noise was attributed to the low quantum efficiency of the photo cathode surface to cover the range up to 1.1 μm . In the test for stability and reproducibility the instrument setup produced a coefficient of variation (precision) of 5.6% for absorption and 6.5% for reduced scattering.

Almost all of the instrumentation mentioned here uses light pulses in the picosecond time range. In contrast Calba et al. (2008) describes the propagation of femtosecond pulses through strongly scattering media. They used a Ti:sapphire regenerative amplifier emitting 100 fs pulses at a

repetition rate of 1 kHz at 800 nm. This probe pulse was split-off into two in a 10/90 beam splitter and the energetic one, after passing through a delay line, impinges the scattering cell. The pulse emerging from the scattering cell and the lower energy pulse was correlated in a beta barium borate crystal. A superposition of the pulses was detected by a photo multiplier tube. They demonstrated that the potential use of femtosecond pulses for investigating optical properties of highly scattering media by making measurements in polystyrene particles immersed in water.

Table 2 Summary of time domain measurements [PMT-photomultiplier, PD-photodiode, CCD-charge coupled device, LD-laser diode, MCP-micro channel plate]

Work by	Light source	Detector	Medium	Results
Chance et al. (1988)	Dye laser (pulse width 130 ps)	MCP	tissue	changes in haemoglobin and myoglobin in ischemic muscle
Delpy et al. (1988)	mode locked krypton ion laser (100 ps)	streak camera, silicon PD	tissue phantom, rat brain	temporal point spread function quantification of cerebral oxygenation
Andersson-Engels et al. (1993)	passively mode locked Ti:Sapphire laser (100 ps)	CCD streak camera	porcine muscle	absorption and scattering properties of tissue over the whole visible spectral range
Brewster and Yamada (1995)	Pulsed laser diode	optical oscilloscope	aqueous latex particle suspension	
Berg et al. (1996)	Dye laser pumped by a mode locked argon ion laser	MCP	plastic tissue like phantom	Time-correlated single-photon counting was used to accurately detect the transmitted pulse
Cubeddu et al. (1997)	mode-locked dye laser	MCP	solid tissue phantom	optical property measurements indicated that the prepared solid phantom has good repeatability among different preparations
Bondani et al. (2003)	diode pumped Nd:vanadate laser (9 ps)	SAPD	Intralipid®	reduced scattering on the concentration of scattering sample is nonlinear and has a quadratic dependence
Contini et al. (2006)	16 laser diodes	4 channel PMT	solid phantom, forearm muscle, human brain	system was tested against linearity, noise, stability and reproducibility
Pifferi et al. (2007)	mode-locked lasers	PMT	Intralipid	maximum error of 27% around 730 nm and a median error of 7% around the whole wavelength range the instrument setup produced a coefficient of variation of 5.6% for absorption and 6.5% for reduced scattering
Calba et al. (2008)	Ti: Sapphire regenerative amplifier	PMT	Polystyrene particle suspension	Concentration and detection solid angle

Time domain measurements mostly use laser sources with output pulses in the picosecond range, typical 100 ps and use fast detectors such as micro channel plates and streak cameras. Compared to conventional continuous wave and frequency domain instrumentation these components are expensive, and especially the detection electronics is complex.

3.4 Frequency domain measurements

Every frequency domain instrument consists of a light source with intensity modulated to radio frequencies and a phase sensitive detection system. Frequency domain instrumentation doesn't require demanding technology for detection unlike time domain measurements. Still giving the same information as time domain measurements as the phase delay of modulation measured is proportional to the mean time of flight. Phase delay based measurements are also sensitive to deeper structures compared to intensity based measurements. Frequency domain instruments can be fabricated with cheaper components compared to time correlated single photon counting modules and short pulse lasers used in time domain instrumentation, such as the technology commonly found in cell phones.

Figure 6 illustrates the quantities measured in frequency domain instruments. In Figure 6 light from a sinusoidally intensity modulated source interacts with a turbid medium and the emerging light is with the same modulation frequency but altered in phase and intensity. In frequency domain one measures the demodulation, intensity reduction and the phase shift introduced by the medium to estimate the optical properties.

3.4.1 Modulation

This section describes the techniques used to intensity modulate the light sources in frequency domain. The most common source, diode laser, can be easily intensity modulated by superimposing the modulation signal to the bias current (of the order of milliamperes), which is considered to be an internal modulation method. This method cannot be employed to our laser source as the bias current is of the order amperes, and modulating this current to radio frequencies is a difficult task with the present electronic components available.

Mode locking is another internal modulation method which gives extremely short duration pulses with a fixed phase relationship. This method is employed by placing an acousto-optic modulator, electro-optic modulator or a saturable absorber inside the laser cavity. Modulating the cavity gain with acousto-optic and electro-optic devices are termed as active mode locking as these devices are controlled by external signals. Saturable absorbers exhibits an intensity dependent transmission of light and the mode locking is referred to as passive. Mode locking is usually employed in the case of pulsed lasers and also Fourier analysis is needed at the detection stage.

The electro-optic modulator works based on the Pockels effect, which introduces a change in the refractive index of a material in response to a strong electric field that varies slowly compared to the frequency of light. Electro-optic modulation is an external modulation method. An electro-optic modulator needs high voltage driving signals and can cause electromagnetic interference at the detection stage. The acousto-optic effect is another external modulation technique and is discussed in detail here.

The diffraction of light by high frequency sound waves in an optically transparent medium is known as acousto-optic effect (Debye and Sears 1932; Lucas and Biquard 1932). A high frequency sound wave travelling through the medium can produce periodic variation in the index of refraction thereby transforming the medium into a diffraction grating with line spacing equal to the wavelength of the acoustic wave. Theoretical treatment of this phenomenon has been developed for the case of normal incidence of light and is known as Raman-Nath scattering (Raman and Nath 1935). In this case, a normally incident electromagnetic field will be spread out into a number of diffraction modes each with a frequency shifted up or down by an integer number of acoustic wave frequency.

In the Bragg regime only the first order diffracted beam comes out of the medium as well as the zeroth order beam which is not diffracted. This type of diffraction is known as Bragg diffraction and is discussed here as our acousto-optic modulator operates in the Bragg regime. The other applications of acousto-optics include the use of light filters, deflectors, frequency shifters. Chang (1976) gives a brief overview of the acousto-optic interaction as well as various applications and devices. A detailed theoretical approach about the phenomenon of acousto-optics can be found in Korpel (1988).

The acousto-optic phenomenon can be theoretically analysed by solving Maxwell's equations for light propagation through the medium assuming a periodically varying permittivity (Scott 1992). This is discussed on the basis of a more simple approach which analyses the effect on the basis of a photon-phonon interaction. Each phonon has an energy and momentum given by the frequency of sound waves in the medium. This photon-phonon interaction can be explained with the help of the diagram of an acousto-optic device shown in Figure 23.

The acousto-optic modulator is constructed by bonding an acousto-electric transducer to a photo-elastic crystal as shown in Figure 23. The acousto-electric transducer is usually driven by a radiofrequency electric signal, which produces a high frequency acoustic wave inside the medium. In the Bragg regime this arrangement acts as an acousto-optic deflector that gives an unmodulated first order beam along with the zeroth order beam. For the acousto-optic deflector to act as a modulator two things are necessary. First the radio frequency signal driving the transducer is amplitude modulated and second the incoming beam is focused on to the centre of acoustic column inside the crystal.

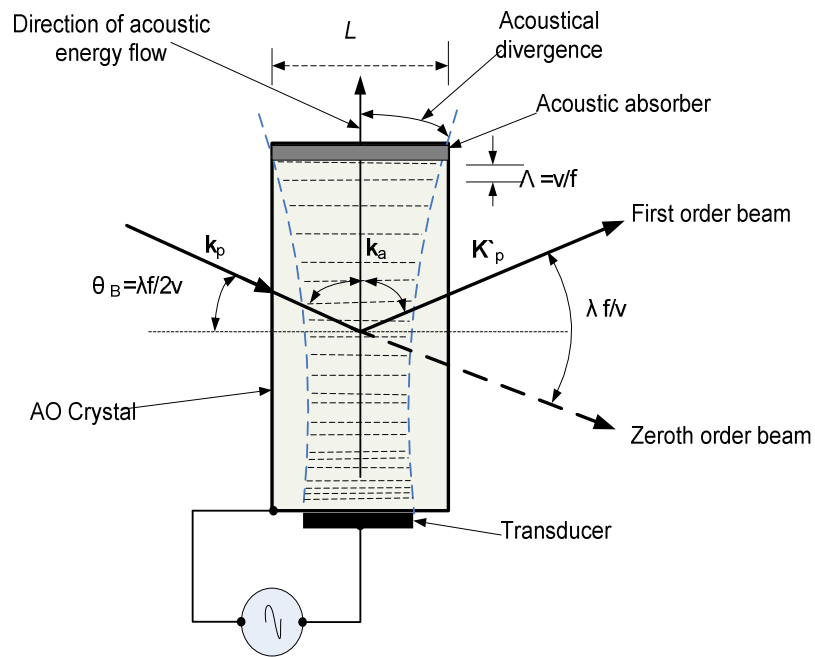


Figure 23 Schematic diagram of acousto optic modulator operating in the Bragg regime (ISOMET Corporation).

In Figure 23, the transducer is injecting an acoustic wave. Consider an incoming photon with wave vector, k_p , colliding with an acoustic phonon having a wave vector, k_a . Assuming the energy momentum conservation throughout the collision, the photon can either gain or lose energy. The outgoing photon wave vector denoted as k'_a can be written as either $k'_p = k_p + k_a$ or $k'_p = k_p - k_a$ depending on whether it gains or loses energy.

If we know k_p and k_a , then we can define the Bragg angle as the only incoming angle that conserves energy and momentum as

$$\theta_B = \sin^{-1}\left(\frac{k_a}{2k_p}\right) = \sin^{-1}\left(\frac{\lambda}{2\Lambda}\right) \quad 43$$

where λ denotes the wavelength of light and Λ is the wavelength of sound.

The two main cases of acousto-optic diffraction, Bragg and Raman-Nath, can be described by introducing a limiting factor defined as

$$Q = 2\pi \frac{\lambda L}{\Lambda^2} \quad 44$$

where L is the width of the acoustic beam inside the medium as shown in Figure 23. The Raman-Nath regime corresponds to $Q \ll 1$, which means the acousto-optic material is thin or L is small.

The Bragg regime corresponds to $Q \gg 1$ and this is accomplished by a wide slab of acousto-optic material. The main difference of Bragg diffraction is that there are only two output beams, the undiffracted beam and the principal or first order diffracted beam. The first order beam will be deflected up or down, to conserve energy and momentum, depending on the incoming beam. The modulation efficiency is defined as the fraction of incident energy transferred to the first order beam.

The modulation index, m , can be written as:

$$m = \left| \sin\left(\frac{\pi L}{\Lambda} \sqrt{\frac{MP_a}{2}}\right) \right|, \quad 45$$

were M is the acoustic figure of merit that relates the diffraction efficiency to the acoustic power for a given device geometry (Chang 1976) and P_a is the acoustic power. It is evident from equation 43 that the modulation index is directly related to the acoustic power, so the diffracted light amplitude is linearly proportional to the voltage applied to the transducer.

3.4.2 Detection

The phase sensitive detection setup in frequency domain spectrometers usually consists of a light detector and signal processing electronics. This section gives a brief overview of the commonly used detectors (photomultiplier tube and avalanche photodiode) and the phase sensitive detection electronics.

Photomultiplier tubes are vacuum tube photo detectors based on the photoelectric effect and secondary emission (Simon and Williams 1968). A schematic diagram of a photomultiplier tube along with a biasing voltage divider resistance network is shown in Figure 24.

When light strikes the photocathode located inside the vacuum enclosure, photoelectrons are emitted. The electrons are directed to the dynode, which is at a high positive potential, with help of focusing electrodes. Numerous secondary electrons are emitted after the primary electron hit the first dynode.

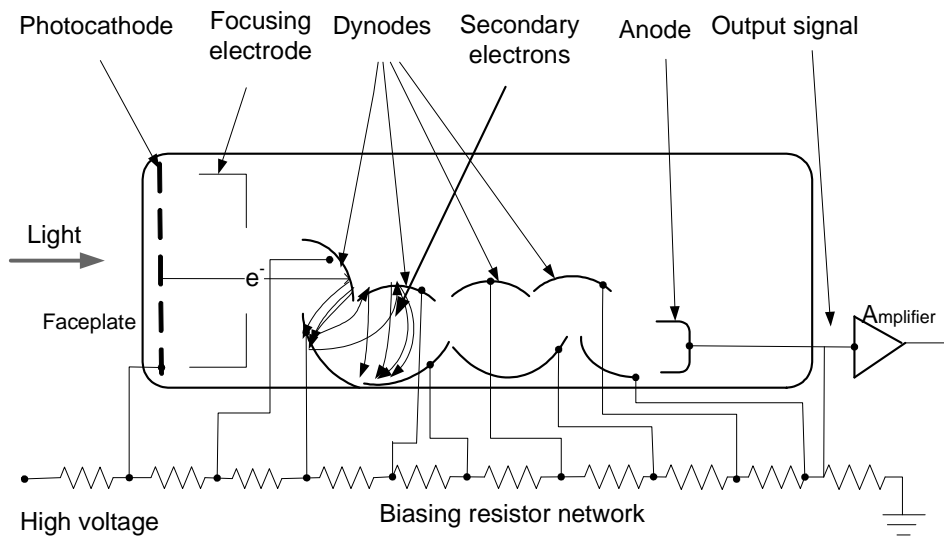


Figure 24 Schematic diagram of photomultiplier tube.

The dynodes are biased with high voltage ranging from 800 V to 2 kV. These secondary electrons are accelerated towards the other dynodes, which are at a higher potential compared to the previous dynode, multiplying the secondary electrons. This mechanism gives the photomultiplier tube gains of the order of 10^6 . The electrons from the last dynode are collected by an anode and are read out as signal current.

Photomultiplier tubes are used in numerous scientific applications (Hakamata 2006). The selection of a photomultiplier tube for a particular application depends on light wavelength, intensity, beam size and speed of optical phenomena. When selecting a photomultiplier tube based on these criteria one must take into account the signal processing electronics that follows. For a frequency domain photon migration instrument the time response of the photomultiplier selected plays an important role as the intensity modulation is in the radiofrequency range. Photomultiplier tubes usually are fast detectors as their rise time is usually of the order of 1 ns. Most of the photomultiplier tubes have very good sensitivity in the ultraviolet and visible region, but in the near infrared this sensitivity begins to decrease. The amplification of current signals from PMT output

also need to be considered with care (Becker and Hickl 2000). Considering the cost, size, power supply requirements and the wavelength of operation a silicon avalanche photodiode seems to be a better alternative.

Photodiodes are semiconductor devices operating based on the photovoltaic effect, the phenomena in which the incidence of electromagnetic radiation on a junction of two dissimilar materials induces an electromotive force (Williams 1960). In the photovoltaic effect, the electrons are not emitted out of the material surface and this is the main difference with the photo electric effect. In the case of a photodiode these dissimilar materials are a p-type and n-type semiconductors. Some photodiodes are fabricated with an undoped (intrinsic) semiconductor layer between p and n type regions and operated in the reverse bias. Light incident on the intrinsic region generates electron-hole pairs which contributes the photo current. Photodiodes can be employed either in photovoltaic or photoconductive mode to detect light depending on the application. In photovoltaic mode no external bias is applied to the photodiode and the voltage generated can be measured. However this mode of operation is not preferred in applications where fast response is needed. In the photoconductive mode a reverse bias is applied across the photodiode.

An avalanche photodiode will have wider intrinsic layer compared to ordinary photodiodes and also needs a high reverse bias voltage (30 V to 300 V) across it. In this regime the electron-hole pair is accelerated by the strong electric field and is capable of producing secondary charge carriers by impact ionisation like in the case of a photomultiplier tube. In other words this produces an avalanche of charge carriers thereby amplifying the photo current. Thus the avalanche photodiode can have gains as high as 10^4 . Gain is defined as the ratio of output current at an operating voltage to the current at zero bias voltage.

Two other properties of interest when selecting an avalanche photodiode for frequency domain spectroscopic applications are the responsivity and bandwidth. Responsivity is defined as the average output current divided by average optical power and has a unit of ampere per watt. The bandwidth is decided by the rise time of the photodiode, which is the time necessary to increase the detector output from 10% to 90% of its final value. The conditions that maximise the bandwidth and minimise the noise due to the avalanche multiplication process can be found in Emmons (1967). The investigations to enhance the frequency response of these detectors so that it could be used in new areas are still going on (Zaoui et al. 2009). The avalanche photo diode operated slightly above the breakdown threshold voltage is said to be operating in the Geiger mode (Pellion et al. 2006). An avalanche photodiode operating in Geiger mode can detect single photons, like the photomultiplier tube, and is sometimes referred to as a silicon photomultiplier (Renker 2006).

The “phase-amplitude crosstalk” is a limitation introduced to the phase measurement by both type of photodetectors, the photomultiplier tube and avalanche photodiode (Alford and Wickramasinghe 2000). This means the signal phase measured depends on the average light intensity entering the photo detector. Various experimental methods have been proposed to eliminate phase-amplitude crosstalk in photomultipliers as well as in avalanche photodiodes (Yokoyama et al. 1995; Morgan and Yong 2001). Yokoyama et al. proposed a scheme to eliminate the phase amplitude cross talk in distance measuring system based on phase change of a modulated source. In this method an appropriate optical bias (unmodulated) was superimposed on the modulated light so that the total intensity is kept constant.

The signal detected after interacting with the sample, in frequency domain spectroscopy, is in the radiofrequency (30 to 500 MHz) range. In order to

measure the amplitude and phase of this signal the frequency is down converted by heterodyne mixing method (Sevick-Muraca et al. 2003). The heterodyning refers to multiplying the signal in a mixer with a reference having a frequency slightly offset and filtering high frequency components out. The amplitude of low frequency component will be proportional to the signal amplitude and can be measured by standard lock-in techniques. This method has also been employed in the case of photomultiplier tube detectors by amplitude modulating the gain (Weng et al. 1991; Iwata et al. 2004). This method is usually employed because lock-in amplifiers are constrained to low frequency signals only; use of radiofrequency lock-in amplifiers may avoid the need to gain modulate the detector.

Figure 25 illustrates a heterodyne detection system reported by Fishkin et al. (1996). The output of the micro channel plate photomultiplier is separated into AC and DC components. The radiofrequency component is

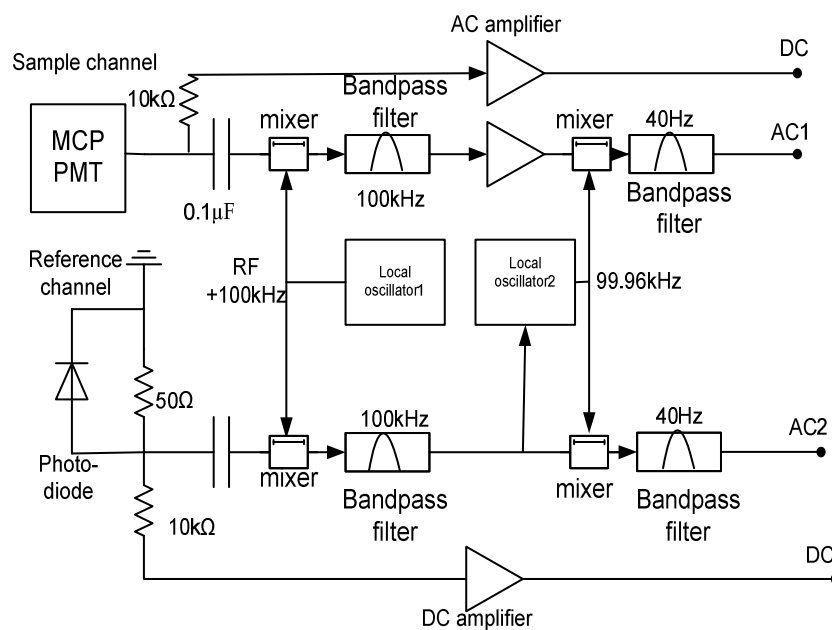


Figure 25 Block diagram of heterodyne detection system reported by Fishkin et al. (1996).

then mixed with a lower frequency of 100 kHz from the local oscillator. After filtering with a narrow bandpass filter, this is again mixed with a frequency of 99.96 kHz, a second bandpass filter is used to separate the difference frequency of 40 Hz. This 40 Hz signal preserves all the qualities of the radiofrequency output from the photomultiplier tube. The reference channel also works in the same way. The *AC* and *DC* signals were measured by a computer with help of a digital interface card.

3.5 Reported instrumentation

This section gives a brief overview of the light sources, intensity modulation techniques and detection system reported in the literature. Even though instrumental description of fluorometers and oximeters can be found in the literature, we would like start with the first instrumental setup which describes the propagation of photon density waves (Fishkin and Gratton 1993). Fishkin and Gratton used a fibre pigtailed diode laser emitting 810 nm as a source. The diode laser output was intensity modulated to radio frequencies by the amplified output of a signal generator. The laser diode output can be intensity modulated by controlling the drive current. The laser output was modulated at frequencies ranging from 20 to 120 MHz. The 1 m long 100 μm diameter fibre pigtail was immersed in a tank containing skim milk and India-ink mixture. They used another 3 mm diameter fibre bundle immersed in the tank to detect the photon density wave with photomultiplier tube. Both the source and detector fibre bundles were immersed with their faces down in an experiment to verify the validity of diffusion approximation. Fishkin and Gratton found the diffusion approximation to radiative transport equation fully described the propagation of photon in a homogeneous media for all absorption coefficients investigated. The range of absorption coefficients investigated was typical to some animal tissues in the near infrared.

Fishkin and Gratton used other source-detector configuration to verify other wave like properties of diffuse photon density waves. Fishkin and Gratton measured the phase shift, *DC* and *AC* amplitude by varying the source-detector separation over the range from 2.5 cm to 9.6 cm (in steps of 0.115 cm) keeping the modulation frequency constant. These quantities were measured by processing the photomultiplier output with an electronic cross-correlation system reported by Feddersen et al. (1989).

Tromberg et al. (1993) reported frequency domain instrumentation by modifying a flurometer. This setup employed an argon-ion or argon-ion pumped dye laser output modulated by a pockels cell. The pockels cell was driven by a function generator or the amplified output of a harmonic comb generator. Tromberg et al. used single frequency modulation as well as pulses with high harmonic content. Fused silica fibre of 600 μm diameter was used as source and detector fibres. Scattered light was detected by gain modulated photomultiplier tubes (Gratton and Limkeman 1983). The gain modulation was provided by harmonic comb generators with slightly offset frequency to the modulation frequency. Phase and amplitude response in the pulsed case were measured by transforming it to a frequency spectrum by an array processor. Single frequency modulation measurements were made by eliminating the harmonic comb generators and cross-correlation detection methods mentioned by Feddersen et al. Tromberg et al. calculated the absorption and scattering of Intralipid solution at various scatter concentrations by recording the phase and amplitude response at different modulation frequencies. Single frequency measurements were made by eliminating the harmonic comb generators and directly connecting the frequency synthesizers to the desired frequency. Absorption coefficient measurement made at various absorber concentrations in Intralipid was linearly interpolated and predicted absorption of pure Intralipid. Optical property measurements were made in Intralipid at 0.4%, 2% and 10% scatter

concentrations and demonstrated that the absorption coefficient measurements are not affected by scatter variations.

Frequency domain instrumentation has also been reported by employing an intensity modulated light emitting diode (Fantini et al. 1994a). The LED output (peak wavelength 665 nm) was modulated to 60 MHz using a function generator and immersed in the scattering medium simulating infinite medium geometry. One end of a 1 mm diameter plastic optical fibre placed in contact with the LED act as source fibre. The other is connected to a photomultiplier tube. Another photomultiplier tube detects the scattered signal inside the medium through a 3 mm diameter glass optical fibre. Here also the signal measurements were made with the electronic cross-correlation system mentioned earlier. All measurements were conducted in aqueous solution of Lyposin 20% with Methylene blue added as an absorber. The scattering coefficient of the solution was adjusted to match that of soft tissue. The absorption coefficient of Methylene blue dissolved in Lyposin at different concentrations were compared with absorption, of Methylene Blue dissolved in water, measured with a spectrophotometer. They got good agreement (within 10%) between the measurements. This report also studied the behaviour of the absorption and scattering coefficient at different absorber concentrations at a number of wavelengths. The reduced scattering coefficient was found to be unaffected by the absorber concentration.

A high band-bandwidth frequency domain instrument employing a network analyser was reported by Madsen et al. (1994). A network analyser is used to test electronic devices and networks by applying a known signal to the device and measuring the reflection and transmission characteristics. The network analyser output terminal gives a range of radio-frequencies, the device under test is usually connected between the input and output terminals to measure the transmission and reflection

characteristics. In the above instrumentation the source laser diode output was modulated by the radio-frequency signal generated by the network analyser (300 kHz to 1 GHz). Even though this setup employed a bias tee providing an offset to get sinusoidal modulation, the optical power output was limited due to the lack of impedance matching. This setup used 600 μm step index multimode fibre for the light delivery and collection. The signal detected by an avalanche photodiode was analysed by the network analyser interfaced to a computer. Measurements were made in a liquid tissue simulating phantom, at different absorber concentrations, by keeping the source and detector fibre separation fixed (14 mm) and by varying the modulation frequencies (50 MHz to 850 MHz). This instrumentation reported optical properties of liquid tissue simulating phantom at 670 nm within 10% of the expected values.

Pogue and Patterson (1994) reported frequency domain instrumentation using an intensity modulated laser diode as well as an arc lamp modulated with a pockel cell. In the first case a laser diode emitting 751 nm was directly modulated to 300 MHz by a signal generator. Fibre optic bundles of 3 mm diameter were used to deliver and collect the light from the sample. The detection setup employed gain modulated photomultiplier tubes, A/D converters and computer employing heterodyne method (Gratton and Limkeman 1983). In the second case an arc lamp was modulated at 130 MHz using a pockel cell, a monochromator was used to report absorption measurements in tissue phantom from 560-760 nm. This study analyses the situation where a tissue is mistakenly treated as semi-infinite medium. In this case the source detector separation will affect the value of the absorption coefficient estimated. The analysis found that a minimum tissue thickness of 20 mm is needed in the semi-infinite reflectance technique for source detector separation of the order of 10 mm. It was also found that for a specific absorption coefficient, decreasing reduced scattering coefficient will

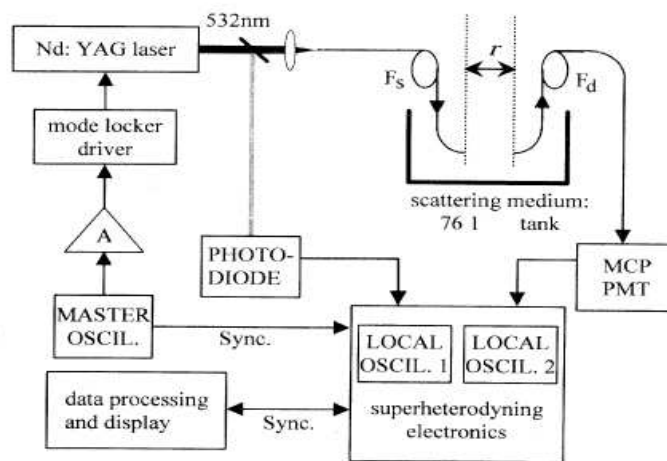


Figure 26 Frequency domain spectrophotometer reported by Fishkin et al. (1996) (reproduced).

increase the offset in absorption measured. This offset was found to be proportional to $(\mu_s')^{1/2}$.

Frequency domain spectrophotometer by Fishkin et al. (1996) indicated in Figure 26 uses a mode-locked pulsed laser at 532 nm with a repetition rate of 76.2 MHz. A Fourier analysis of this pulse train yields a series of harmonic intensity modulation frequencies with spacing of 76.2 MHz. This pulse train was coupled to a 0.15 cm diameter optical fibre using a lens and the other end of the fibre was immersed in a tank containing the scattering medium. A small portion of the pulse train was directed onto a fast photodiode, with a beam splitter, which provides a reference. A 0.3 cm glass fibre bundle used as detector fibre had a 0.1 cm aperture on the end immersed in the turbid medium. Inside the turbid media the fibre ends were directly facing each other.

The detector fibre was placed directly in front of 6 μm micro channel plate photomultiplier. The signal processing and measurements were made with an electronic superheterodyne detection system. Phase shift and demodulation measurements were made at fourteen intensity modulation frequencies (from 381 to 3200.4 MHz in steps of 76.2 MHz) at source-

detector separation ranging from 1.1 to 2.1 cm in steps of 0.1 cm. The modulation data acquired at 3200.4 MHz were inconsistent (the data was not linear with the source-detector separation) with both the P_1 approximation and standard diffusion equation.

This work (Fishkin et al. 1996) also indicated that the difference between standard diffusion equation and P_1 approximation is significant only at modulation frequencies of several megahertz or greater. At higher modulation frequencies and relatively small reduced scattering coefficient, P_1 approximation yields better results. For relatively large reduced scattering and/or low modulation frequencies, the standard diffusion equation is adequate for the description of light transport in turbid media.

Tromberg et al. (1997; Tromberg et al. 2000) reported a multi wavelength high bandwidth frequency domain instrument for non-invasively measuring the optical properties of human breast tissue. They used four laser diodes (674, 811, 849 and 956 nm) modulated by the output of a network analyser from 300 MHz to 1 GHz. The radiofrequency output of the network analyser was superimposed on the direct bias current of the diodes through individual bias tees. A portion of the modulated light was detected by a PIN diode and goes to one channel of the network analyser providing a real time compensation for the source fluctuations. An avalanche photodiode was used as the detector. Here they employed the semi infinite medium geometry where the source fibre (100 μm diameter gradient index) and the photodiode are in direct contact with the tissue surface. This instrument measured the frequency dependence of phase and amplitude of the photon density wave, at a source-detector separation of 2.2 cm, to estimate the absorption and reduced scattering coefficients of breast tissue. The wavelength dependence of absorption was used to estimate the tissue haemoglobin concentration, oxygen saturation and water content. Results of this study showed that frequency domain

measurements are sensitive to absorption and scattering changes induced by the presence of small palpable lesions in breast tissue.

Frequency domain instrumentation has also been used for particle size analysis (Jiang et al. 1997). This set up used a pulsed laser with a repetition rate of 80 MHz. The pulse repetition rate was changed to 4 MHz by passing the light through an acousto optic modulator. Photomultiplier tubes were used to detect the light from scattering medium and reference through optical fibres. Fourier analysis of the 4 MHz pulse train detected from the scattering medium yielded a series of intensity modulation frequencies at multiples of 4 MHz. Heterodyning techniques were accomplished, with gain modulated photomultipliers, for signal processing and measurements. Measurements were made in polystyrene micro-sphere suspensions and the results were in agreement within 10% of the dynamic light scattering size distribution measurements.

A broad bandwidth frequency domain instrument using multiple wavelengths was reported by Pham et al. (2000). The instrument used four laser diodes with output modulated by the radio frequency signal from a network analyser. This setup used a fraction of the network analyser output redirected to the reference channel served as a reference signal for the measurements. Modulation frequencies up to 1 GHz were used. Light from individual laser diodes were coupled to optical fibres with their output end connected to an optical switch. This ensures that only one laser diode was modulated at a time. Optical fibres with 100 μm diameter were used to couple light into the sample. Diffusively reflected light from the sample was collected by a 1 mm diameter fibre connected to an avalanche photo diode. Radio frequency signals from the avalanche photodiode were directed to the network analyser to be heterodyned to make phase and amplitude measurements relative to reference channel. The detected signal levels were typically between -10 and -40 dBm. Pham et al. reported

phase and amplitude accuracies of the order of $\pm 0.3^\circ$ and $\pm 3.5\%$ respectively. The phase and amplitude precision observed was an order of magnitude higher compared to the accuracy. The accuracy figures were used to report uncertainties in frequency domain measurements.

Pham et al. performed optical property measurement in tissue phantoms (Intralipid) in infinite and semi-infinite geometries. The accuracy for quantifying the absorption coefficient was found to be $\pm 5\%$ for semi-infinite and $\pm 4\%$ for the infinite geometries respectively. For the reduced scattering these figures were ± 2 and $\pm 3\%$ respectively for the infinite and semi infinite geometries. The reduced scattering coefficient measured was 3% lower than expected at all wavelengths; this was attributed to variation in preparation of Intralipid. This work demonstrated the capability of frequency domain methods to separate the contribution of absorption from scattering in infinite and semi-infinite geometries. This was accomplished by making absorption measurements at various scatter concentration and vice versa.

The absorption and reduced scattering coefficients of tissue simulating phantoms were recovered with 10% and slightly above 10% respectively using frequency domain instrumentation by Xu and Patterson (2006). This setup used an intensity modulated (100 MHz) laser diode (750 nm) as source. The detection system employed a gain modulated photomultiplier and lockin amplifier for the measurement of phase shift and amplitude attenuation. The setup also employed two detector fibres; only one fibre was translated to make measurements. The setup was tested for phase amplitude crosstalk. The phase amplitude cross talk was thought to be a property of the detector alone. This work found the cross talk ($\sim 2.5^\circ$) is dependent on the geometry of light path and the method by which light is attenuated.

The frequency domain instruments that are commercially available use the multi distance approach that is measurements are collected at different source-detector separations at constant modulation frequency. Transformation of a multi distance frequency domain instrument available in the market to multi frequency instrument, so that it can be used in the case of small tissues, is reported by Spichtig et al. (2009). The instrumentation was validated by making measurement in silicone and Intralipid phantoms with known optical properties. Also *in vivo* measurements were made in human forearm and cervix tissues. Eight

Table 3 Summary of frequency domain instrumentation [PMT-photomultiplier, PD-photodiode, CCD-charge coupled device, LD-laser diode, MCP-micro channel plate, APD-avalanche photodiode]

Work	Source	detector	Modulation method	Medium	Results
Fishkin and Gratton (1993)	LD	PMT	current	skim milk India-ink mixture	Validated diffusion approximation in homogeneous media for range of μ_a
Tromberg et al. (1993)	argon-ion or argon-ion pumped dye laser	PMT	pockel cell	Intralipid	μ_a measurements not affected by μ_s 's variations
Duncan et al. (1993)	four laser diodes	PMT	current	Intralipid	
Fantini et al. (1994)	LED	PMT	current	Lyposin 20% with Methylene blue	μ_s unaffected by the μ_a
Madsen et al. (1994)	LD	APD	current	Intralipid	optical properties within 10% of the expected values
Pogue and Patterson (1994)	LD and arc lamp	PMT	current pockel cell	Intralipid	minimum tissue thickness of 20 mm for semi-infinite reflectance at source detector separation 10 mm
Fishkin et al. (1996)	mode-locked pulsed laser	MCP, PD		Intralipid	difference between SDE and P1 approximation is significant only at ω several MHz or greater
Tromberg et al. (1997)	LD	APD	current	breast tissue	FD sensitive to μ_a and μ_s 's changes in breast tissue
Pham et al. (2000)	LD	APD	current	Intralipid	Accuracy $\mu_a \pm 5\%$ (semi-infinite) and $\pm 4\%$ (infinite medium) $\mu_s \pm 2\%$ (semi infinite) and $\pm 3\%$ (infinite)
Xu and Patterson (2006)	LD	PMT	current	Intralipid	μ_a & μ_s recovered with 10% and slightly above 10% respectively
Spichtig et al. (2009)	LD	APD	current	Intralipid	μ_a & μ_s accuracy of < 10% and 31% respectively

laser diodes (690, 692, 764, 805, 872, 888, 914 and 980 nm) were used to make measurements and the modulation frequencies were in the range from 130 to 400 MHz in steps of 10 MHz. This setup used the photomultiplier and avalanche photo diode for measurements of optical properties thus providing a comparison between the two.

Even though the avalanche photodiode and photomultiplier tube had approximately the same accuracy the APD enables detection at wavelengths above 880 nm. The absorption and reduced scattering coefficients of phantoms were determined with an accuracy of less than 10% and 31% respectively. The measurement in forearm and cervix tissue enables water and haemoglobin to be quantified.

3.6 Combination of instrumentations

There are also a few reports of instrumentation that uses the combination of different measurement techniques. The combination of frequency domain and steady state instrumentation was reported to measure the optical properties of turbid media (Bevilacqua et al. 2000). The steady state instrumentation employed a 150 W halogen lamp as source. A fibre coupled spectrograph with CCD detectors analysed the light diffusively reflected from the sample over a wide wavelength range (650 nm – 1000 nm). Light was delivered to the sample with four fibre bundles each with diameter of 600 μm , collected with 1 mm diameter fibre. The frequency domain setup used seven different amplitude modulated laser diodes (672, 800, 806, 852, 896, and 978 nm) with output powers of less than 20 mW at the sample. The modulation frequencies were provided by a Network Analyser and the light was detected by avalanche photodiodes modules.

In vivo measurements were made in a tissue simulating phantom and female breast. The strength and weakness of both steady state as well as

frequency domain measurements were also highlighted. The steady state technique enabled better detection of absorption features because of the continuous wavelength coverage compared to the discrete wavelength frequency domain measurements. The frequency domain technique with large source detector separation can probe depths that cannot be achieved by spatially resolved steady state technique. As frequency domain measurements were made only at discrete wavelength constrained by the availability of laser diodes combining this with the steady state technique improved the accuracy of measurement results.

Swartling et al. (2003) reported measurements comparing spatial and temporal diffuse reflectance. They used the same setup (Dam et al. 2001) described in the continuous wave instrument section. The time domain instrumentation used picoseconds pulsed diode lasers at 660 nm and 785 nm as source. A 50 μm diameter gradient index fibre delivered light to the sample and another fibre with 600 μm was used to collect light and delivered to a micro channel plate photomultiplier. The time dispersion curve for the pulses was recorded with time-correlated single photon counting measurements. The measurements made on solid tissue phantoms indicated less than 10% difference in the reduced scattering values between the systems. For the absorption coefficient this corresponds to an absolute difference of less than 0.05 cm^{-1} for absorption values in the range 0.05 to 0.3 cm^{-1} . *In vivo* measurements performed in a meat sample indicate that time resolved method provides robust results in presence of heterogeneities.

The review of literature concerning continuous wave, time domain and frequency domain instrumentation suggests optical properties of a turbid medium can be extracted with accuracy in the range 1 to 10%. This accuracy seems to be the same irrespective of the instrumentation method. Each method has its own merits and demerits. In any case an upper limit

of the accuracy seems to be 10% and is regarded as sufficient as many applications do not require the absolute quantification of optical properties.

3.7 Summary

An overview of various space resolved, time domain and frequency domain instrumentation reported in the literature is presented. The merits and demerits of each of this measurement technique are also discussed. In the literature there seems to be a belief that extraction of the optical properties can be much improved in accuracy, compared to intensity measurements only, and as time resolved method uses an additional parameter to estimate the optical properties. Also the frequency domain instrumentation is cheaper to fabricate compared to time domain instrumentation. None of this instrumentation can be considered superior to the other in spectroscopic estimation of optical properties. However, by employing a range of measurement techniques we can gain confidence in experimental results. The frequency domain technique separates the effect of scatter from the measured absorption coefficient and vice versa. This will be an advantage when we intend to monitor the minute changes in the absorption coefficient of turbid media with temperature.

The frequency domain spectrometer setup is illustrated in Figure 27. The light source is a titanium-sapphire laser which is tuneable from 700 to 1050 nm. The output wavelength is monitored by diverting a small fraction (4%) of the output light using a glass plate. This light is coupled into a multimode optical fibre (63 μm diameter) and delivered to a wavemeter (1150, Burleigh, USA) to monitor the wavelength of operation. The laser output is intensity modulated to 50 MHz using an acousto-optic modulator (GPM 800-200-950, Brimrose, USA) driven by a fixed frequency (800 MHz) driver (FFA-800-B1-F1, Brimrose, USA).

The intensity modulation is supplied by a high-frequency signal generator (SMY-02, Rohde & Schwartz, Germany). The fixed frequency driver for the acousto-optic modulator accepts a modulation input in the range 0 to 1 V. The modulation input supplied by the signal generator needs an offset voltage to satisfy this condition. This offset voltage is added to the modulation input with the help of bias tee (ZX85-12G-S+, Mini-Circuits, USA). The laser output is focused into the acousto-optic crystal using a lens with a 10 cm focal length and near-infrared antireflection coating.

The acousto-optic modulator requires linear horizontal optical polarisation for efficient operation. The titanium-sapphire laser output is linearly polarised in the vertical direction. As it is expensive to use wave plates to rotate the polarisation of laser beam, the acousto-optic crystal is mounted sideways as shown in Figure 28. This figure also shows the focusing lens and the arrangement to couple the modulated output beam into the source optical fibre (BFL 48-1000, Thorlabs, USA) with the help of a microscope objective lens (20X).

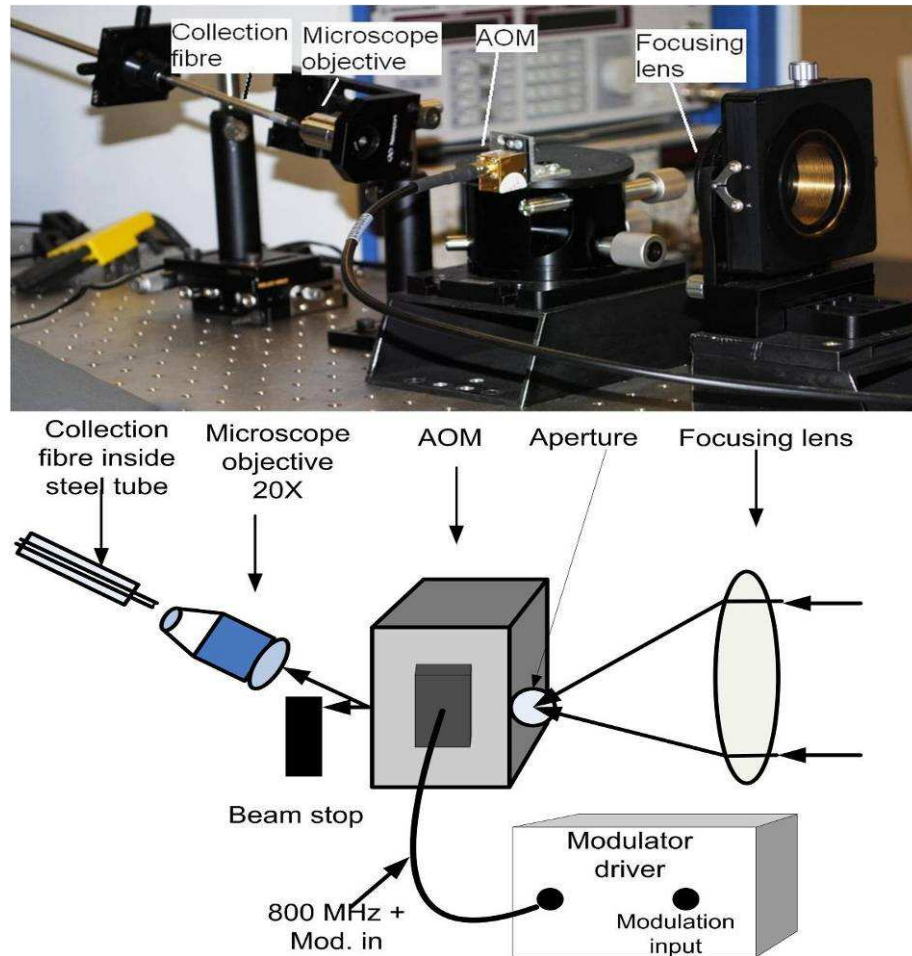


Figure 28 Photograph and schematic diagram of the acousto-optic modulator used in the experiment setup with focusing lens and fibre coupling mechanism.

This arrangement couples only the first order modulated beam into the fibre and blocks the unmodulated zeroth order beam. The source fibre delivers the modulated light into the sample (Intralipid®20%). The 1 mm diameter low-OH glass fibre with a numerical aperture of 0.48 is threaded through a 6 mm diameter stainless steel tube to provide rigidity. A second identical fibre collects the light from the sample delivering it to the avalanche photodiode module (C5331-30, Hamamatsu, Japan) for measurement. The source and collection fibres are mounted on a translation stage as shown in Figure 27. The translation stage is interfaced to a computer through a serial cable and is controlled by a custom Labview (National Instruments, USA) program. The distance between the source and collection fibres is controlled by the computer to a precision

better than 10 μm . The closest position possible between the fibres is 10 mm.

The amplitude and phase shift of the transmitted signal is measured by a lock-in amplifier (SR844, Stanford Research Systems, USA). The phase reference for the lock-in amplifier is provided by splitting the source modulation from the signal generator. The lock-in amplifier was interfaced to the computer through a USB to GPIB control module (488-USB2 GPIB, ICS Electronics, USA) and controlled by custom software implemented in LabView. The whole setup was automated with custom MATLAB (The MathWorks, USA) and LabView programs for automated data collection and analysis. The MATLAB and LabView source code is given in APPENDIX II. A detailed description of each component used in the construction of spectrometer is outlined in the next sections.

4.3 Light source

The light source used in our setup is a diode pumped continuous wave titanium-sapphire laser (Verdi-V5 and 899-LC combination, Coherent, USA), which is tuneable from 700 to 1100 nm. The Verdi-V5 consists of a diode- pumped, frequency-doubled (Franken et al. 1961) Nd:YVO₄ laser that provides green (532 nm) output with a continuous wave power of

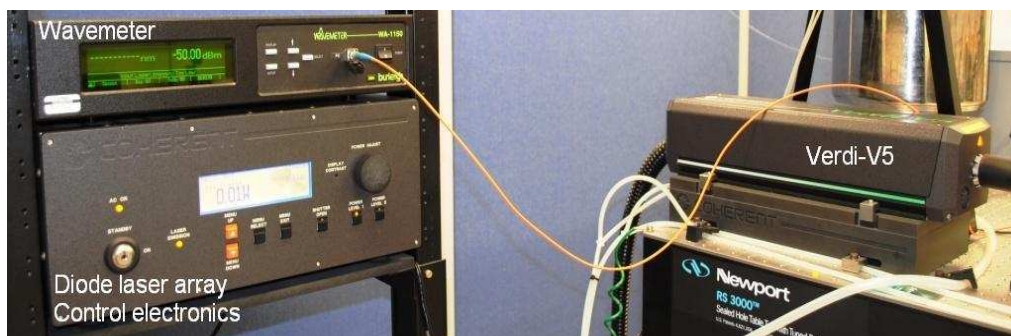


Figure 29 Laser system Coherent Verdi-V5 with biasing electronics for the diode array (Verdi-V5).

5 W. The laser diodes are integrated in a fibre array package with a thermo-electric cooler in the power supply and CPU box as shown in Figure 29. The diode laser output, used to pump the Nd:YVO₄ laser, and is delivered through optical fibres (inside the black plastic tubing) as shown in Figure 29.

A schematic diagram of the Nd:YVO₄ laser optics is shown in Figure 30. The lasing medium is an Nd:YVO₄ crystal with pump power provided by the diode lasers through the fibre delivery. The optical diode, based on the Faraday effect, allows light transmission in only one direction ensuring unidirectional lasing operation. The temperature of the lasing crystal and the etalon are controlled by thermo-electric coolers.

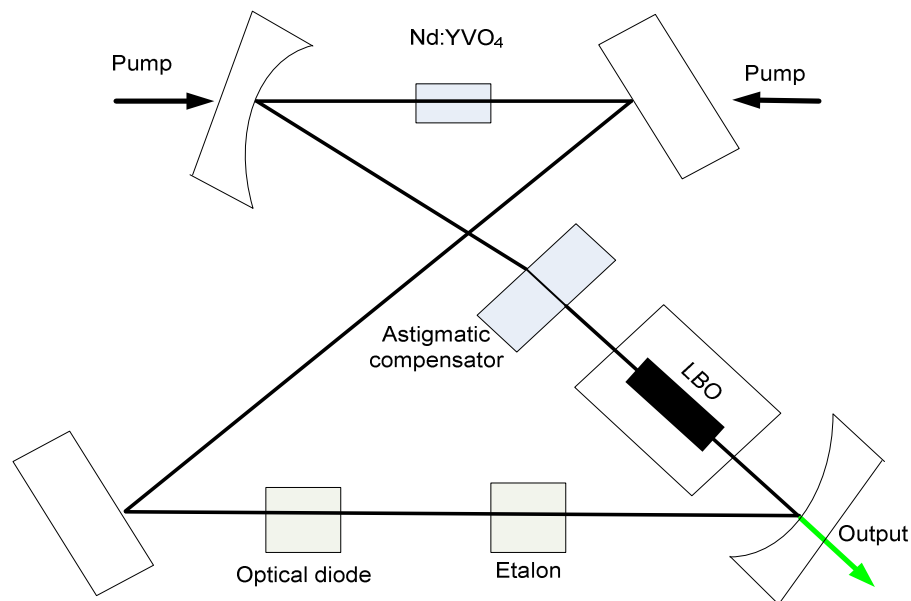


Figure 30 Laser head optical schematic of Nd:YVO₄.

The non-critically phase matched Lithium borate (LBO) crystal held at approximately 148°C ensures generation of the second harmonic. The etalon helps single frequency operation at 532 nm. The green output has a beam diameter of 2.25 ± 0.225 mm and power stability of ± 50 mW. This output at 532 nm is used to pump the tuneable titanium-sapphire laser.

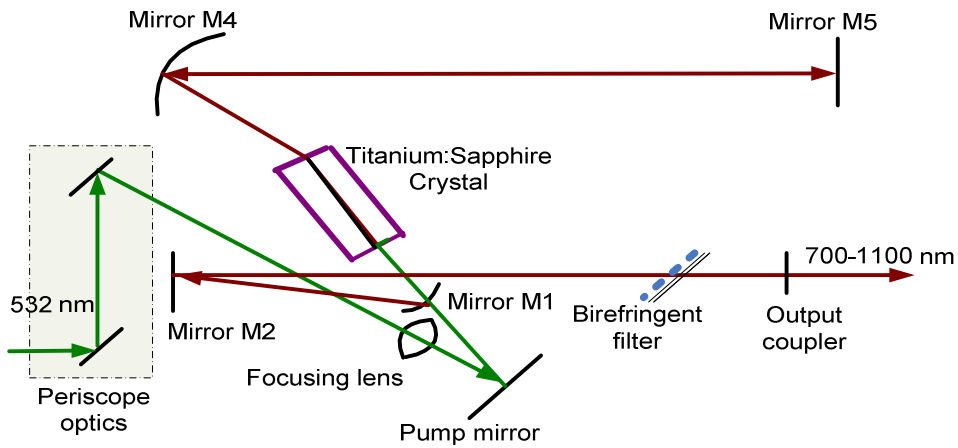


Figure 31 Schematics of titanium sapphire laser cavity.

The optical schematic diagram for the folded linear cavity titanium-sapphire laser is shown in Figure 31. The green laser output from the Nd:YVO₄ laser is delivered to the titanium-sapphire crystal through a periscope arrangement with two plain mirrors. It is then focused and

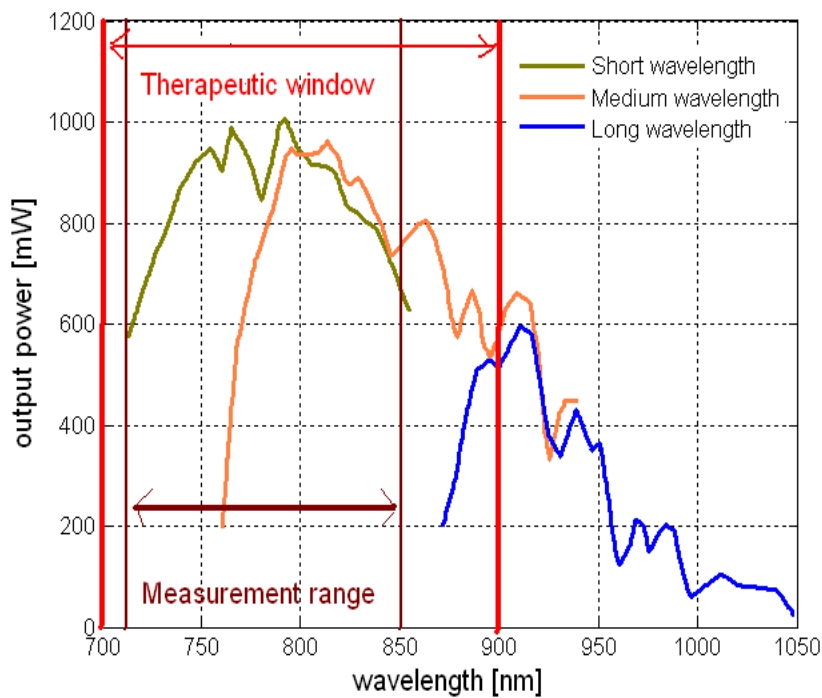


Figure 32 The output power variation of titanium-sapphire laser plotted against wavelength (Palmer 2003).

delivered to the Ti:sapphire crystal by the pump mirror. A three plate birefringent filter (Zhu 1990) mounted at its Brewster angle allows 2 GHz broadband operation. All components are mounted on a 2-inch invar bar to provide mechanical strength and stabilize the cavity length against temperature changes. There are different sets of output couplers to get wavelength coverage from 700-1100 nm. The output power can vary from 100 mW to 1 W depending on the selected wavelength.

The titanium-sapphire laser output has a tuning range of 710 to 1050 nm, a maximum power of 1 W at 790 nm, a beam diameter of 0.6 mm at the output coupler and is vertically linearly polarized. Figure 32 illustrates the output power at various wavelengths with different output couplers. The output power is strongly dependent on the optical alignment. In this thesis we have made use of the short wavelength optics and made measurements from 710 to 850 nm as this range stays well within the therapeutic window.

4.4 Acousto-optic modulator

The most important specification for applications like frequency domain spectroscopy is the modulation bandwidth of the acousto-optic modulator. This is the maximum frequency at which the light beam can be modulated. The acousto-optic modulator used here has a digital modulation bandwidth of 200 MHz and an analogue bandwidth of 135 MHz.

An acousto-optic modulator (GPM-800-200-950, Brimrose, USA) made from Gallium phosphide is used in our experimental setup. This section describes application-specific considerations for selecting an acousto-optic modulator along with the characteristics of this particular device.

Gallium phosphide has been found to provide excellent diffraction efficiency (Bonney et al. 1984). The diffraction efficiency is defined as the ratio of deflected optical power to unreflected optical power, divided by the radiofrequency power supplied by the transducer (Bonney et al. 1984). The optical power requirement for an application is determined by this efficiency. The optical transmission of the substrate material at the operating wavelength also affects the output power. The acousto-optic modulator used in this setup has an optical transmission of more than 80% and efficiency greater than 35% in the wavelength range 710 to 950 nm.

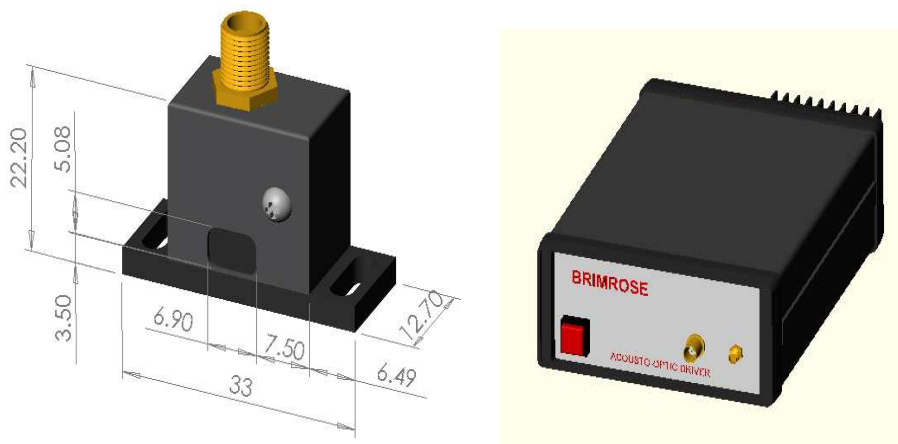


Figure 33 Acousto optic modulator and the fixed frequency driver (reproduced from Brimrose, USA, product catalogue).

For a particular light wavelength and orientation of the Bragg cell there is a given radiofrequency that matches the Bragg condition. This frequency is referred to as the centre frequency. The acousto-optic modulator used in our setup has a centre frequency of 800 MHz. In reality there will be a range of frequency, close to the centre frequency, which will be close enough to give Bragg diffraction. This frequency range is referred to as the RF bandwidth, and is 400 MHz for the AOM used here. The maximum modulation frequency will be around 25% of the centre frequency.

The acousto-optic modulator has a Bragg angle of 3.5° and separation angle of 7° between the first and zeroth order beams. These parameters can impose physical limitations when coupling diffracted light into an optical fibre. Figure 33 shows the acousto-optic modulator with the fixed frequency driver (FFA-800-B1-F1, Brimrose, USA). The driver circuit consists of a quartz crystal referenced phase-locked loop, giving a radiofrequency signal at 800 MHz and 1 W output power.

4.5 Avalanche photodiode module and detection electronics

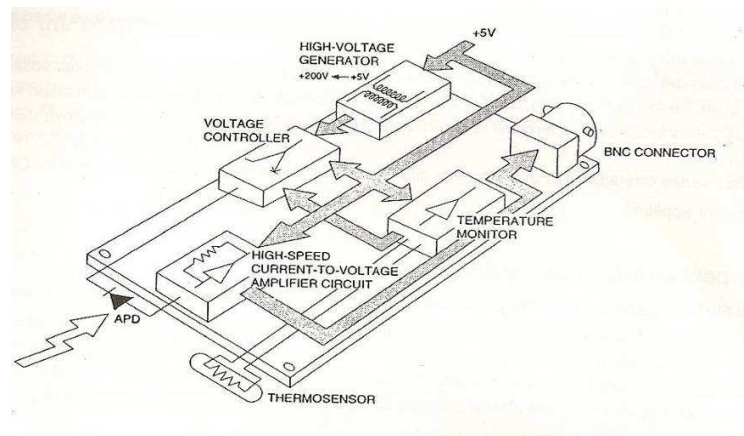


Figure 34 Block diagram of avalanche photodiode module (reproduced from APD MODULE C5331, Instruction Manual, Hamamatsu Photonics K.K.).

Avalanche photodiodes are available as modules that incorporate amplifiers and other circuit components integrated in to a package. The experimental setup described in this thesis uses such an avalanche photodiode module (C5331-01, Hamamatsu, Japan). The internal block diagram is shown in Figure 34. This module integrates a silicon avalanche photodiode, a high voltage generator, voltage controller, temperature monitor and a high-speed current to voltage amplifier into a small printed circuit board. The avalanche photodiode is provided with a fibre coupling connector that has an integrated lens.

This avalanche photodiode module was selected as it has good sensitivity and high gain from 400 to 1000 nm and a cut-off frequency of 100 MHz,

significantly higher than our modulation frequency. The avalanche photodiode includes a high-speed current to voltage converter giving an output of around 46 mV for an incident optical power of 1 μ W. This output corresponds to a minimum avalanche photodiode gain of 30; the avalanche photodiode gain is variable (maximum 200), making it ideal for low light level applications. The module incorporates a temperature compensating bias circuit that stabilizes the gain if the sensor temperature varies. The modules power supply requirements (5 V DC) also makes the avalanche photodiode easier to use than a photomultiplier tube which needs a 700 - 1 kV supply. The output signal voltage is available through a 50 ohm BNC connector.

The instrumentation described in this thesis employs a radiofrequency lock-in amplifier (SR844, Stanford Research Systems, USA), which accepts input signals with frequency ranging from 25 kHz to 200 MHz. Lock-in amplifiers are used to detect and measure very small AC signals using a technique known as phase sensitive detection (Scofield 1994).

4.6 Performance testing

This section discusses performance evaluation of the instrument developed. The effects of phase-amplitude crosstalk, accuracy and repeatability are examined. These properties are important for reliable measurements of optical properties.

4.6.1 Phase and amplitude variation after acousto-optic modulator

These measurements were motivated by the discrepancies in phase measurements observed with a photomultiplier tube (R928, Hamamatsu photonics, Japan) detector instead of the avalanche photodiode module (C5331-01, Hamamatsu Photonics, Japan). The phase lag of the photon density wave measured in a 1.8% Intralipid[®] solution was found to be two orders of magnitude higher than what was expected from theory. We

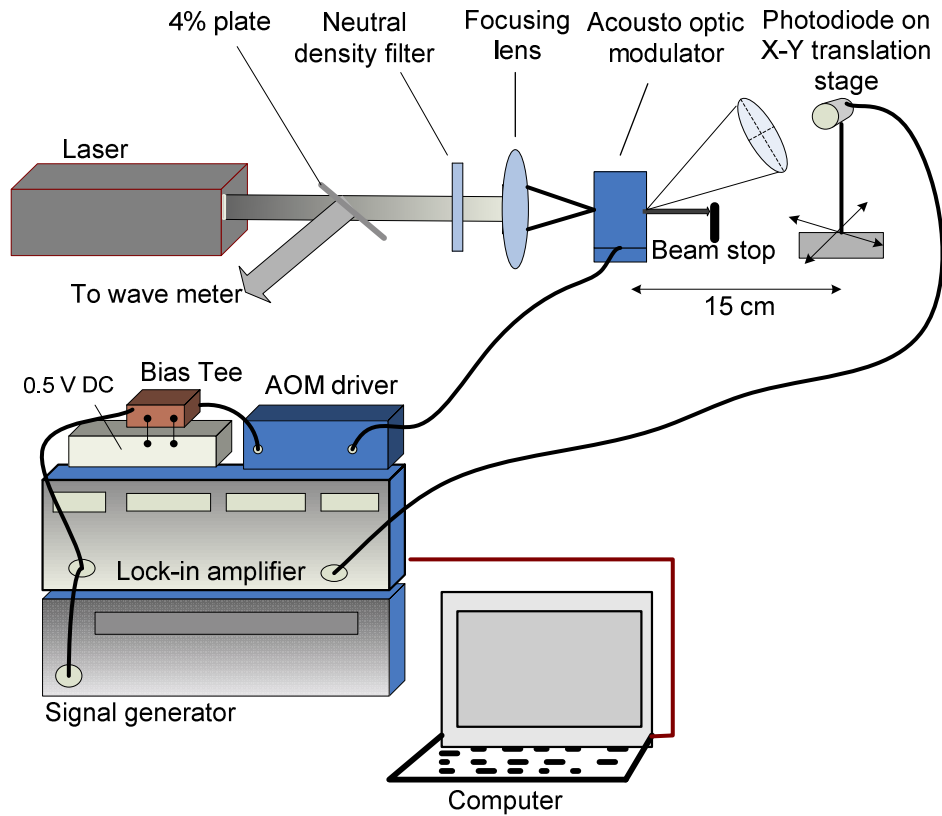


Figure 35 Experiment setup to monitor phase variation across the modulated beam.

suspected this phase variation had origins in the acousto-optic modulation.

Figure 35 shows the setup to monitor the phase and amplitude variation across the laser beam modulated at a frequency of 50 MHz. A small area photodiode (DET 210, Thorlabs, USA) mounted on an X-Y micrometer stage and scanned across the beam. This photodiode output is connected to the lock-in amplifier as shown in the diagram.

Figure 36 illustrates the phase and amplitude measured across the modulated beam at a distance of 15 cm from the exit of the acousto-optic modulator. The phase and amplitudes were measured by the lock-in amplifier.

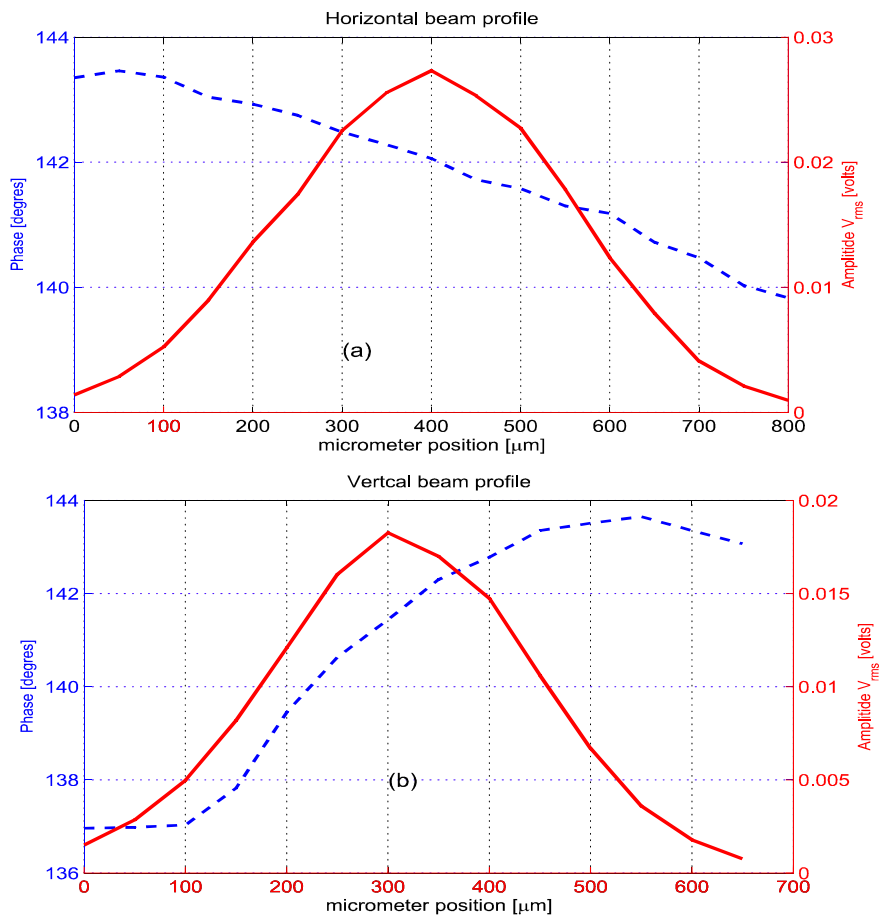


Figure 36 Variation of intensity and phase of the modulated beam measured at a distance of 15 cm from the output aperture of the acousto-optic modulator.

Figure 36 shows a variation in phase of approximately 2° horizontally and about 4° vertically across the beam. This phase variation may be caused by the glass window in front of the photodiode or may be a result of the acousto-optic modulator. This spatial phase variation is important while considering other effects like phase–amplitude crosstalk. The combination of these phase errors can introduce large uncertainties in the optical property measurements. We believe, in our case, the phase variation is introduced by the glass window in front of the photodiode and consequently does not affect our measurements.

4.6.2 Detected signal

Figure 37 illustrates the frequency spectrum of the signal detected by the APD module from a turbid sample, analysed with a spectrum analyser

(R3131, Advantest Corporation, Japan). Figure 37 (a) and (b) illustrates the signal detected at the initial (10 mm) and final (30 mm) optode separations.

This separation is typical for the range covered in this thesis. These phase and amplitude data were used to calculate the optical properties using equations 41 and 42 from section 2.9. Figure 37 (a) and (b) corresponds to a source (wavelength 800 nm) modulation frequency of 50 MHz.

Figure 37 (a) indicates a signal amplitude of -30.25 dBm and an intrinsic

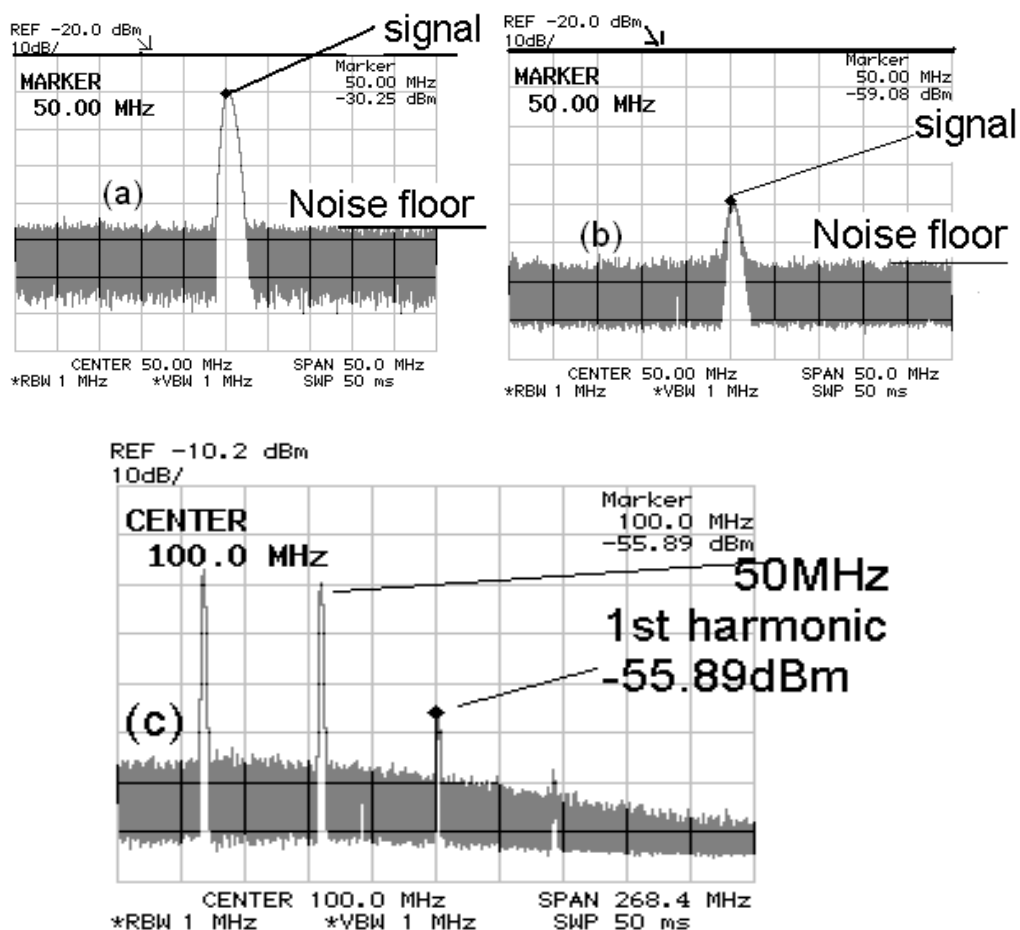


Figure 37 Frequency spectrum of detected signal at two optode separations (a) 10 mm, (b) 30 mm and (c) indicates the first harmonic. This corresponds to a typical scan of the optode from 10 to 30 mm at a source modulation frequency of 50 MHz.

noise of approximately -68 dBm. This results in a signal-to-noise ratio of about 100. In Figure 37 (b) the signal amplitude reduces to -59 dBm and the intrinsic noise floor shifts to -75 dBm, so again the signal-to-noise ratio is close to 100.

The reduction of the noise floor as the signal decreases is a property of the photodiode module and is explained in the manual (APD MODULE, C5331, Instruction manual, Hamamatsu Photonics). The first harmonic at 100 MHz is indicated in Figure 37 (c) and has amplitude of -56 dBm; this is recorded at a source detector separation of 10 mm where the signal amplitude is -30 dBm. The amplitude of all the higher harmonics was less than -75 dBm. The low signal to noise ratio can adversely affect on the robustness of optical property measurements, even with very low harmonic content.

4.6.3 Phase and amplitude measurements

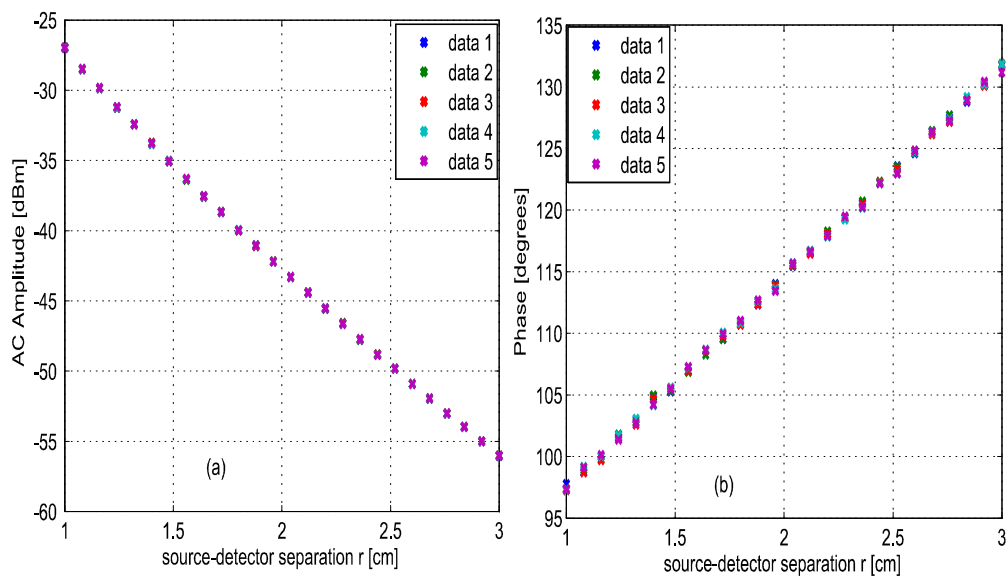


Figure 38 AC amplitude (a) and phase (b) of photon density wave measured by the lock-in amplifier plotted against source-detector separation.

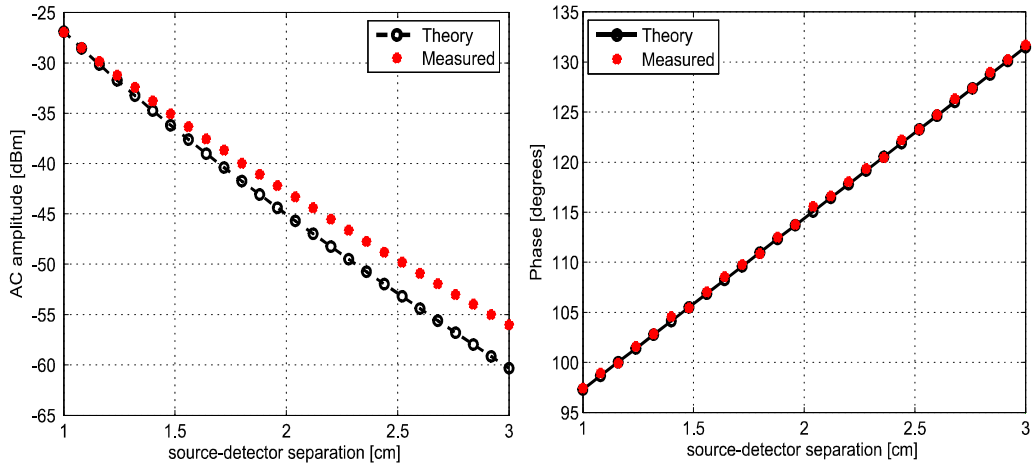


Figure 39 Amplitude and phase variation measured and predicted by theory. Simulated based on equations 27 and 28 for a medium with absorption 0.024 cm^{-1} and reduced scattering 16 cm^{-1} at a source modulation frequency of 50 MHz.

Figure 38 (a) and (b) shows the phase and AC amplitude measured by the lock-in amplifier in a solution of 1.8% Intralipid at 790 nm. The expected absorption and reduced scattering coefficients at this concentration and wavelength are approximately 0.024 cm^{-1} and 16 cm^{-1} respectively. The source modulation frequency is 50 MHz. The measurements are recorded

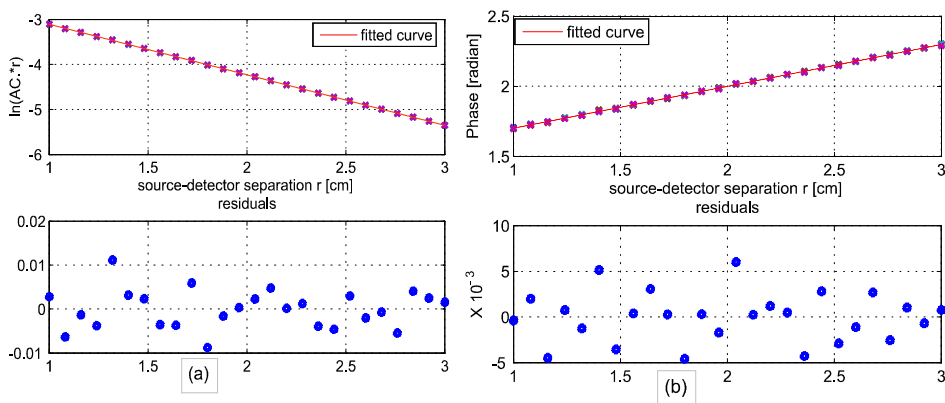


Figure 40 (a) Logarithm of AC amplitude multiplied by source detector separation plotted against source detector separation. (b) Phase in radian plotted against source detector separation. The subplot shows the residuals for a linear regression to the amplitude and phase data.

by moving the detector fibre from 10 mm to 30 mm in steps of 0.8 mm. At each step, five replicate measurements of phase and amplitude were recorded. The change in amplitude and phase is nearly -30 dBm and about 32°, respectively.

Figure 39 shows the amplitude and phase variation expected from these experimental measurements based on equations 27 and 28. An arbitrary source power of 1 mW is assumed. The model shows a 13% difference in amplitude and 1% difference in phase compared to the experimental values. This difference seems to be higher than expected from the signal-to-noise ratio found in section 4.6.2.

In Figure 40 (a) the AC amplitude is multiplied by the source detector separation and the logarithm of this quantity is plotted against source detector separation. The measured phase is converted to radian and is plotted against source detector separation as shown in Figure 40 (b). From the slope of a linear fit to the data in Figure 40, the absorption and reduced scattering coefficients of the medium are calculated using equations 41 and 42. The residuals from the linear regression (Figure 40, lower plots) show no obvious trend or pattern indicating a linear fit is appropriate.

4.6.4 Phase-amplitude crosstalk

Phase-amplitude crosstalk is a property of the detector that introduces error in phase measurements. In photodetectors, in particular photomultipliers, the transit time of charge carriers (electrons) through the device depends on the number of charges present at any particular time. When light intensity changes the transit time changes, which affects the phase of an AC signal. This phase delay can affect the optical property measurements and, if significant, a correction factor must be applied.

The phase-amplitude crosstalk in our instrumentation was measured by introducing a variable neutral density filter (NDC 50C-4M, Thorlabs, USA) between the acousto-optic modulator and the microscope objective as shown in Figure 41. The source-detector separation was kept constant. The power was attenuated by rotating the neutral density filter in steps each time recording the phase and amplitude by the lock-in amplifier. In the absence of significant cross-talk between phase and amplitude, the phase measured should remain constant reflecting a fixed shift in phase between the source-and detector.

The phase measurements were recorded for three fixed source detector positions, 10, 20 and 30 mm. The neutral density filter is rotated in such a way that the amplitude attenuation recorded by the lock-in amplifier is in the range of a single scan for optical property measurement in a turbid

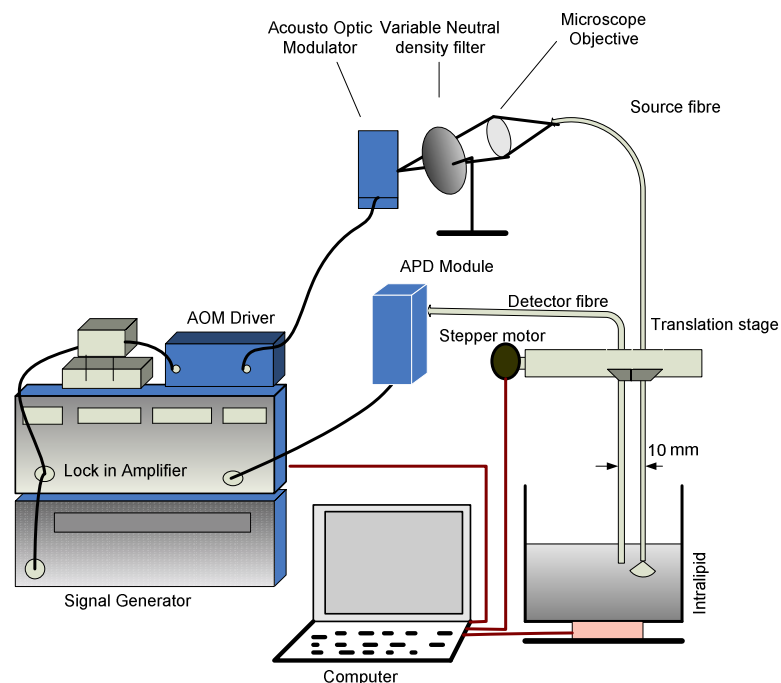


Figure 41 Experiment setup to measure phase amplitude crosstalk. The variable neutral density filter was rotated to make phase and amplitude measurements from the sample keeping the source and detector fixed.

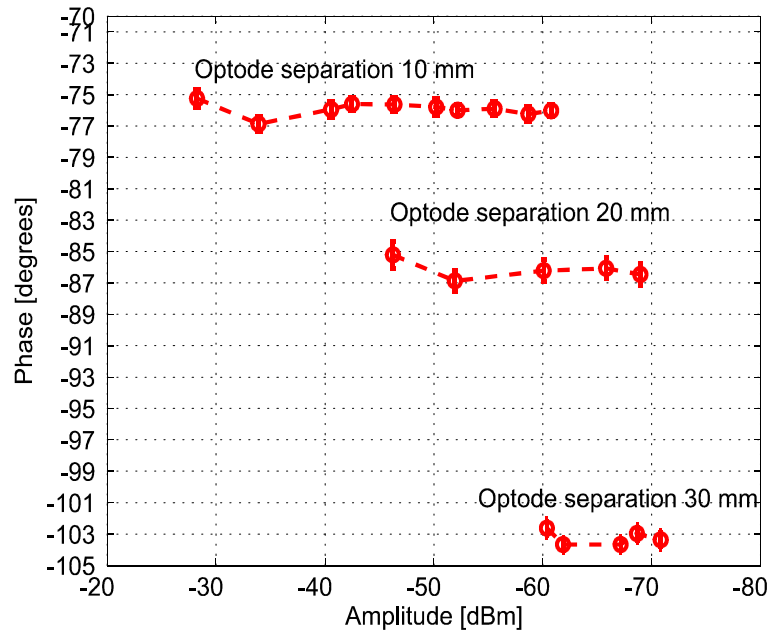


Figure 42 Phase plotted against amplitude attenuation at three source detector separations. The laser power is attenuated by rotating the neutral density filter at fixed source detector separation. The error bars represent ± 1 standard deviation.

medium (from -30 to -60 dBm). At each position of the neutral density filter, ten phase and amplitude measurements were recorded.

Figure 42 illustrates the mean phase measured by the lock-in amplifier plotted against amplitude attenuation introduced by the neutral density filter at three source detector separations. The standard deviation of the ten measurements was calculated and is indicated using error bars in Figure 42.

All three plots show a consistent decrease in phase for the first intensity change. Subsequent changes to the source intensity do not affect the phase. Phase amplitude crosstalk is characterised by a consistent increase or decrease of measured phase with change in intensity. We conclude that the phase variation with intensity illustrated in Figure 42 is not caused by phase amplitude crosstalk. As phase-amplitude crosstalk depends on the method of light attenuation (Xu and Patterson 2006) the drop at the second

measurement point is due to the amplification of stray light reflections, at the expense of signal, from the filter surface. This is caused by physically handling the filter (Baltes and Faris 2009). As illustrated in Figure 42 this is more prominent when the signal strength is higher. Thus we conclude that our measurements are not affected by phase amplitude crosstalk.

4.6.5 Accuracy and precision

Accuracy and precision of the instrumentation both depend on the stability of amplitude and phase measurements, which, in turn depend on source stability. First the amplitude and phase stability of the instrumentation were investigated. Measurements were made in air with the source and detector fibre facing each other 10 cm apart. The source was modulated at 50 MHz and a lock-in amplifier used to acquire phase and amplitude data for ten minutes.

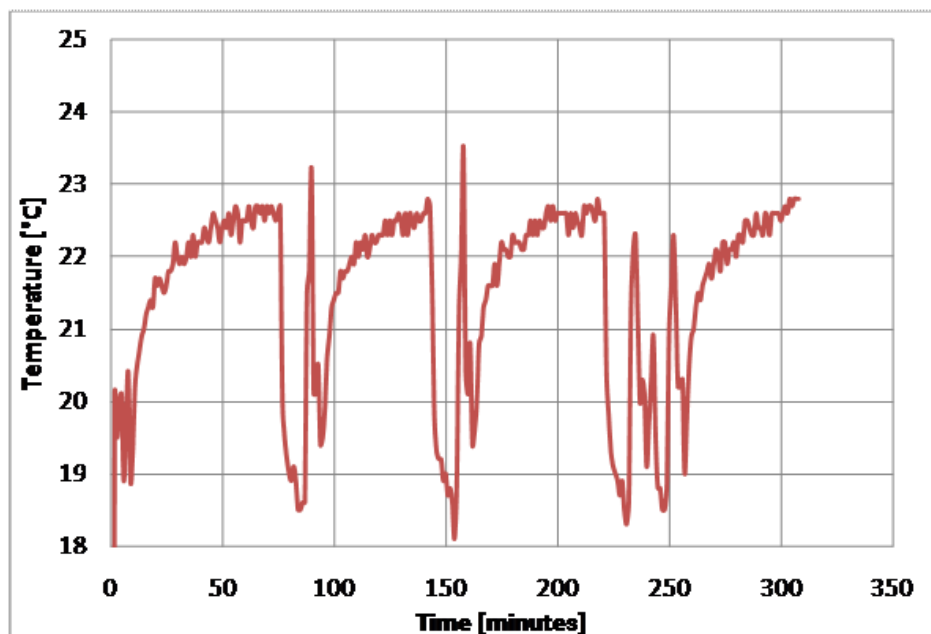


Figure 43 Room temperature variation inside the lab monitored using a thermocouple thermometer (Fluke 52 II, Fluke Corporation, USA) with aircoditiner operating.

Initial measurements with the room's air-conditioner turned on demonstrated sensitivity to temperature. Monitoring the room temperature for 5 hours revealed temperature fluctuations driven by the air conditioner in the order of $\pm 4^\circ\text{C}$ (Figure 43). In subsequent measurements, the air-conditioner was turned off (room temperature variation less than $\pm 1^\circ\text{C}$) and a shield was used to minimize fluctuations in the air between the fibres.

Figure 44 shows phase and amplitude measurements recorded by the lock-in amplifier with the air-conditioner turned off. A power meter (Nova, Ophir Optronics, Israel) measures a fraction of the source laser power to monitor any source fluctuations. The air-conditioner was turned on during the measurement after 18 minutes. This is indicated by the vertical line in Figure 44. The phase and amplitude both changes abruptly

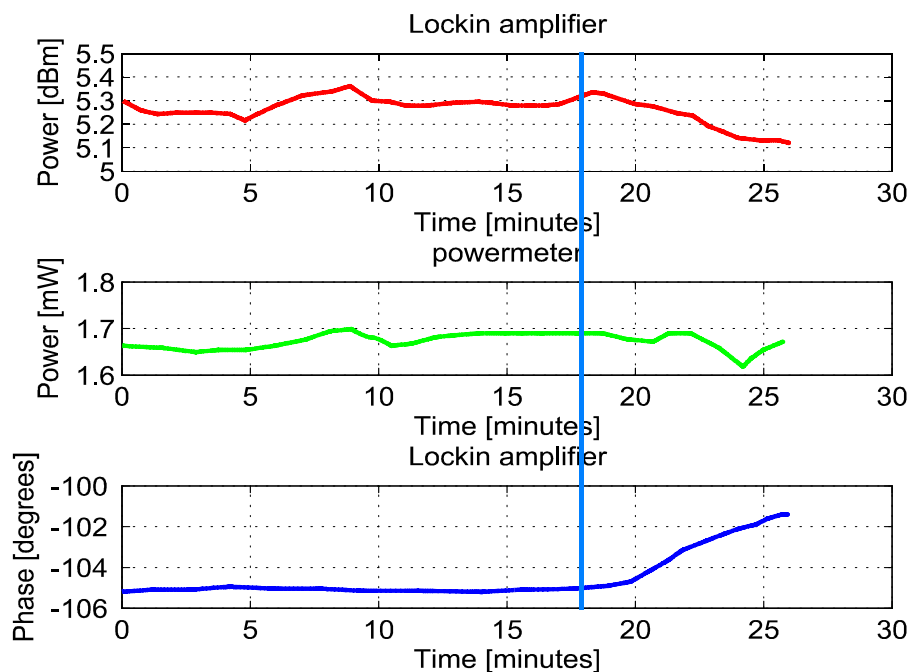


Figure 44 Effect of room temperature variation on the amplitude and phase measurements made by the lock-in amplifier. The line indicates a change in room temperature due to turning the air conditioner on.

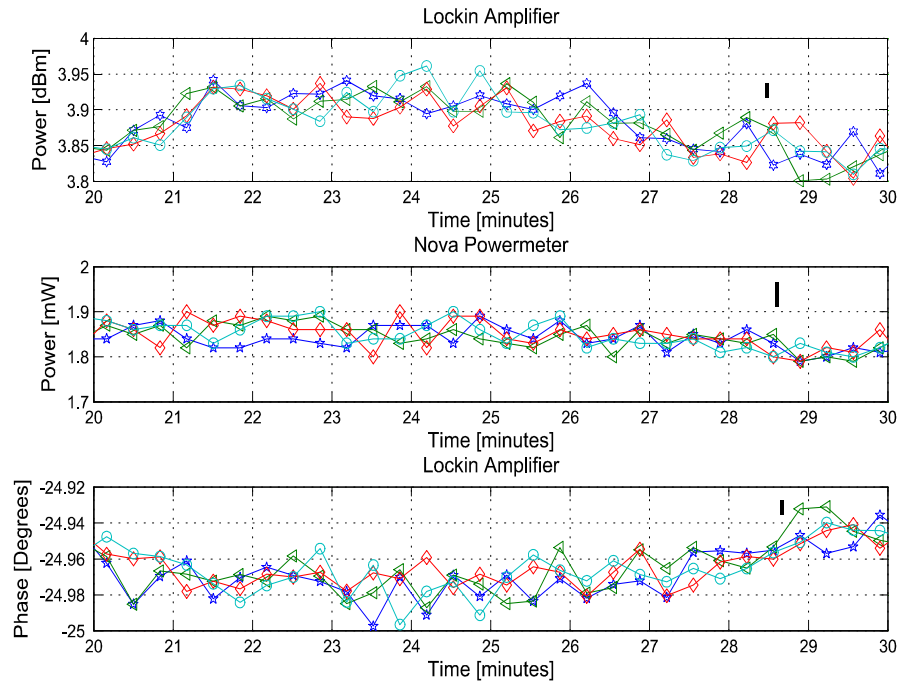


Figure 45 Amplitude and phase of the modulation measured over a 10 minute period by the locin amplifier. These measurements were made by placing the source and detector fibres facing each other in air. The second subplot shows the direct unmodulated source power measured by a power meter.

due to the change in room temperature. The change in temperature introduces a change in phase measurement in the order of 5° .

Figure 45 shows the phase and amplitude of the modulated source recorded by the lock-in for a period of 30 minutes (a scan of the detector fibre from 10 to 30 mm takes nearly 7 minutes) with the air conditioner turned off.

Figure 45 shows a variation in amplitude of approximately ± 0.1 dBm and a phase variation in the order of $\pm 0.04^\circ$ over a period of 10 minutes, when room temperature is stable. This indicates an amplitude stability of 0.3% and phase stability of 0.1% compared to the amplitude and phase changes expected in Intralipid.

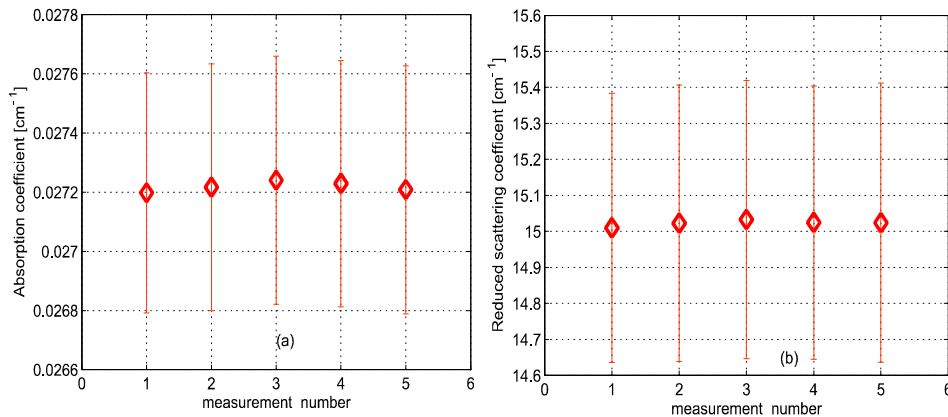


Figure 46 Five repeated measurements of (a) absorption and (b) reduced scattering coefficients made at 790 nm at source modulation frequency 50 MHz. The error bars represent standard deviation for 10 repeated measurements of amplitude and phase corresponding to each data point.

To check the precision and accuracy of the estimated optical properties we have made absorption and reduced scattering coefficient measurements in a tissue simulating phantom. Figure 46 shows repeated measurements of optical properties at 790 nm. Detectors play an important role in the measurements of optical properties. The instrument performance was evaluated by making measurements at a wavelength which is near to the peak response wavelengths of many available detectors. Again these estimates are based on a source modulation frequency of 50 MHz.

Accuracy is defined as how close we can estimate a quantity to its true value (Pifferi et al. 2005). For absorption measurements in turbid media, accuracy can be determined by comparison with absorption measurements in non-scattering samples of the absorbing medium. As the main absorbing species in Intralipid is water (van Staveren et al. 1991), and the absorption of water is well documented, this comparison may seem straight forward. However, there is a large spread even in the absorption coefficient reported for water in the literature. Here we use the most recently reported water data for comparison (Kou et al. 1993). Kou et

al. reports an absorption coefficient of 0.024656 cm^{-1} , comparing to this value the accuracy in the absorption coefficient measurement is within 10%.

The precision, or short term repeatability, is calculated from the repeated absorption coefficient measurements shown in Figure 46 (a). These measurements give a coefficient of variation (Pifferi et al. 2005) of 0.0006 cm^{-1} and 0.00056 cm^{-1} for the absorption and reduced scattering coefficient respectively. The precision is approximately 3% for the absorption and 6% for the reduced scattering coefficient. This compares well with measurements reported in the literature. Sun et al. (2002), for example, report a precision of 7% for the reduced scattering coefficient.

4.7 Summary

The main components in the fabrication of a frequency domain photon migration spectrometer have been discussed. The experimental procedure for optical property measurement using the constructed frequency domain spectrometer is indicated in section 4.6.3. The phase and amplitude stability of the source modulation was checked and found to be suitable for optical property measurements. The spectrometer was tested for accuracy and precision by making optical property measurements at a representative wavelength in a tissue simulating phantom. The phase-amplitude crosstalk effect was quantified by making measurements using a variable neutral density filter and found to be sufficiently small to have no effect on optical property measurements.

CHAPTER 5

OPTICAL PROPERTIES OF INTRALIPID®

5.1 Introduction

This chapter describes the validation of the constructed wavelength tuneable frequency domain photon migration spectrometer by measurements of optical properties in a turbid sample. The setup was tested by measuring the optical absorption and reduced scattering coefficient of Intralipid® at five dilutions in the therapeutic window between 710 and 850 nm at 10 nm intervals. The instrument performance was evaluated comparing the measured optical properties with published data and Mie theory predictions based on independent particle size measurements.

5.2 Method



Figure 47 Intralipid 20% bottle along with the sample container setup.

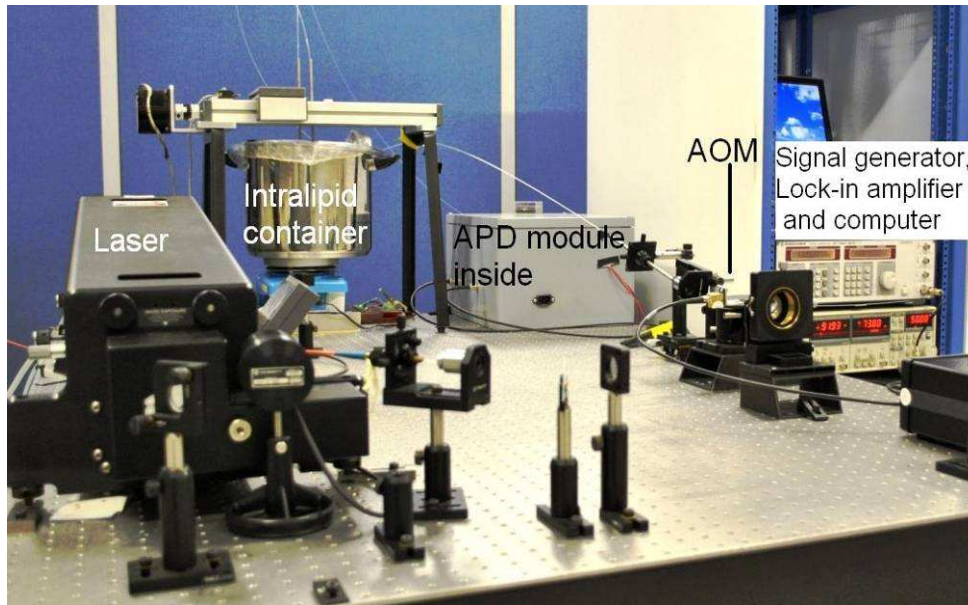


Figure 48 Complete experimental setup.

The optical properties of the tissue phantom Intralipid®-20% (Pharmaco, New Zealand) were measured after dilution with distilled water to lipid concentrations of 0.94, 1.80, 2.59, 3.32, and $4.00 \pm 0.01\%$ (w/w). Measurements were made in a large (10 L, 26 cm diameter, 21 cm height) stainless steel pot filled with 5.5 to 6 L of solution. To prevent settling and maintain a uniform temperature distribution, the solution was gently stirred with a magnetic stirrer (VELP Scintifica, Italy). A loose polythene sheet covered the top of the steel pot to prevent water evaporation. The temperature of the solution was monitored during measurements and found to be $22 \pm 0.5^\circ\text{C}$ throughout the experiment.

The fibre geometry was similar to the infinite medium illustrated in Figure 9 (a). The distance between source and detector fibres was varied from 10 to 30 mm in 0.8 mm steps. Five replicate measurements of amplitude and phase delay were collected at each position. The optical properties were calculated from these measurements at each wavelength and concentration using equations 41 and 42.

To provide a separate estimate of the reduced scattering coefficient of the turbid sample, the particle size distribution of our Intralipid[®]-20% stock solution, diluted to 1% lipid concentration, was measured using a Mastersizer 2000 (Malvern Instruments Ltd., UK). The reduced scattering coefficient was calculated from the particle size distribution using Mie theory. A MathCAD program calculated the reduced scattering coefficient of the Intralipid[®] sample based on Mie theory (Künnemeyer 2008). The MathCAD code is given in APPENDIX III.

5.4 Amplitude and phase measurements

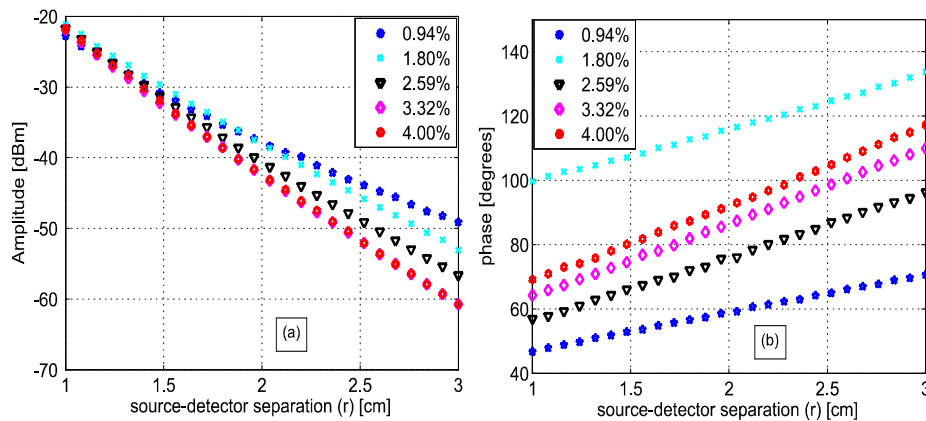


Figure 49 Amplitude (a) and phase (b) data recorded by the lock-in amplifier are plotted against source detector separation. These data corresponds to a wavelength of 750 nm at five different Intralipid concentrations.

Figure 49 shows the amplitude and phase measured by the lock-in amplifier plotted against source detector separation. Measurements were recorded at five different Intralipid concentrations (0.94%, 1.8%, 2.59%, 3.32%, and 4%) at 750 nm wavelength are shown. In Figure 50, the amplitude has been normalized to -1 dBm at 1 cm and phase shift to 1 radian at 1 cm for clarity. This eliminates small source drifts between measurements from the plot, but does not affect the optical properties reported below, which are all based on slopes. Across all wavelengths, we observed that the magnitude of the amplitude-separation slope increased

with concentration. The same was true for phase, which also showed a consistent relationship with concentration.

Figure 50 illustrates both the phase and the logarithm of source-detector separation multiplied by AC amplitude varies linearly with source-detector separation.

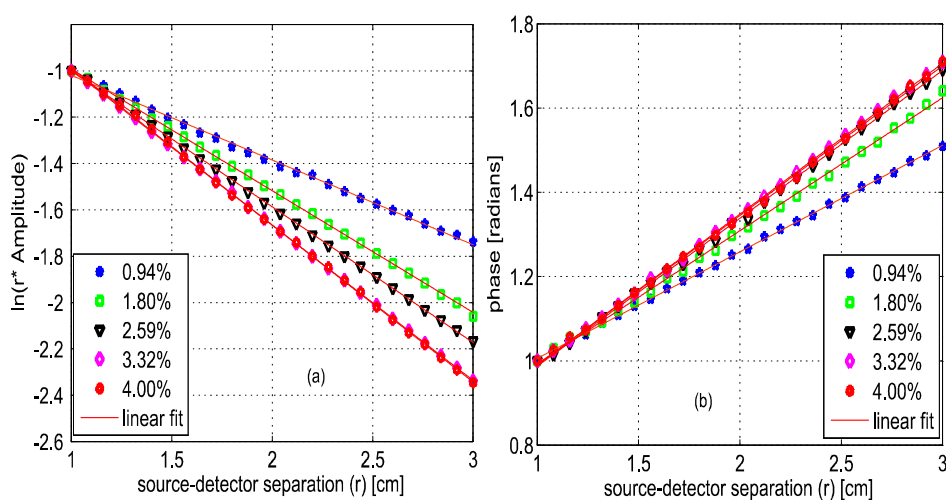


Figure 50 (a) Logarithm of source-detector separation times normalized AC amplitude and (b) normalized phase variation versus source-detector separations at 750 nm for five Intralipid concentrations.

5.5 Intralipid particle size measurements

Figure 51 shows the particle size distribution measured by the Mastersizer 2000. The Mastersizer uses laser diffraction to make particle size measurements. The particles pass through a focussed laser beam. The scattered light intensity is measured by a number of detectors placed to cover a wide range of angles to measure the light scatter angle. The scattering angle, which is inversely proportional to the size of the particle, is used to evaluate the particle size. The particle distribution of Intralipid®-10% reported by van Staveren et al.(1991) is included for comparison. We have presented the particle distribution as a volume fraction here, as particle size, rather than mass, more directly affects scatter cross-section;

the large number of small particles identified by van Staveren et al. only make a small contribution to the reduced scattering coefficient.

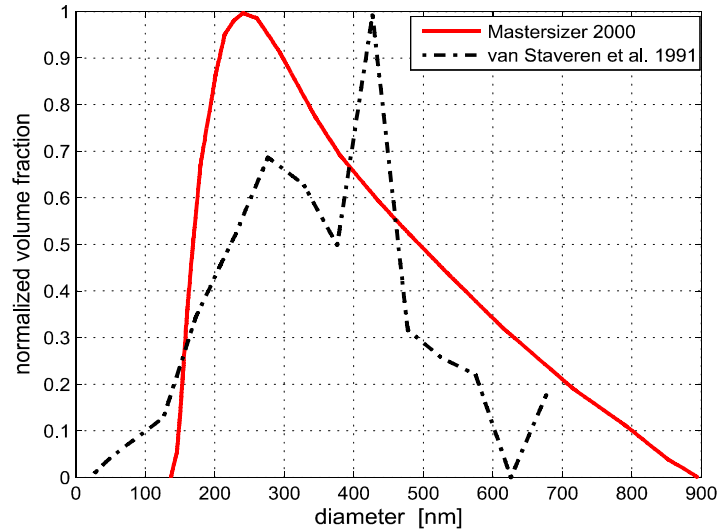


Figure 51 Volume fraction of Intralipid 20% particles measured with a Mastersizer 2000. This distribution is used in our Mie theory calculations. Data by van Staveren et al. (van Staveren et al. 1991), converted to volume fraction, are included for comparison.

Both results have a peak particle size between 200 and 300 nm. The peak in van Staveren et al.'s data around 425 nm is caused by noise in their data which is exaggerated for small numbers by our conversion from number density to volume fraction.

5.6 Absorption and reduced scattering coefficient estimation

The average absorption and reduced scattering coefficients at each concentration and wavelength were calculated using equations 41 and 42. Errors were estimated by propagation of uncertainties from the replicate measurements. The MATLAB code used to estimate the errors is given in APPENDIX I.

The calculated absorption coefficient is plotted in Figure 52. It shows a characteristic water absorption peak around 740 nm and the tail of the

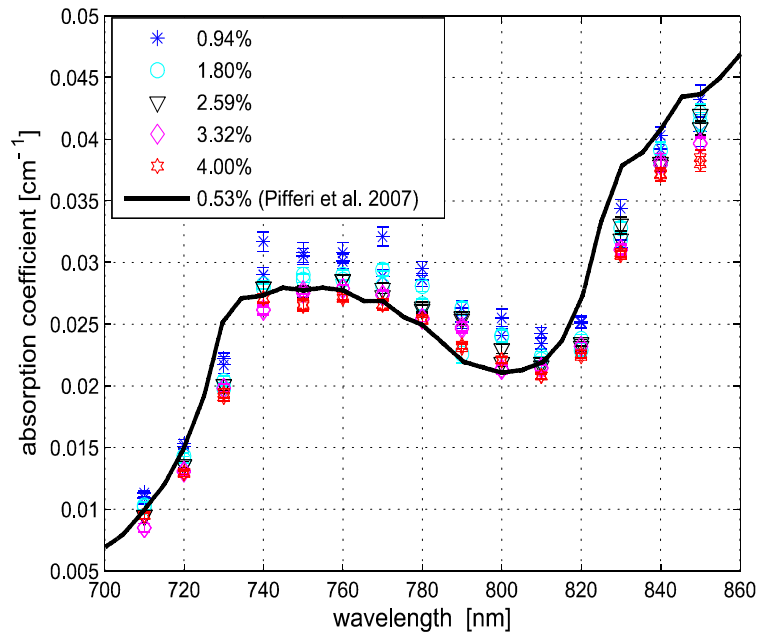


Figure 52 Absorption coefficient of Intralipid. Data reported by Pifferi et al. (Pifferi et al. 2007) are included for comparison. The error bars indicate 95% confidence interval.

970 nm water absorption peak, as might be expected from a solution that is predominantly water. In general, the absorption coefficient decreases as the concentration of Intralipid® increases.

The absorption coefficient of 0.53% (solid fraction) Intralipid®-10%, reported by Pifferi et al. (2007), is included for comparison. Pifferi et al. used time-correlated single photon counting to obtain their estimate of the absorption coefficient. The absorption coefficient agrees in shape but is lower from 740 to 810 nm and higher from 820 to 850 nm than our results. This is not consistent with the relationship between concentration and absorption observed in our data; we will explore this further below.

Figure 53 shows the reduced scattering coefficient calculated from the frequency domain measurements and Mie theory using the particle size distribution plotted in Figure 51. Three Intralipid® concentrations of 0.94%, 2.59%, and 4% were used in the Mie theory calculation to facilitate comparison with the frequency domain result.

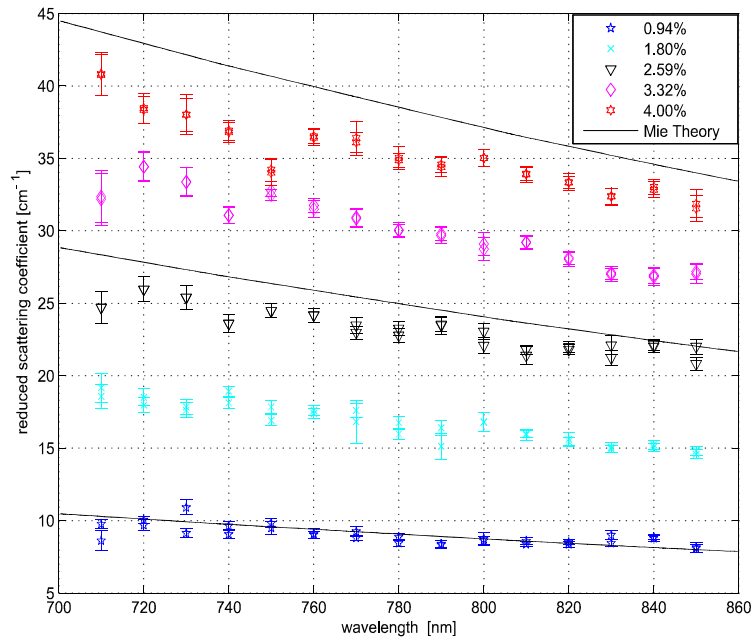


Figure 53 Reduced scattering coefficient of Intralipid. The solid lines correspond to Mie theory estimates, based on our particle size measurements, for 0.95, 2.59 and 4.0% lipid concentration. The error bars indicate 95% confidence interval.

Again, there is a clear correlation with the reduced scattering coefficient increasing as Intralipid® concentration increases. Both, frequency-domain and Mie results show a steady decrease in the reduced scattering coefficient as wavelength increases as reported in the literature (Bevilacqua et al. 2000; Mourant et al. 1997). However, we found the Mie theory estimate of the reduced scattering coefficient overestimated our frequency-domain result by about 6% at most wavelengths. This is significantly larger than the random error in the frequency-domain result (approximately 0.1%). It may reflect a systematic error in one, or both, of the methods. The difference in the reduced scattering coefficient between Mie theory and frequency domain estimates at various Intralipid concentrations is plotted in Figure 54. This discrepancy varies with wavelength and is larger as concentration of Intralipid goes higher. This may be an indication of failure of Mie theory and diffusion equation which does not account for the shadowing of particles at higher scatter concentrations.

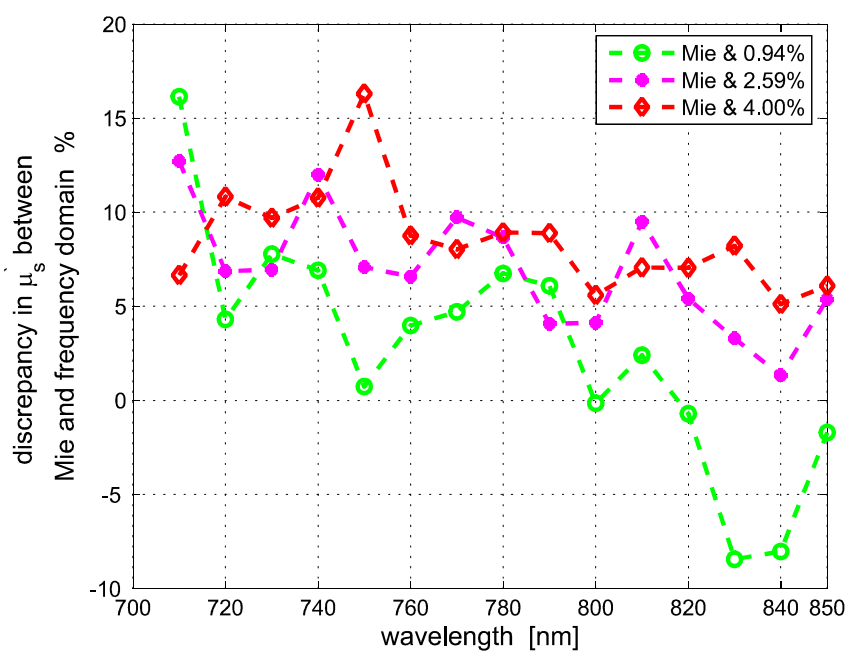


Figure 54 Difference between reduced scattering estimated by Mie theory and frequency domain measurements plotted against wavelength.

5.7 Validating optical property measurements

In this section we analyse and compare the measured optical properties of Intralipid with published results. Collecting absorption measurements at many concentrations allowed us to extrapolate and estimate the absorption coefficient of the pure absorber. In the near-infrared, the main absorbing species of Intralipid® is water (van Staveren et al. 1991; Flock et al. 1992), which provides an independent validation of the absorption measurement. Water concentration was calculated by dividing the mass of water by the total mass of the Intralipid® sample to allow for soluble constituents.

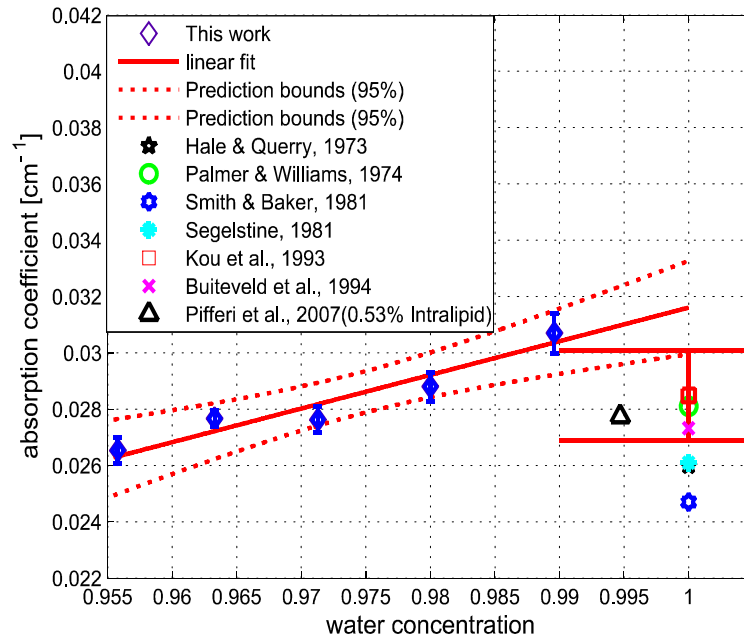


Figure 55 Absorption coefficient of Intralipid at 750 nm plotted against water concentration along with literature data. The dotted lines indicate 95% confidence interval for the linear fit.

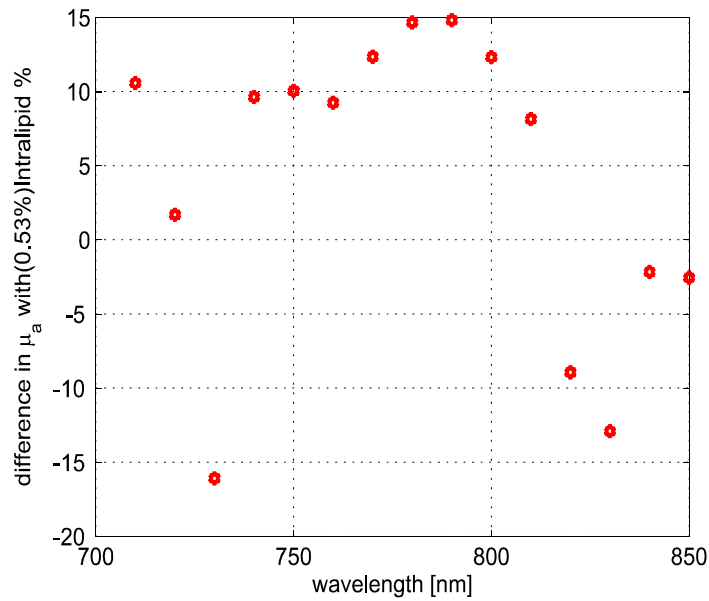


Figure 56 Discrepancy between extrapolated absorption at a water concentration equivalent to 0.53% Intralipid absorption reported by Pifferi *et al.* (2007) plotted against wavelength.

Figure 55 illustrates a typical relationship, measured at 750 nm, between absorption and concentration. A linear fit, with 95% confidence intervals is

included. For comparison, water absorption reported by six other groups (Hale and Querry 1973; Palmer and Williams 1974; Smith and Baker 1981; Segelstein 1981; Kou et al. 1993; Buiteveld et al. 1994) and absorption of Intralipid® (0.53%) reported by Pifferi et al. (2007) are included. Only the data reported by Kou et al. included an estimate of error, which is also included on the plot.

In this case, the extrapolated absorption coefficient overestimates the most recent water absorption measurements by about 12%, though the error is not the same at all wavelengths. At 750 nm, the measurement reported by Pifferi et al. (2007) is about 11% below the extrapolated value for 0.53% Intralipid®. However, as Figure 56 shows, this discrepancy also varies with wavelength reaching maximum of 15% at 780 and 790 nm.

The extrapolation shown in Figure 55 can be applied across all

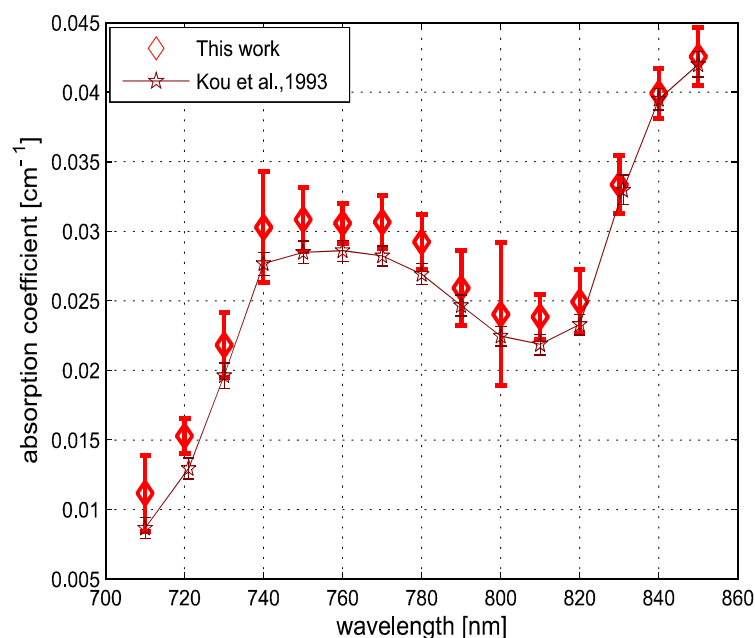


Figure 57 Extrapolated absorption coefficient (triangular markers with error bars) for water from Intralipid measurements versus wavelength. The solid curve represents water absorption data reported by Kou *et al.* (1993). The error bars correspond to ± 2 standard deviations.

wavelengths to estimate the spectrum of the pure absorber (Kou et al. 1993). The water absorption data reported by Kou et al. (1993) are included for comparison; these data were also measured at 22°C, include standard errors and show good agreement with the work of Downing and Williams (1975), and Palmer and Williams (1974) who used similar methods. With water the main absorbing component of Intralipid®, it is not surprising to find our extrapolated absorption coefficient closely follows that of water. However, a weighted mean difference of $0.0022 \pm 0.0003 \text{ cm}^{-1}$ indicates a statistically significant discrepancy between the two data sets. This probably indicates systematic problems in the measurements or flaws in the underlying theory.

The discrepancy between water absorption data from our extrapolation and the water data reported by Kou et al. is indicated in Figure 58. It shows a maximum of 23% at 710 nm and 15% at 720 nm. At all other

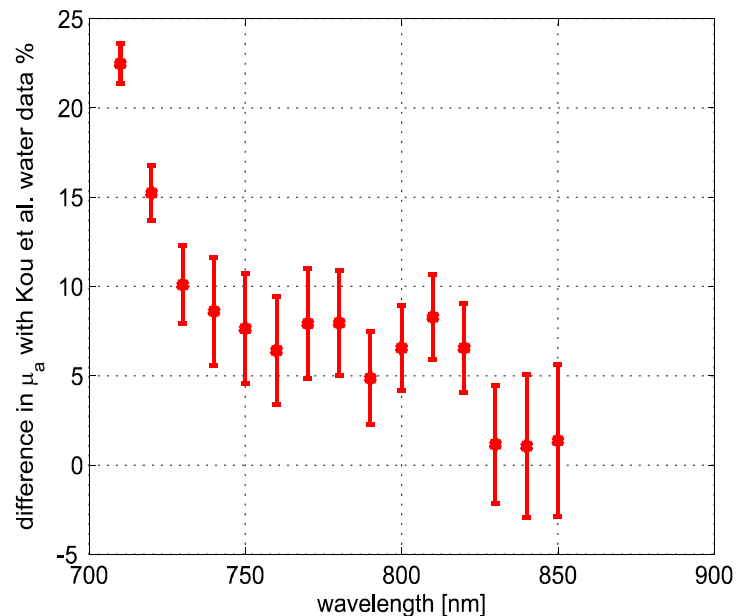


Figure 58 Discrepancy between extrapolated water absorption from our measurements and the pure water absorption data reported by Kou *et al.* (1993) plotted against wavelength.

wavelengths the difference between water data reported by Kou et al. and our extrapolation remains within 10%.

We believe there are no other absorbers in Intralipid®-20% strong enough to introduce this discrepancy. In any case, we found comparison with water absorption data a robust, quantitative approach for validating an instrument's capability of measuring the absorption coefficient.

A similar analysis can be applied to the reduced scattering coefficient, though it is nonsensical to extrapolate to a "pure scattering medium". At high scatter concentrations, the relationship between the scattering coefficient and concentration is not linear because individual scattering particles can mask their neighbours. Figure 59 shows the reduced scattering coefficient at 750 nm plotted against Intralipid® concentration. Reduced scattering values, calculated by Mie theory using our measured volume fractions, are included for comparison. At lower concentrations,

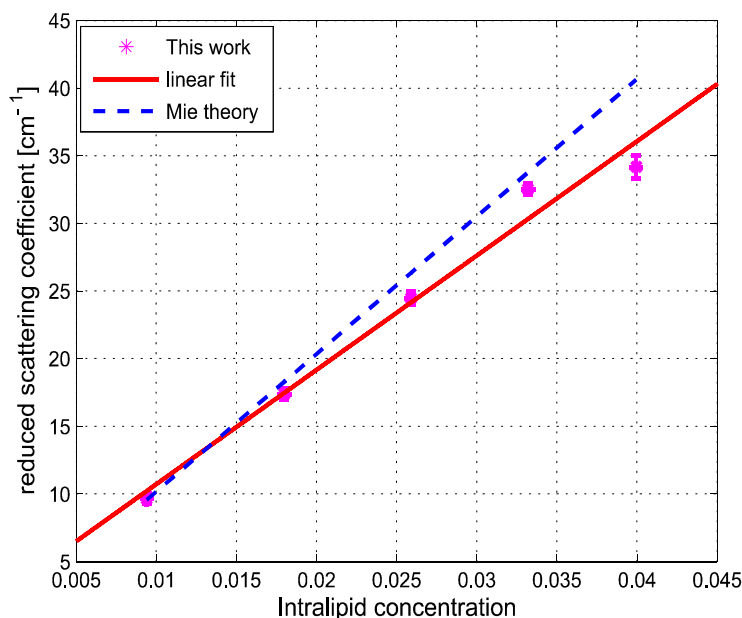


Figure 59 Reduced scattering coefficient at 750 nm versus Intralipid concentration. The error bars indicate 95% confidence intervals. The solid line is a linear fit to the experimental data. The dashed line shows the Mie theory results.

the theoretical values are in good agreement with the measured reduced scattering coefficients. As the concentration of Intralipid[®] increases, the measured reduced scattering coefficient drops below the predictions of Mie theory.

Previous reports (Giusto et al. 2003; Zaccanti et al. 2003) have shown that the linear relationship between reduced scattering coefficient and particle concentration breaks down at higher Intralipid[®] concentrations though van Staveren et al. (1991) reported that a linear relationship between concentration and the reduced scattering coefficient holds reasonably well up to 4% at 1100 nm.

To compare with other published data we have linearly interpolated our data and linearly scaled literature data to 2% Intralipid[®] concentration, well within the linear range. Figure 60 shows the result. Included are the reduced scattering coefficient for Intralipid[®]-20% (2% solution) reported by other frequency domain (Coquoz et al. 2001; Xu and Patterson 2006), time resolved (Spinelli et al. 2007), and continuous wave (Martelli and Zaccanti 2007) methods. Xu and Patterson report scattering data at 750 nm by making measurements in diluted samples of Intralipid[®]-20% in water from 0.3 to 2% concentration. Coquoz et al. report reduced scattering coefficients at 811 and 849 nm by making measurements in a solution of Intralipid[®] with an added absorber. The reduced scattering reported by Spinelli et al. and Martelli and Zaccanti for Intralipid[®]-20% is scaled down to a 2% concentration for comparison. Overall, our results are in good agreement with other measured data. The scattering values reported by Chen et al. (2006) are 30% lower than our results and results published in the literature so they are not included in the diagram.

Figure 60 also shows the reduced scattering coefficient calculated by Mie theory using our particle size measurements, as well as values derived

from van Staveren et al.'s (1991) fit to Mie theory data. Calculated values reported by Michels et al. (2008) for Intralipid®-20%, scaled down to a 2% concentration, closely follow our own Mie theory predictions. Our experimental results are below our Mie calculations by about 6%, with a larger deviation at lower wavelengths. The discrepancy between our experimental results and van Staveren et al.'s values is about 11% across the whole wavelength range.

These discrepancies may be due to a change in size distribution because of slight differences in manufacturing recipes for Intralipid® (Michels et al. 2008). However, a discrepancy between experimental and Mie theory values has also been reported for measurements in a microsphere suspension (Coquoz et al. 2001). Coquoz et al.'s experimental results overestimated the reduced scattering by 6.5 to 28% at 811 nm and 1 to 8%

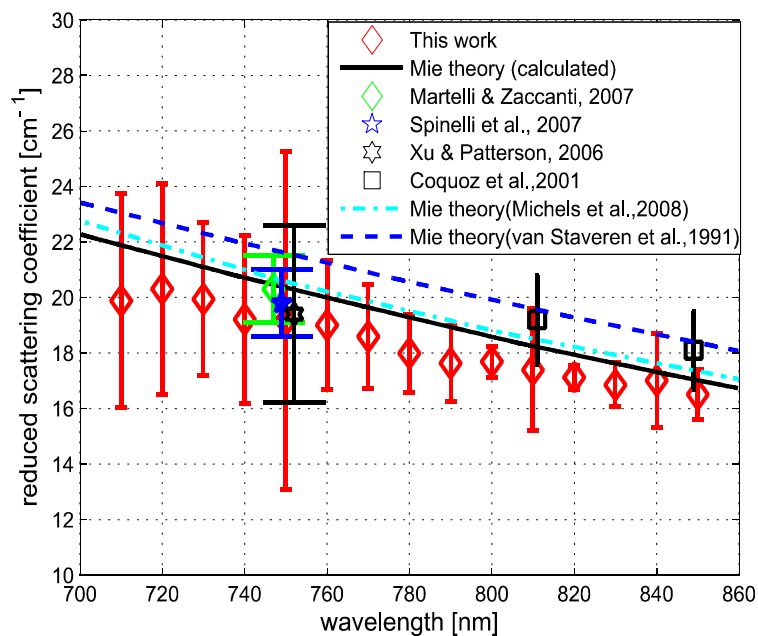


Figure 60 Reduced scattering coefficient (triangular markers with error bars) values for a 2% solution of Intralipid plotted against wavelength. The solid line corresponds to the Mie theory values calculated based on our particle size measurement. Data reported at 750 nm is staggered a little to make them visible. The error bars indicate 95% confidence interval.

at 849 nm compared to Mie theory values.

Our results are consistent with the literature and confirm that the experimental set-up is capable of measuring the absorption and reduced scattering coefficient of Intralipid®. Using acousto-optic modulation of a tuneable laser in a frequency domain photon migration instrument is a viable approach to measure the optical properties of liquid turbid media.

5.8 Influence of glucose on the optical properties of Intralipid

This section explores the optical properties of Intralipid in the presence of glucose. Monitoring glucose in aqueous solutions by changes in absorption coefficient is particularly difficult because of the way these sugars interact with water molecules (Giangiaco 2006). However monitoring the reduced scattering coefficient provides an efficient method. This experiment was conducted with the aim of exploring potential application in blood glucose monitoring. Also, sugars may find application in optical clearing as the addition of sugar causes a reduction in scattering (Hirshburg et al. 2007).

5.8.1 Method

Phase and amplitude measurements were collected in a 1% Intralipid solution (w/w), prepared as described in the previous chapter, in the wavelength range from 710 to 850 nm. The first set of measurements was done at low glucose concentration in Intralipid: 200, 400 and 600mg/dL. Absorption and reduced scattering coefficients were estimated from the phase and amplitude measurements at each glucose concentration.

A fresh Intralipid solution (1%) was prepared and the measurements were repeated at three glucose concentrations namely 1000 mg/dL, 2000 mg/dL and 4000 mg/dL.

5.8.2 Influence on absorption

Figure 61 shows the absorption coefficient calculated at three concentrations (200 mg/dL, 400 mg/dL and 600 mg/dL) of glucose in Intralipid. The absorption coefficient of Intralipid without glucose is also included. The estimated absorption coefficient does not show any consistent correlation with glucose concentration.

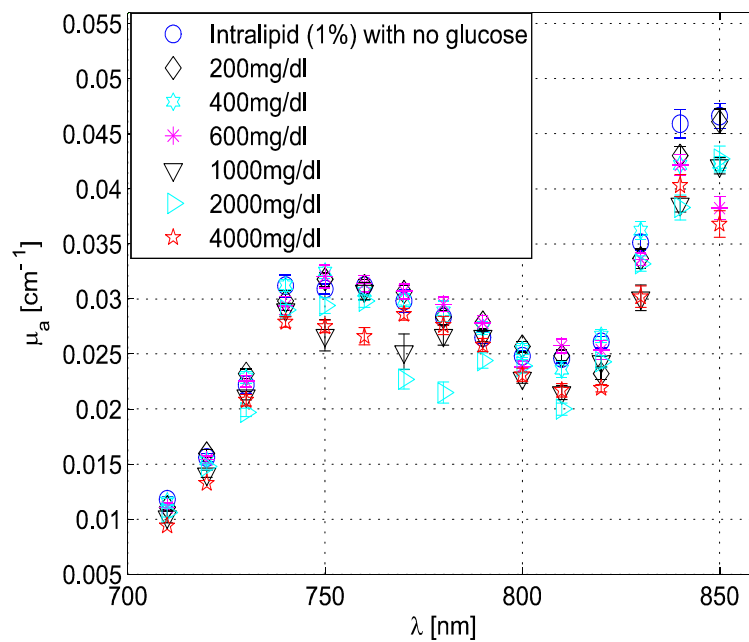


Figure 61 Calculated absorption coefficient of Intralipid with high concentrations of glucose solution.

However, some individual wavelengths show peculiarities. For example, at 740 nm the absorption has a decreasing trend with increasing concentration of glucose. A similar behaviour can be observed for wavelengths above 800 nm. As the main absorbing species in Intralipid is water, this result demonstrates the complex behaviour of glucose interaction with water that has been widely reported in the literature (Giangiacomo 2006).

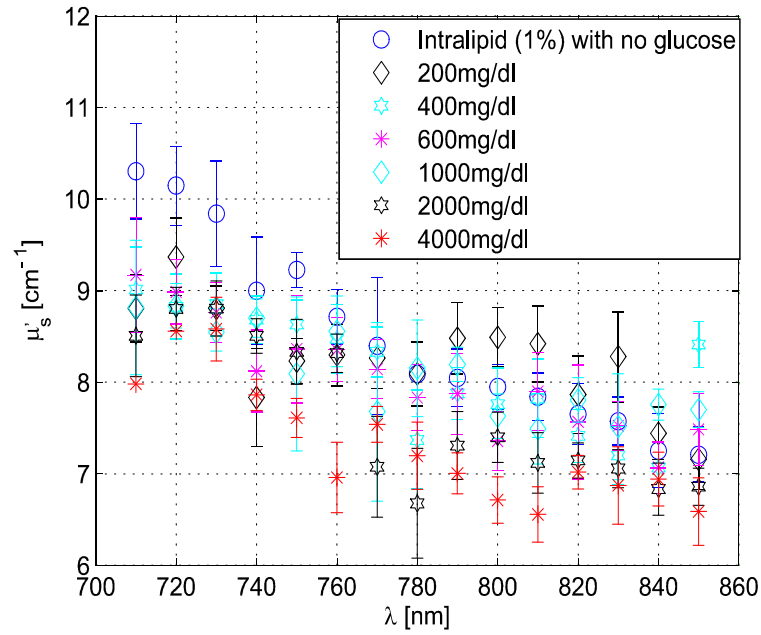


Figure 62 Reduced scattering coefficients of Intralipid at higher glucose concentrations plotted against wavelength.

5.8.3 Influence on reduced scattering

Figure 62 shows the reduced scattering coefficient estimated in Intralipid in the presence of low glucose concentrations. Below 760 nm the reduced scattering coefficient tends to decrease as glucose concentration increases. However, this trend is not present above 760 nm.

At lower glucose concentrations the behaviour of the reduced scattering coefficient with changes in glucose concentration is inconsistent across wavelength. The reduced scattering seems to increase at all wavelengths below 790 nm and decreases at wavelengths above 790 nm with increasing glucose concentration. Figure 62 illustrates the trend in reduced scattering coefficient with higher glucose concentration. In this case, the reduced scattering coefficient decreases at almost all wavelengths as glucose concentration increases.

From Figure 62, 740 nm seems to be a good choice for monitoring glucose based on change in reduced scattering coefficient, as 740 nm shows a gradual decrease in the scattering as glucose concentration increases.

5.8.4 Possibility of glucose monitoring in turbid media

Analysing the absorption coefficient estimated at various concentrations of glucose in Intralipid shows that there is no correlation between the absorption coefficient and glucose except perhaps at 730 nm. The absorption coefficient measured at 730 nm shows a linear decrease with the glucose concentration from 200 to 1000 mg/dL as shown in Figure 63. At concentrations below 200 mg/dL this behaviour is not visible; this indicates that the sensitivity of the instrumentation is not enough to observe the minute changes. However, additional measurements made at concentrations higher than 1000 mg/dL show that the absorption is not affected by glucose and is illustrated in Figure 63.

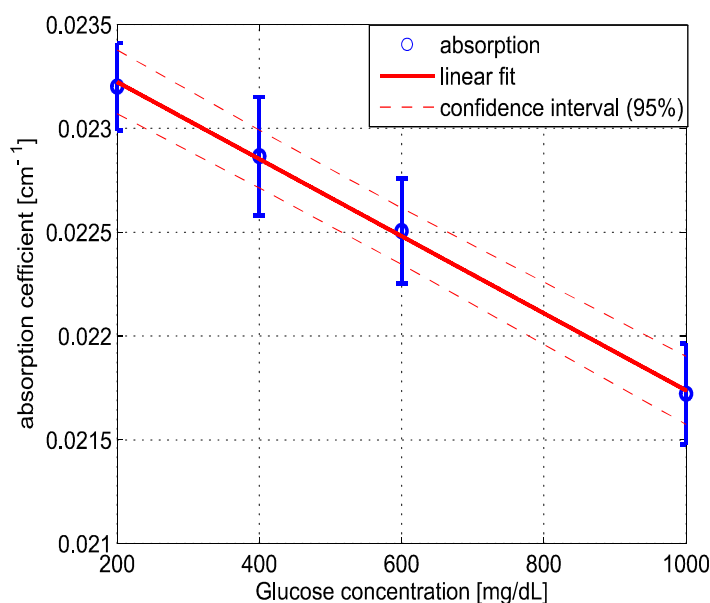


Figure 63 Absorption coefficient estimated at 730 nm plotted against glucose concentration in Intralipid. The red line corresponds to a linear fit to the data. The dotted line indicates 95% confidence interval for the fit.

Scattering variations due to glucose in turbid media as a means to monitor blood glucose levels have been reported by many groups (Maier et al. 1994; Kohl et al. 1994; Zhao and Myllylä 2001). These measurements were performed in Intralipid, polystyrene sphere solution and blood.

These results were able to predict the concentration of glucose with varying degree of success. A good review of non invasive blood glucose monitoring using various near infrared spectroscopic technique can be found in Khalil (1999). These measurements demonstrate substantial research is still needed to successfully measure glucose concentration in solution.

Our data analysis reveals the complex nature of interaction of glucose on absorption coefficients at all wavelength investigated. However the correlation observed at 730 nm between the absorption and glucose concentration seems interesting enough for further research. The reduced

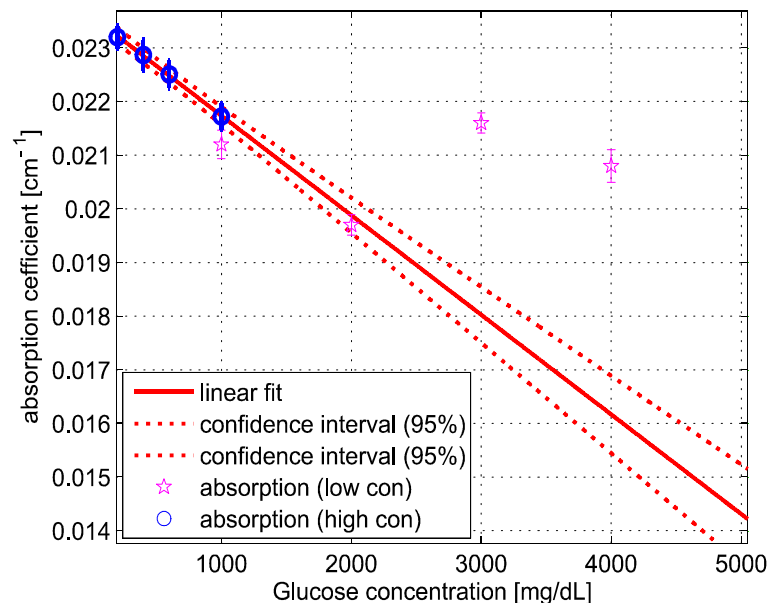


Figure 64 Absorption coefficient estimated at higher concentrations (magenta data points) plotted against concentration. The linear fit does not include the magenta data points.

scattering coefficient shows a decreasing trend with increasing glucose concentration as observed by many others. Further research is needed to validate instrument performance, for example by comparing the absorption and temperature effect on the absorption with glucose.

5.9 Summary

The instrument performance was evaluated with measurements of Intralipid®-20%, at five concentrations (0.94–4.0%), in the therapeutic window (710–850 nm). We obtained measurements with standard errors of 1% for the absorption coefficient and less than 2.5% for the reduced scattering coefficient.

We found the absorption coefficient decreased as Intralipid® concentration increased, consistent with the liquid phase being the dominant absorber. We extrapolated the relationship between absorption and concentration to estimate the absorption of the liquid phase. The absorption of the liquid phase was found to follow closely that of pure water, but overestimating it by about 10%. It was not clear from our measurements whether this difference was due to additional absorbing species in the liquid phase or systematic errors in the measurements. In either case, we found comparison with water absorption a useful technique for validation of Intralipid® measurements.

We found a clear linear correlation between the reduced scattering coefficient and concentration of Intralipid across all wavelengths. We interpolated our measurements, and results reported in the literature at 750 nm, to a common concentration of 2% for comparison. Our results were consistent with prior literature at discrete wavelengths, within experimental error. The reduced scattering coefficient was also compared with an estimate calculated from particle-size distribution using Mie theory. We found the Mie theory calculation overestimated our frequency-

domain measurement and previous reports in the literature by about 6%. Mie theory requires that the inter particle distance is larger than 3 to 5 particle diameters when calculating the reduced scattering coefficient. This is certainly not true in our case as the concentration of Intralipid increases.

These results show that a tuneable-laser can be used with an acousto-optic modulator to measure the absorbing and scattering properties of turbid liquids over a moderate wavelength range. Collecting data over a broader range than has been previously explored, has aided comparison with the intrinsic properties of the turbid medium's constituents. Potential systematic discrepancies between the different techniques have been highlighted.

CHAPTER 6

TEMPERATURE DEPENDENCE OF OPTICAL PROPERTIES OF INTRALIPID®

6.1 Introduction

This chapter describes the frequency domain spectroscopic measurements we made to estimate the temperature induced variations in the optical properties of Intralipid®. We have used a 1.8% (w/w) solution of Intralipid® as the sample to simulate the reduced scattering properties of human brain and breast tissues (Cheong et al. 1990). Measurements were made in the physiologically relevant temperature range of 30 to 40 °C while heating and cooling the liquid. This experiment explores the instrument's ability to make practical absorption and reduced scattering measurements.

6.2 Method

The temperature of the medium was maintained using a closed-loop control system incorporating a heated plate (VELP Scientifica, Italy) equipped with a magnetic stirrer and a semiconductor temperature sensor (LM35, National Semiconductor, USA) immersed in the sample as shown in Figure 65. The temperature sensor was placed close to the side of the stockpot. This arrangement ensured the temperature probe would not interfere with the optical measurements. The temperature sensor and the solution heater were connected via a data acquisition device (U 12, LabJack Corporation, USA) to a computer and controlled by a Labview (National Instruments, USA) program. A loose polythene cover minimised water evaporation during the experiment. A 1.8% (w/w) solution of Intralipid was obtained by diluting 500 mL of Intralipid-20% (Pharmaco, New Zealand) in 5 L of distilled water.

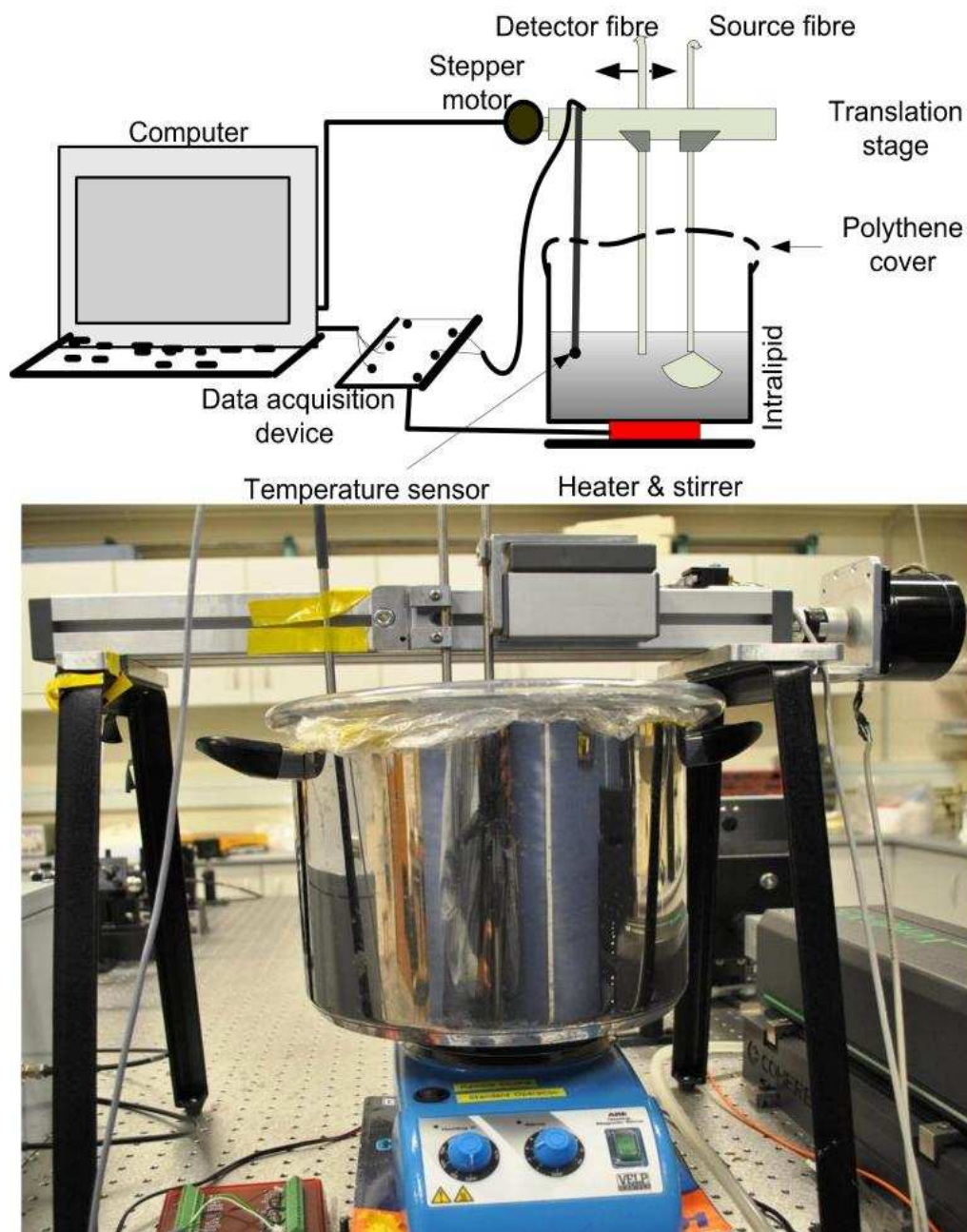


Figure 65 The setup measuring temperature dependence of optical properties of Intralipid. The photograph demonstrates the careful arrangement to prevent water evaporation during heating the Intralipid solution.

Amplitude and phase measurements were initially collected, at 10 nm intervals, between 710 and 850 nm at three different set-point temperatures (30, 35 and $40 \pm 0.5^\circ\text{C}$ – the “low temperature resolution” data) as the distance between the source and detector fibres was increased from 10 to 30 mm (0.8 mm steps).

At each stage-position, five amplitude and phase measurements were recorded to estimate the errors in our results. The temperature control system was allowed to stabilise for at least 30 minutes before collecting each set of measurements. Additional amplitude and phase measurements—the “high resolution” data—were made at 740, 800 and 840 nm at room temperature (22 °C) then as the solution was first slowly heated (over 2 h) from 30 to 40 °C then again as it cooled (over 4 h) and finally again at room temperature. These measurements were collected every 1.1 ± 0.1 °C between 30 to 40 °C over the heating and cooling regimes. Replicate heating and cooling measurements were collected at 740 nm and 840 nm with similar solutions prepared, on different days; a single set of measurements was recorded at 800 nm. Finally, optical measurements were recorded when the solution reached 22 °C after a cooling cycle, then again at 22 °C the next day.

As Intralipid® is known to decay over time, (Whateley et al. 2008) a fresh solution was prepared for each set of measurements.

6.3 Optical property temperature dependence

Figure 66 shows the absorption coefficient of Intralipid, calculated from the amplitude and phase measurements, over the wavelength range 710 to 850 nm measured at the three different temperatures. The absorption coefficient from previous measurements discussed in section 5.6 at 22 ± 0.5 °C is included (Cletus et al. 2009). The error bars at each measurement illustrate ± 1 standard deviation, based on propagating uncertainties in replicate measurements through the calculations. Arrows on the plot show the trend in absorption coefficient with temperature. The absorption coefficient increases around 740 and 840 nm and decreases around 800 nm in response to increasing temperature.

The reduced scattering coefficient, again calculated from the amplitude and phase measurements, is illustrated in Figure 67 for the three temperatures measured in this study and at 22°C discussed in section 5.6 (Cletus et al. 2009). As predicted by Mie theory (Fu and Sun 2001), the reduced scattering coefficient decreases, nearly linearly, as wavelength increases. Moreover, these measurements show the reduced scattering coefficient decreases as temperature increases. The temperature trend is more clearly illustrated for the absorption and reduced scattering coefficients using the data measured continuously as the sample was heated and cooled (Figure 68 and Figure 69 respectively). Each plot illustrates an approximately linear relationship between the optical coefficient and temperature at 740 and 840 nm for two replicate measurements during heating and cooling of the sample. Results at $22 \pm 0.4^\circ\text{C}$ are included for comparison from earlier work discussed in

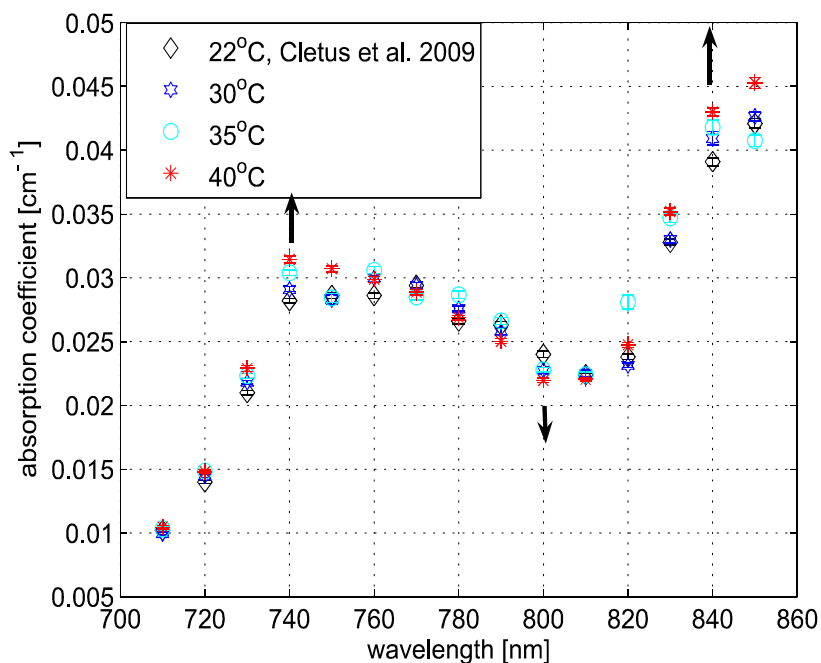


Figure 66 Absorption coefficient at 22°C (triangle), 30°C (hexagram), 35°C (circle) and 40°C (diamond) plotted against wavelength. The change in absorption around 740, 800 and 840 nm is indicated by arrows.

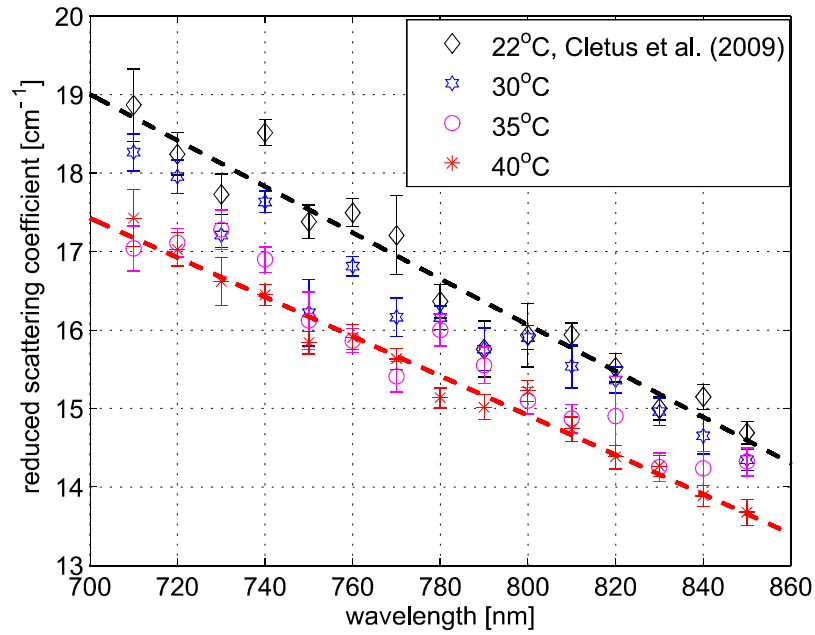


Figure 67 Reduced scattering coefficient measured at different temperatures plotted against wavelength. A linear, least-squares fit at 40 °C (red) and 22 °C (black) show the trend (dashed lines).

section 5.6 (Cletus et al. 2009). Each data point between 30 and 40°C represents the average of five measurements with one standard deviation error bars estimated by propagating the noise in the amplitude and phase measurements through the calculations for the optical coefficients.

As Figure 68 shows, the absorption coefficient increases with temperature at both 740 and 840 nm. This is consistent with the change in absorption coefficient of pure water (Langford et al. 2001), the main absorbing species in Intralipid (Flock et al. 1992). The absorption coefficients over the heating and cooling period match well at 740 nm. However at 840 nm, absorption was generally higher during the cooling period. This may be due to a variation in dilution across the different batches of Intralipid.

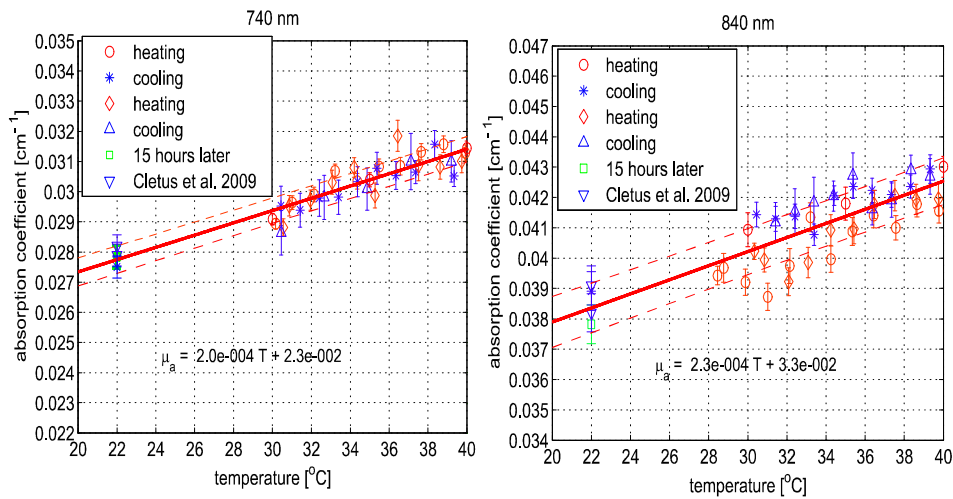


Figure 68 Absorption coefficient at 740 and 840 nm plotted against temperature. The red circles correspond to the heating cycle data and the blue asterisks to the cooling cycle. The solid line is a least square fit to all the data, and the dashed line indicates a 68% confidence interval. The error bars give ± 1 standard deviation.

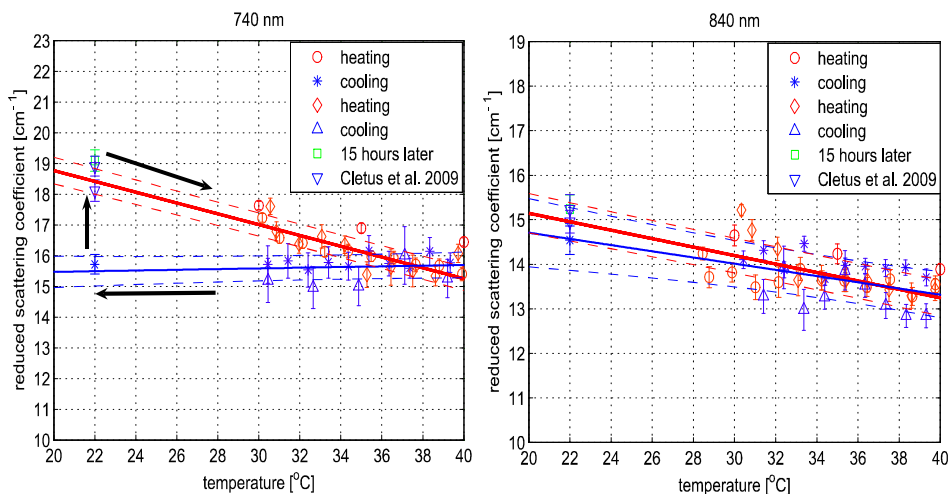


Figure 69 Reduced scattering coefficient at 740 and 840 nm plotted against temperature. The red circles indicate heating and blue asterisks cooling cycles. The solid lines are least square fits to heating and cooling data. The error bars and confidence interval show ± 1 standard deviation.

A temperature coefficient, α , has been estimated using a linear, least-squares fit to the measurements made in the heating and cooling periods. The discrepancy between heating and cooling at 840 nm had no significant effect on the slope so data from the two periods has been combined in all cases. These measurements are in good agreement with results collected at 22 °C both during this work and in the previous validation measurements.

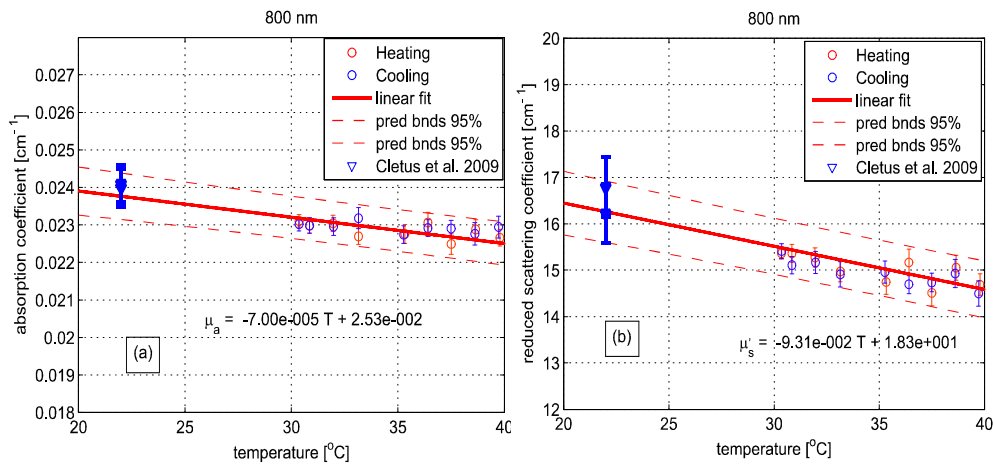


Figure 70 Absorption (a) and reduced scattering (b) coefficient variation at 800 nm plotted against temperature. The error bars and confidence intervals indicate ± 1 standard deviation.

Generally, the reduced scattering coefficient decreased as temperature increased at 740 and 840 nm (Figure 69). However at 740 nm, a hysteresis was observed whereby the reduced scattering coefficient decreased during heating yet remained reasonably constant during cooling, even down to 22°C. This behaviour was observed in both replicates but was not a result of self cooling as the measurement time for a single set (a detector fibre scan from 10 to 30 mm) is about 7 minutes and the change in temperature in this interval is only of the order of 0.2°C. Earlier data at 22 °C and a subsequent measurement at 22 °C (green square) on the following day (15 hours later), indicate that the scattering coefficient recovers to its original value eventually. This behaviour was observed in both replicates at 740 nm but at 840 nm, although the slope is slightly lower during the cooling period, no significant difference was observed between the heating and cooling periods. Kakuta et al. (2008) and McGlone et al. (2007) also observed different behaviour in their measurements during heating and cooling. Kakuta et al. observed discrepancy in their absorbance measurement and postulated that it may be due to the permanent structural changes in the micelles during heating. McGlone et al. also observed different scattering behaviour during heating and cooling.

Because of this hysteresis, the temperature coefficient, β , for the scattering coefficient was estimated using only data from the heating period, with a linear least-square fit.

6.4 Optical temperature coefficients

Accurate knowledge of the optical properties of turbid media, such as tissue, is important in many clinical applications that use light for diagnosis and treatment. The optical properties depend on the physiological state of the tissue and are influenced by many parameters. One such parameter is temperature, which can substantially alter measured optical properties. The effect can be quantified as a temperature coefficient, the rate of increase (or decrease) in absorption (α) and scattering (β) coefficients with temperature.

Jeffrey et al. (1995) measured the near-infrared spectra of chicken, bovine and porcine tissues from 17 to 45 °C with a spectrophotometer and reported that the measurements can predict tissue temperature with a standard error less than 0.2 °C. Laufer et al.(1998) measured the change in optical properties of human dermis and sub-dermis from 25 to 40 °C. They observed positive and negative temperature coefficients of scattering for dermis and sub-dermis, respectively, but no change in absorption with temperature. Temperature induced change in the optical properties can, for example, limit the application of photodynamic therapy (Svensson et al. 2005).

Other applications include the estimation of temperature itself from changes in optical properties. Temperature can be estimated from changes in absorbance (Kakuta et al. 2008), however in turbid media variation in scatter introduces an uncertainty in the path length making it difficult to reliably estimate temperature from optical extinction coefficients. Uncoupling the effect of scattering on absorption may reduce this

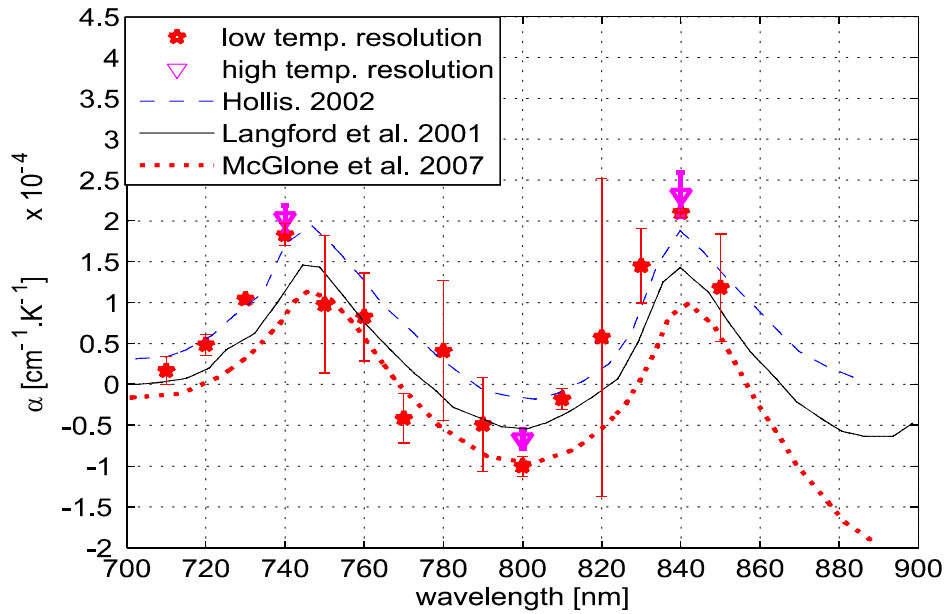


Figure 71 Temperature coefficient of absorption for 1.8% solution of Intralipid plotted against wavelength. Temperature coefficient for pure water reported by Hollis, Langford et al. and the temperature coefficient for Intralipid (1%) by McGlone et al. are also included. Error bars indicate 68% confidence intervals.

obscurity, offering the potential for accurate measurements of temperature in turbid solutions. The frequency domain technique uncouples absorption from scattering (Cerussi et al. 2001) when determining the optical properties of turbid media which potentially allows more accurate recovery of optical coefficients (Gerken and Faris 1999).

A positive temperature coefficient of absorption (α) of $(2.0 \pm 0.02) \times 10^{-4} \text{ cm}^{-1} \text{ K}^{-1}$ at 740 nm and $(2.3 \pm 0.3) \times 10^{-4} \text{ cm}^{-1} \text{ K}^{-1}$ at 840 nm was calculated from the data plotted in Figure 68. At 800 nm as shown in Figure 70, we calculated a temperature coefficient of $(-7 \pm 1) \times 10^{-5} \text{ cm}^{-1} \text{ K}^{-1}$. The near-infrared absorption features arise from overtones and combination bands of the vibrations of the water molecule (Bernath 2002). At 837 nm, the main contribution is a combination of symmetric and asymmetric stretch and bending vibrations. The 739 nm absorption peak is caused by symmetric and asymmetric stretch vibrations. The sensitivity of

water absorption to temperature arises from changes to the strength of the hydrogen bonds and microscopic changes in the structure of the water (Langford et al. 2001).

There is some disagreement in the literature over the precise value of water's near-infrared temperature coefficient. Our results at 740 and 840 nm are in good agreement with those reported by Hollis (2002; Hollis et al. 2001) for water but are 40% higher than the temperature coefficient of water reported by Langford et al. (2001). The temperature coefficient of absorption for Intralipid measured by McGlone et al. (2007) are about 50% lower than our results. At 800 nm, our result is more consistent with the data reported by Langford et al. (2001) and McGlone et al. (2007), underestimating Hollis' observation by 75%.

The temperature coefficient of Intralipid absorption was estimated in 10 nm steps between 710 and 850 nm using the data plotted in Figure 66.

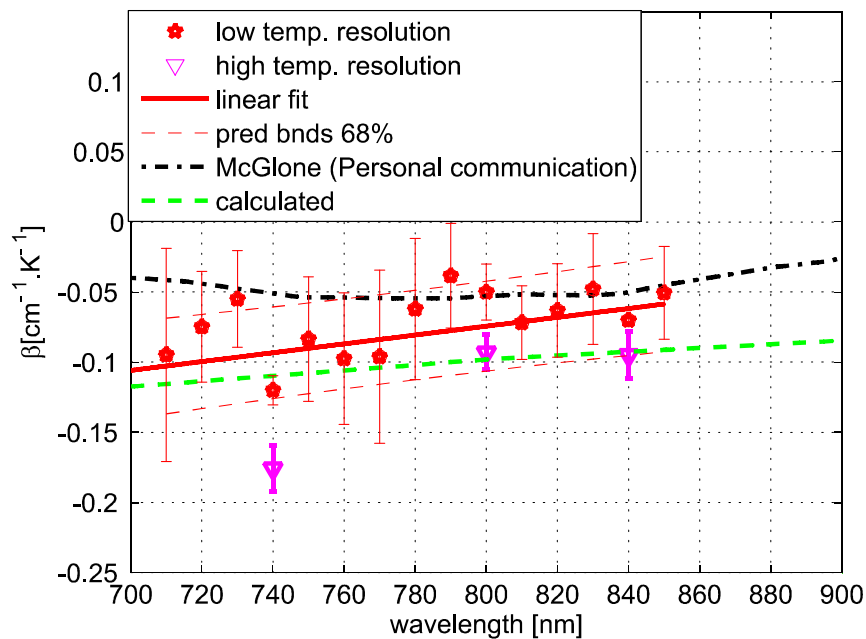


Figure 72 Temperature coefficient for reduced scattering coefficient plotted against wavelength. The red line shows a linear fit to the temperature coefficient.

At most wavelengths, the temperature coefficient was estimated from absorption measured at 22, 30, 35 and 40 °C (squares). At 740, 800 and 840 nm the results, obtained from high temperature resolution measurements, discussed above are plotted (triangles).

The error bars indicate 68% confidence interval of the regression values. Large errors, at 820 nm for example, occur when there is a significant variation in laser power during a measurement. Overall, our results agree in magnitude and spectral shape with values reported in the literature.

The prediction intervals in Figure 68 give an indication of the temperature sensitivity of our set-up. The minimum temperature change observable within the error limits is 4 °C and 6 °C at 740 and 840 nm, respectively. This is probably insufficient for applications requiring precision measurement. Moreover, the presence of other absorbing species, such as haemoglobin, in biological samples will likely demand even greater accuracy. However, we believe the largest source of error lies in the precision of the phase measurements and the short-term stability of the source. We believe more precise temperature measurements can be achieved by including active feedback to control the amplitude of our laser source. This was not possible in the work reported due to financial constraints.

The temperature coefficient of the reduced scattering coefficient (β) was estimated, as for absorption, using linear regression. However, as we found a significant difference in scattering behaviour during heating and cooling, only heating data were used. The results are plotted in Figure 72. At most wavelengths, the temperature coefficient was estimated from reduced scattering measured at 22, 30, 35 and 40°C (squares); at 740, 800 and 840 nm, approximately 10 measurements between 30 and 40°C, as well as 22°C were used (triangles). A linear regression line through the

reduced scattering temperature coefficient shows a general decrease in temperature sensitivity as wavelength increases.

The discrepancy between temperature coefficients from high and low resolution measurements at 740 nm can be largely attributed to fitting errors as there are only three data points in the low resolution and ten data points in high resolution measurements. The effect of hysteresis on this behaviour needs more in depth study.

The scattering coefficient of a turbid media is affected by temperature in two ways. Firstly, as temperature increases the volume of the medium expands, diluting the scattering effect (McGlone et al. 2007). However, more significantly, the refractive index of water also decreases with temperature (Sardar et al. 2006) leading to a greater mismatch between the scattering particles and the absorbing medium. We have modelled the temperature coefficient of the reduced scattering coefficient of Intralipid based on Mie scattering and changes of the refractive index with temperature. We used published particle size distribution data for Intralipid (van Staveren et al. 1991) and assumed a refractive index temperature sensitivity of $3.54 \times 10^{-4} \text{ K}^{-1}$ as that value is typical of the major fatty acids components of soya bean oil and similar derivatives (Castro et al. 2005). Including this result in Figure 72 for comparison (green, dotted) demonstrates agreement with individual measurements experimental error, but suggests in general the temperature coefficient from the experimental data may slightly over estimate that calculated from Mie theory. McGlone et al. measured temperature coefficients for scattering in a 1.2% Intralipid solution by continuous wave measurements. Their data, scaled to 1.8%, is illustrated as well. Within the large uncertainty our measurements agree with theory and other measurements.

6.5 Summary

We have used frequency domain, photon-migration spectroscopy to separately measure absorption and reduced scattering temperature coefficients in a turbid medium for the first time. The optical temperature coefficients of the liquid, tissue simulating phantom, 1.8% Intralipid® were estimated from 710 to 850 nm in the physiologically relevant 30 to 40°C temperature range. At 740, 800 and 840 nm (key wavelengths in the water absorption temperature coefficient), we measured absorption temperature coefficients of $(2.0 \pm 0.02) \times 10^{-4}$, $(-7 \pm 1) \times 10^{-5}$ and $(2.32 \pm 0.03) \times 10^{-4} \text{ cm}^{-1}\text{K}^{-1}$ and reduced scattering temperature coefficients of -0.18 ± 0.02 , -0.09 ± 0.01 and $-0.09 \pm 0.02 \text{ cm}^{-1}\text{K}^{-1}$, respectively. The temperature coefficients observed for absorption closely follow the published results for water, as expected. The temperature coefficients observed for reduced scattering exhibited a general decrease as wavelength increased, consistent with predictions made by Mie theory and literature.

We observed hysteresis behaviour in the reduced scattering measurements made at 740 nm that did not appear to occur at higher wavelengths. The reduced scattering coefficient decreased with temperature, but did not increase again as the solution was cooled until sometime later. This hysteresis did not affect the absorption measurements. This result suggests similar observations of this behaviour reported in extinction measurements are caused by changes in the scattering micelles.

These results suggest temperature measurement, with a precision of $\pm 4 \text{ }^\circ\text{C}$, in turbid media is feasible based on the absorption coefficient's temperature coefficient. However, an improvement in precision will be required for many applications.

CHAPTER 7

CONCLUSION & FUTURE WORK

This thesis explored the relatively new technique: frequency domain photon migration spectroscopy. A brief overview of the theoretical details together with various measurement methods used in research laboratories and real clinical applications is provided. Frequency domain photon migration spectroscopy provides an important spectroscopic technique compared to conventional near-infrared transmission spectroscopy. This method has the capability to independently quantify absorption and scattering in a turbid medium. This makes it particularly useful in medical applications where the absolute quantification of tissue chromophores is required. The frequency domain technique also enjoys greater penetration depth in thick tissue than other photon migration methods making it ideal for applications like in vivo spectroscopy and tissue imaging. Frequency domain spectrometers constructed using laser diode sources are limited to a relatively small range of discrete wavelengths. Wavelength tuneability is beneficial to tissue spectroscopy and imaging as it provides more information about the sample. By externally modulating a wavelength tuneable laser system, the frequency domain spectrometer can be made continuously wavelength tuneable.

A frequency domain spectrometer for the therapeutic window was fabricated by externally modulating a wavelength tuneable Ti: Sapphire laser using an acousto-optic modulator. The acousto-optic modulator was selected after carefully considering diffraction efficiency and modulation bandwidth as these qualities are poor in the case of most commercially available products. A lock-in amplifier together with a low noise avalanche photodiode module constituted the phase sensitive detection system. Initial tests for accuracy and precision indicate that the instrument measures absorption coefficient with an accuracy in the order of 10%. The

precision of absorption and reduced scattering measurements is in the order of 3% and 6% respectively. The frequency domain spectrometer constructed was validated by making optical property measurement in a tissue simulating phantom Intralipid® in the therapeutic window from 700 to 850 nm. Absorption coefficients were measured at a range of concentrations and extrapolated to estimate the concentration of the pure absorber. Comparison with published data for water absorption, the main constituent of Intralipid, demonstrated an accuracy of better than 10% at most of the wavelengths. Measurements of the scattering coefficient were compared with predictions from Mie theory based on independent particle size measurements. A comparison of both measurements agrees within 9%.

To test sensitivity, the frequency domain spectrometer constructed was used to estimate the minute changes in the optical properties of Intralipid with temperature. These measurements indicate a positive temperature coefficient of absorption at 740, 840 nm and a small negative temperature coefficient at 800 nm. These measurements were in excellent agreement with published results. This was the first time these temperature coefficients were measured using the frequency domain technique. We found changes in the absorption coefficient's temperature coefficient could be used to estimate temperature with a precision of ± 4 °C. This is probably not sufficiently precise for most applications of in vivo tissue monitoring, an application that could benefit from further research. We found the reduced scattering coefficient decreased with temperature. We have also demonstrated a hysteresis effect in the scattering coefficient of Intralipid during temperature cycling. Previous work has discussed instabilities in Intralipid with temperature, but this is the first detailed study we are aware of.

Finally the effect of glucose on the optical properties of Intralipid was monitored. The behaviour of glucose in Intralipid seems to be complex regarding absorption and shows no correlation at most of the wavelengths. However measurements at 730 nm show a linear relation between absorption and glucose concentration. This absorption dependence may be analysed by varying temperature of the sample in future for robust glucose sensing.

Future work can be directed to improve the precision and accuracy of the instrumentation thereby making better temperature resolution. This could be achieved by using a source that has very good short term output power stability.

The dependence of reduced scattering coefficient on glucose concentration above and below 760 nm is worth investigating and also the effect of temperature on the optical properties of glucose in a turbid medium. It would also be interesting to see whether any other biological media exhibit hysteresis behaviour for reduced scattering with temperature.

APPENDIX I

Calculation of error in optical properties

The absorption and reduced scattering coefficients were calculated by equations 41 and 42.

To estimate the error in μ_a and μ_s' , we assume that all the error is in measuring the amplitude (m_{ac}) and phase (m_ϕ) slopes. Applying the standard approach for estimating errors for μ_a :

$$\sigma_a = \sqrt{\left(\frac{d\mu_a}{dm_{ac}} \sigma_{ac}\right)^2 + \left(\frac{d\mu_a}{dm_\phi} \sigma_\phi\right)^2} \quad 46$$

Where σ_{ac} and σ_ϕ are the error in amplitude and phase measurements.

Evaluating the derivatives in equation 46 gives:

$$\frac{1}{2} \frac{\omega}{\nu} \left(\frac{-m_\phi}{m_{ac}^2} - \frac{1}{m_\phi} \right) \quad 47$$

$$\frac{1}{2} \frac{\omega}{\nu} \left(\frac{1}{m_{ac}} + \frac{m_{ac}}{m_\phi^2} \right) \quad 48$$

Combining equations 46, 47 and 48 and simplifying gives the error in absorption coefficient as:

$$\sigma_a = \frac{1}{2} \frac{\omega}{\nu} \frac{m_\phi^2 + m_{ac}^2}{m_{ac}^2 - m_\phi^2} \sqrt{\sigma_{ac}^2 m_\phi^2 + \sigma_\phi^2 m_{ac}^2} \quad 49$$

The same analysis for reduced scattering coefficient gives the error as:

$$\sigma_s = \frac{1}{3\mu_a} \sqrt{4(m_{ac}^2 \sigma_{ac}^2 + m_\phi^2 \sigma_\phi^2) + (m_{ac}^2 - m_\phi^2)^2 \left(\frac{\sigma_a}{\mu_a}\right)^2} \quad 50$$

APPENDIX II LabView Codes

LabView code for lock-in Amplifier

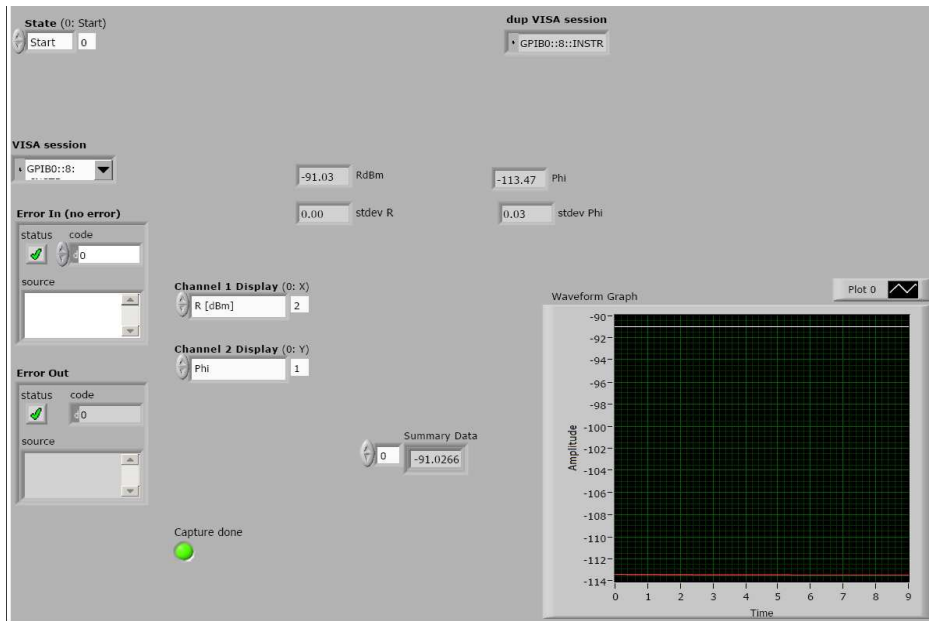


Figure 73 Front panel of LabView program controlling lock-in amplifier.

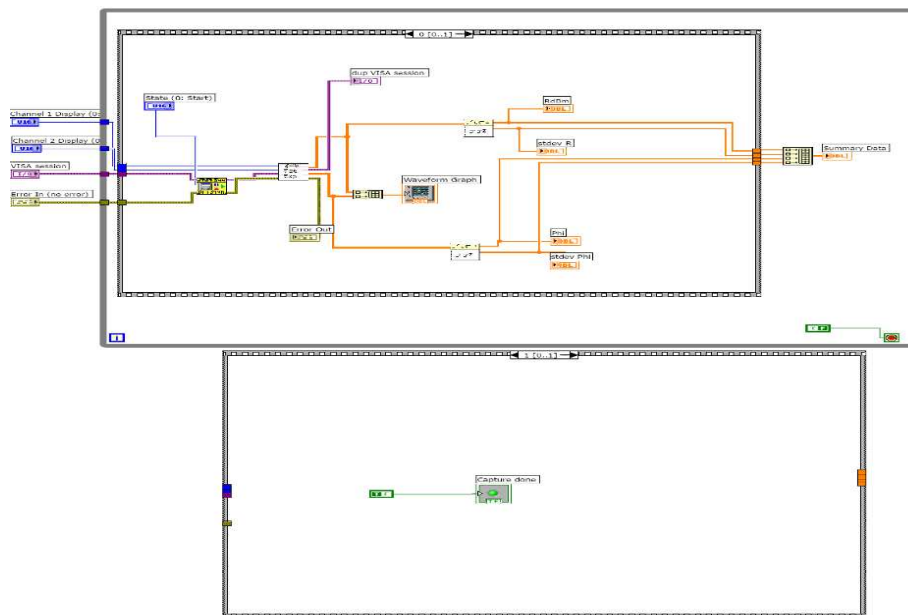


Figure 74 VI corresponding to front panel shown in Figure 73.

LabView front panel - translation stage

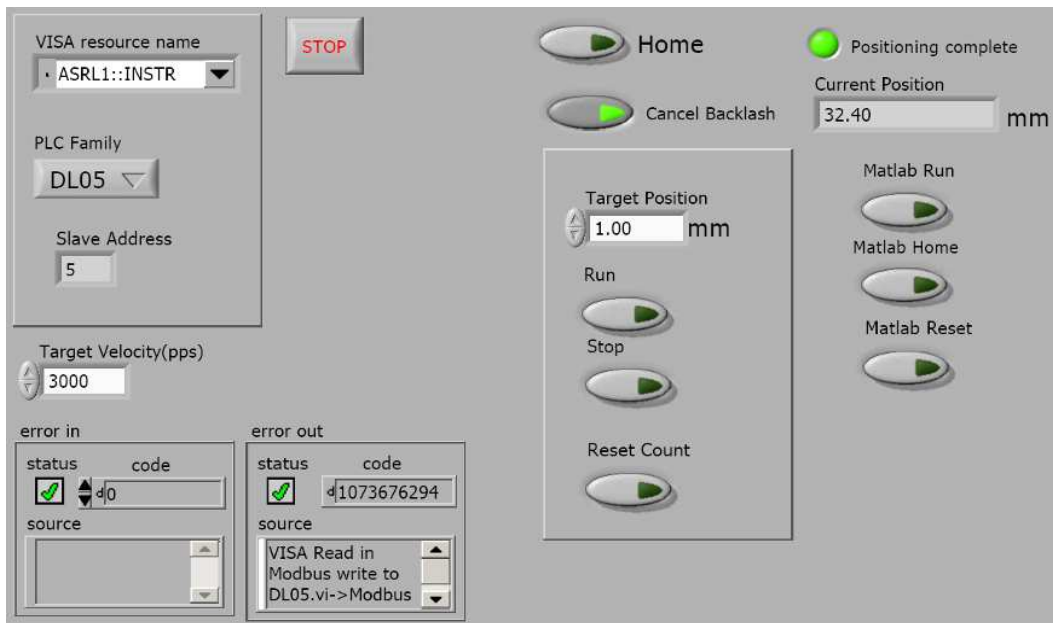


Figure 75 Labview program controlling translation stage.

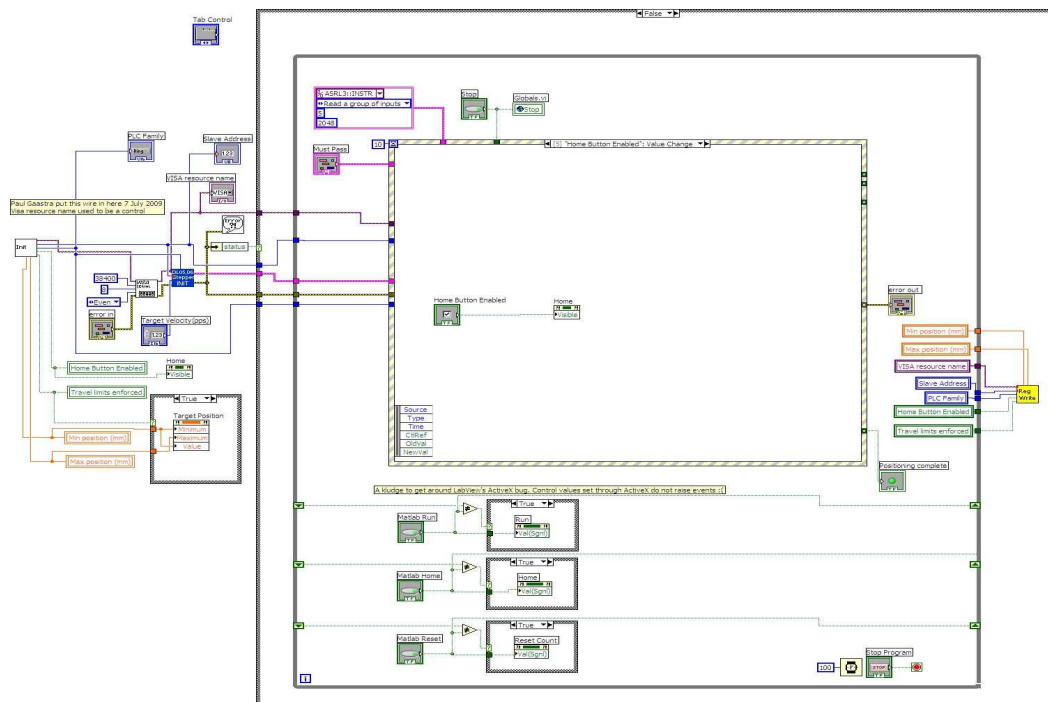


Figure 76 VI corresponding to front panel shown in Figure 75.

Temperature control VI

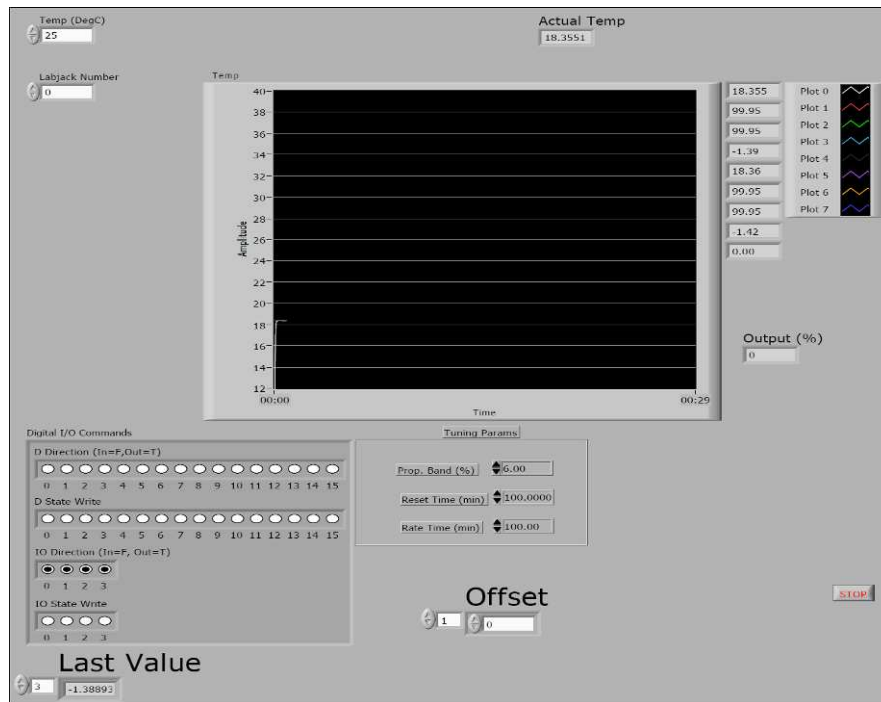


Figure 77 Front panel of LabView program controlling Intralipid temperature.

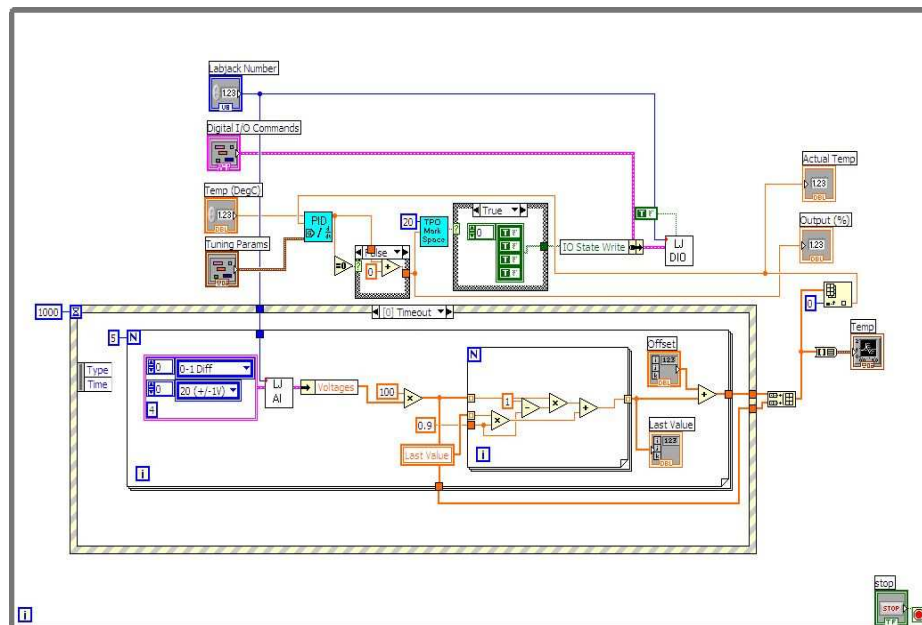


Figure 78 VI corresponding to front panel shown in Figure 77.

MATLAB Codes

Matlab code running the FDPM Spectrometer

```

% Script to run FDPM spectrometer with Lockin Amplifier.
% SETUP INSTRUCTIONS:
% The zero position of the translation stage should be set
% so that zero = home position.
% The Labview stage translator software and Lockin Amplifier
% software should be running before using this script.
% Make sure the paths to the functions we need are available.
addpath('C:\IMOS withLockinAmplifier \LockinAmplifier.vi ');
addpath('C:\Program Files\Stage Translator\Matlab');
% Establish a connection to the labview software that
% controls the translation stage:
hStage = ConnectToTranslationStageController();
% Establish a connection to the labview software that
% gets data from the Lockin Amplifier and Network Analyser.
hLA = OpenLockinAmplifier ();
% Define some experiment parameters
Experiment.Frequency = 50; % Experiment excitation frequency [MHz]
Experiment.InitialSeparation = 10; % Starting separation of optical
probes
Experiment.FinalSeparation = 30; % Final separation of optical
probes
Experiment.NumberOfMeasurements = 26; % Number of measurements to
collect
Experiment.Separations = linspace(Experiment.InitialSeparation,
Experiment.FinalSeparation, Experiment.NumberOfMeasurements);
Experiment.ReplicateMeasurements = 5; % Number of waveforms to
average from LA.
Experiment.RefractiveIndex = 1.33;
SpeedOfLight = 2.9979e10; %[cm/s]
% The translation stage operates to move the fibres closer
together as
% position increases. The following constants will be used to
translate
% between probe separation and stage position.
Stage.A.P = 16; % One position of the translation stage [mm]
Stage.A.S = 44; % Separation of probes at position A.
Stage.B.P = 49; % A second position of the translation stage [mm]
Stage.B.S = 11; % Separation of probes at position B.
% Reserve some storage memory for the data we're going to collect
Experiment.phase =
zeros(Experiment.NumberOfMeasurements, Experiment.ReplicateMeasurem
ents);
Experiment.power =
zeros(Experiment.NumberOfMeasurements, Experiment.ReplicateMeasurem
ents);
% Calculate stage positions from probe separations.
Positions = (Experiment.Separations - Stage.A.S) * (Stage.A.P -
Stage.B.P) / (Stage.A.S - Stage.B.S) + Stage.A.P;
% Collect all the measurements.
for nMeasurement = 1:Experiment.NumberOfMeasurements
% Move the stage to the next position.
disp(['Moving to: ', num2str(Positions(nMeasurement)), '
Separation: ', num2str(Experiment.Separations(nMeasurement))]);
TranslateTo(hStage, Positions(nMeasurement));
pause(3); % Wait for LA to be ready.

```

```

% Collect a measurement from the Lockin Amplifier.
for nRep = 1:Experiment.ReplicateMeasurements
[RdBm,stdevR,Phi,stdevPhi]= GetLockinAmplifierData(hLA);
Experiment.power(nMeasurement, nRep) = RdBm;
Experiment.powersd(nMeasurement, nRep) =stdevR;
Experiment.phase(nMeasurement, nRep) = Phi;
Experiment.phasesd(nMeasurement, nRep) = stdevPhi;
pause(1);
end
figure(1);
plot(Experiment.Separations(1:nMeasurement),
Experiment.power(1:nMeasurement,:), 'x-
',Experiment.Separations(1:nMeasurement),
Experiment.phase(1:nMeasurement,:), 'o-');
xlabel('Probe separation [mm]');
ylabel('Powero[dBm]&Phasex[\circ]');
drawnow;
end
% All finished. Close the connections to labview
CloseLockinAmplifier(hLA);
DisconnectTranslationStageController(hStage);
Experiment.nReject = input('Reject how many points from start?');
% Define some variables.
result.Power =Experiment.power(1:nMeasurement,:);
result.Phase = Experiment.phase(1:nMeasurement,:);
% Assume the power is in dB so calculate linear power.
Experiment.lin_power = 10.^(result.Power(:,1)/20);
nPoints = length(Experiment.lin_power);
% Fit a least-squares line to the power and phase data and
% plot a couple more graphs.
figure(2);
include = (Experiment.nReject+1):nPoints;
power_fit = polyfit(Experiment.Separations(include)/10,
log(Experiment.lin_power(include)) .*
Experiment.Separations(include)/10),1);
yy = polyval(power_fit, Experiment.Separations/10);
plot(Experiment.Separations/10, log(Experiment.lin_power) .*
Experiment.Separations/10,'x', Experiment.Separations/10,
yy,'r',Experiment.Separations(include)/10,
log(Experiment.lin_power(include)) .*
Experiment.Separations(include)/10),'o');
text(0.1,0.9, sprintf('y = %g x + %g', power_fit(1),
power_fit(2)), 'units','normalized');
xlabel('Separation [cm]'); ylabel('log(Power * r)');
figure(3);
phase_fit = polyfit(Experiment.Separations(include)/10, -
result.Phase(include,1)' * pi/180,1);
yy2= polyval(phase_fit, Experiment.Separations/10);
xlabel('Separation [cm]'); ylabel('Phase [radians]');
plot(Experiment.Separations/10, -result.Phase(:,1)' * pi/180,'v',
Experiment.Separations/10, yy2,Experiment.Separations(include)/10,
-result.Phase(include,1)' * pi/180,'o');
text(0.1,0.9, sprintf('y = %g x + %g', phase_fit(1),
phase_fit(2)), 'units','normalized');
% Calculate ua and us.
Experiment.mu_a = (phase_fit(1)/power_fit(1) -
power_fit(1)/phase_fit(1))*pi*Experiment.Frequency*1e6*Experiment.
RefractiveIndex/SpeedOfLight;
Experiment.mu_s_dash = (power_fit(1)^2 -
phase_fit(1)^2)/(3*Experiment.mu_a);

```

```
disp('Result:');
disp(sprintf('mu_a = %g; mu_s_dash = %g', Experiment.mu_a,
Experiment.mu_s_dash));
```

Function connecting the translation stage

```
% Function to open a connection to a running instance
% of the LabView translation stage controller.
function hConnection = ConnectToTranslationStageController()
hConnection.hApp = actxserver('StageTranslator.Application');
hConnection.hController = hConnection.hApp.GetVIREference('Stage
Translator.vi');
```

Function connecting lock-in amplifier

```
% create a connection to labview software that controls
LockinAmplifier
function hLA = OpenLockinAmplifier ()
hLA.hLabView = actxserver('LabView.Application');
hLA.hLockinAmplifier = hLA.hLabView.GetVIREference('C:\IMOS
LockInandAnalyser\LockinAmplifier.vi');
```

Function to move the translation stage

```
% Move the translation stage to a given position.
% Does not return until the stage has completed its
% movement. Position is specified in millimeters from
% the home position.
function TranslateTo(hConnection, Position)
hConnection.hController.SetControlValue('Target Position',
Position);
hConnection.hController.SetControlValue('Matlab Run', 1);
bComplete = 0;
pause(0.4);
while ~bComplete
    pause(0.1)
    bComplete = hConnection.hController.GetControlValue('Positioning
complete');
end
hConnection.hController.SetControlValue('Matlab Run', 0);
```

Function to get data out of lock-in amplifier

```
% Function to get Data from LockinAmplifier VI
function [RdBm,stdevR,Phi,stdevPhi]= GetLockinAmplifierData(hLA)
% Check to see if the data is ready in the labview program
ready = 0;
while ready ==0
    ready = hLA.hLockinAmplifier.GetControlValue('Capture done');
    pause(1);
end
%Get Data from Lockin Amplifier through labview program
data = hLA.hLockinAmplifier.GetControlValue('Summary Data');
RdBm = data(1); % AC Amplitude in dBm
stdevR = data(2); % Standard deviation in amplitude measurements
Phi = data(3); % Phase lag measured in degrees
stdevPhi= data(4); % Standard deviation in phase measurements
hLA.hLockinAmplifier.SetControlValue('Capture done',0);
```

Function to disconnect translation stage

```
% Function to close a connection to a running instance
% of the LabView translation stage controller.
function hConnection =
DisconnectTranslationStageController(hConnection)
release(hConnection.hController);
release(hConnection.hApp);
```

Function to close connection to lock-in amplifier

```
%Close the connection to LockinAmplifier VI
function CloseLockinAmplifier(hLA)
hLA.hLockinAmplifier.release();
hLA.hLabView.release();
```

Code monitoring the temperature effects on optical properties

```
% Script to run IMOS Temperature Measurement with Lockin
Amplifier.
% SETUP INSTRUCTIONS:
% The zero position of the translation stage should be set
% so that zero = home position.
% The Labview stage translator software, Labjack Temperature
Control software and LockinandAnalyser
% software should be running before using this script.
% Make sure the paths to the functions we need are available.
addpath('C:\IMOS withLockinAmplifier\LockinAmplifier.vi ');
addpath('C:\Program Files\Stage Translator\Matlab');
addpath('C:\Program Files\Temp Control.vi');
% Establish a connection to the labview software that
% controls the Labjack Temperature Control.
hConnection = ConnectToLabjackTempControl();
% Establish a connection to the labview software that
% controls the translation stage:
hStage = ConnectToTranslationStageController();
% Establish a connection to the labview software that
% gets data from the Lockin Amplifier and Network Analyser.
hLA = OpenLockinAmplifier ();
TargetTemperature = linspace(20.7,20.9,3);
Separations = linspace(10,30,3);
nReplicates = 5;
nMeasurement = length(Separations);
for i = 1:length(TargetTemperature)
% Change the temperature of the intralipid solution.
disp(sprintf('Setting to %g', TargetTemperature(i)));
ChangeSolutionTemperature(hConnection, TargetTemperature(i));
CurrentTemperature = GetActualTemperature(hConnection);
disp(sprintf('Stabilized at %g', CurrentTemperature));
% Collect measurements...
Data(i).StartTemperature = CurrentTemperature;
Data(i).Result =
CollectMeasurements(hStage,hLA,nMeasurement,nReplicates,Separation
s);
Data(i).EndTemperature = GetActualTemperature(hConnection);
%Calculation
[mu_a(i), mu_rs(i), mu_a_error(i), mu_rs_error(i)] =
calculate(Separations,nMeasurement,Data(i).Result.power,Data(i).Re
sult.phase);
disp('Result:');
```

```
disp(sprintf('mu_a (%d)= %g;mu_rs(%d) = %g ', i,mu_a(i),
i,mu_rs(i)));
disp(sprintf('mu_a_error(%d)= %g; mu_rs_error(%d) = %g',
i,mu_a_error(i),i,mu_rs_error(i)));
mean_temperature(i) = mean([Data(i).StartTemperature,
Data(i).EndTemperature]);
% Save.
save;
end
figure(4);
errorbar(mean_temperature, mu_a, 2*mu_a_error);
figure(5);
errorbar(mean_temperature, mu_rs, 2*mu_rs_error);
% All finished. Close the connections to labview
CloseLockinAmplifier(hLA);
DisconnectTranslationStageController(hStage);
DisconnectTempControl(hConnection);
```

Function connecting the temperature control

```
% Function to open a connection to a running instance
% of the Lajack temperature controller.
function hConnection = ConnnectToLabjackTempControl()
hConnection.hApp = actxserver('LabjackTempControl.Application');
hConnection.hController = hConnection.hApp.GetVIREference('Temp
Control.vi');
```

Function to collect measurements

```
% Function to collect measurement sequence by moving the Optical
fibres.
% hStage is the open connection to the translation stage
% hLNA is the open connection to the labview program that controls
the lockin
% nReplicates is number of replicate measurements to collect at
each separation
% Separations is vector of fibre separations where measurements
are to be collected.
% Results are: experiment phase and power.
% Result.SignalPhase = Phase measured for signal channel.
% Result.SignalPower = Power measured for signal channel.
function [Result] =
CollectMeasurements(hStage,hLA,nMeasurement,nReplicates,Separation
s)
ExperimentFrequency = 50e6; %Frequency of excitation im MHz
ExperimentRefractiveIndex = 1.33; %refractive index of solution
SpeedOfLight = 2.9979e10; % speed of light cm/sec
%Separations = linspace(10,30,2);
% The translation stage operates to move the fibres closer
together as
% position increases. The following constants will be used to
translate
% between probe separation and stage position.
Stage.A.P = 16; % One position of the translation stage [mm]
Stage.A.S = 44; % Separation of probes at position A.
Stage.B.P = 49; % A second position of the translation stage [mm]
Stage.B.S = 11; % Separation of probes at position B.
% Reserve some storage memory for the data we're going to collect
Result.power = zeros(nMeasurement, nReplicates);
Result.phase = zeros(nMeasurement,nReplicates);
```

```

% Result.Separations = zeros(nMeasurement,nReplicates);
% Calculate stage positions from probe separations.
Positions = (Separations - Stage.A.S) * (Stage.A.P -
Stage.B.P)/(Stage.A.S - Stage.B.S) + Stage.A.P;
% Collect all the measurements.
for nCurrentMeasurement = 1:nMeasurement,
    % Move the stage to the next position.
    disp(['Moving to: ', num2str(Positions(nCurrentMeasurement)), '
Separation: ', num2str(Separations(nCurrentMeasurement))]);
    TranslateTo(hStage, Positions(nCurrentMeasurement));
    for nRep = 1:nReplicates
        [RdBm, stdevR, Phi, stdevPhi] = GetLockinAmplifierData(hLA);
        Result.power(nCurrentMeasurement, nRep) = RdBm;
        Result.powersd(nCurrentMeasurement, nRep) = stdevR;
        Result.phase(nCurrentMeasurement, nRep) = Phi;
        Result.phasesd(nCurrentMeasurement, nRep) = stdevPhi;
        figure(1);
        plot(Separations, Result.power, 'x-', Separations, Result.phase, 'o-
');
        xlabel('Probe separation [mm]');
        ylabel('Power [dBm] & Phase [\circ]');
        drawnow;
    end
end
end

```

Function to change solution temperature

```

% Change the temperature of the solution to the target temperature.
Returns
% when the solution has reached the required temperature.
% hConnection: open connection to the labjack. Open with
% ConnectToLabjackTempControl
% Temperature: Desired solution temperature.
function ChangeSolutionTemperature(hConnection, TargetTemperature)
SetTargetTemperature(hConnection, TargetTemperature);
ActualTemperature = 0;
TemperatureHistory = zeros(5,1);
nNextTemperature = 1;
bStable = 0;
while bStable == 0
    pause(1);
    ActualTemperature = GetActualTemperature(hConnection);
    TemperatureHistory(nNextTemperature) = ActualTemperature;
    nNextTemperature = nNextTemperature + 1;
    if (nNextTemperature > length(TemperatureHistory))
        nNextTemperature = 1;
    end
    dT = TemperatureHistory(nNextTemperature) - ActualTemperature;
    disp(sprintf('Target = %g, Actual = %g, dT = %g',
TargetTemperature, ActualTemperature, dT));
    bStable = abs(TemperatureHistory(nNextTemperature) -
ActualTemperature) < 0.2 & abs(TargetTemperature -
ActualTemperature) < 0.5;
end
end

```

Function to calculate optical properties

```

% This function calculate the absorption and scattering
coefficients
% from the data collected by the function "CollectMeasurements".

```

```

%Power = power data in dB
%Phase = phase data in degrees
function [mu_a, mu_rs, mu_a_error, mu_rs_error] =
calculate(Separations,nMeasurement,Power,Phase)
r=repmat(Separations,5,1)./10;
ExperimentFrequency = 50e6;
ExperimentRefractiveIndex = 1.33;
SpeedOfLight=2.9979e10;
Const1=pi*ExperimentFrequency*ExperimentRefractiveIndex/SpeedOfLight;
LinPower = 10.^(Power./20);
PhaseR = Phase.*pi/180;
phase_fit = polyfit(r',-PhaseR,1);
power_fit = polyfit(r',log(r'.*LinPower),1);
Mac =power_fit(1);
Mph =phase_fit(1);
m_ac =power_fit(2);
m_ph =phase_fit(2);
mu_a = (Mph./Mac - Mac./Mph)*Const1;
mu_rs = (Mac.^2 - Mph.^2)./(3*mu_a);
S = sqrt(sum((log(mean(r',2)).*mean(LinPower,2)) - Mac.*mean(r',2) -
m_ac).^2)/(nMeasurement-2));
S1 = sqrt(sum((( -mean(PhaseR,2)- (Mph.*mean(r',2)) -
m_ph)).^2)/(nMeasurement-2));
Sfactor = sqrt(nMeasurement./(nMeasurement.*sum(mean(r',2).^2) -
(sum(mean(r',2)).^2)));
DMac = S.*Sfactor;
DMph = S1.*Sfactor;
% mu_a_error(i) =
Const1*mu_a(i)*(((Mac(i).^2+Mph(i).^2)/(Mac(i).^2-
Mph(i).^2))*sqrt((DMph(i)).^2/(Mph(i).^2)
+(DMac(i)).^2/(Mac(i).^2)));
mu_a_error = Const1 *sqrt(DMac.^2*(Mph/Mac.^2 + 1/Mph).^2 +
DMph.^2*(Mac/Mph.^2 + 1/Mac).^2);
mu_rs_error =(2/(3*mu_a))*sqrt((Mac*DMac)^2 + (Mph* DMph)^2 +
mu_a_error^2*((Mac^2-Mph^2)^2/(4*mu_a^2) - (2/3)*(Mph^2-Mac^2) +
(9/4)*mu_a^2));
% (2/(3*mua)) * sqrt((Mac*EMac)^2 + (Mph*EMph)^2 + Emua^2*
((Mac^2 -Mph^2)^2/(4*mua^2) -2*(Mph^2 -Mac^2)/3 + 9*mua^2/4))
end

```

APPENDIX III

Mathcad-Intralipid® Mie scattering

Most of the Mie code is from (Lompado) and (Fu and Sun 2001). The formalism is based on (van de Hulst 1981) who has provided a summary and procedure for Mie's original work. Fu and Sun (2001) have extended the analysis to allow absorbing media. However, it still only holds for spherical particles.

The results for a non-absorbing medium have been tested for single particles against Wiscombe's example sets and the MieTab program and agree up to at least size parameter 100.

Specific tests with x-size parameter, m real, k imaginary index of scatterer:

x	m	k	Qsca	g
0.1	1.5	0	2.308e-5	1.98e-3
0.165	1.106	0	9.4e-6	4.5e-3
1	1.5	0	0.215	0.199
1.322	1.107	0	0.0229	0.305
4.462	1.106	0	0.425	0.886
10	1.5	0	2.882	0.743
100	1.5	0	2.094	0.818
10	1.5	0.1	1.235	0.922
100	1.5	0.1	1.132	0.95

Required data

Vacuum wavelength:

$$\lambda_0 := 800\text{nm}$$

Concentration of intralipid-10, that is how many mL per L total. (1% corresponds to 0.1% Intralipid)

So here we have a concentration of Intralipid of

$$\text{mL10perL} := \frac{100}{1000}$$

$$\text{mL10perL}10\% = 1\%$$

Speed of light in vacuum:

$$c_0 := 299792458 \frac{\text{m}}{\text{sec}}$$

Properties of the external medium

Water experimental data from Kou et al. (1993). First column Wavelength (micron), second Real Index, third Imaginary Index

Water :=

	1	2	3
1	0.5	1.339	9.243·10 ⁻¹⁰
2	0.505	1.339	1.078·10 ⁻⁹
3	0.51	1.339	...

Find interpolated values at operating wavelength.

$$n_1(\lambda) := \text{linterp}(\text{Water}^{(1)} \cdot 1\mu\text{m}, \text{Water}^{(2)}, \lambda)$$

$$k_1(\lambda) := \text{linterp}(\text{Water}^{(1)} \cdot 1\mu\text{m}, \text{Water}^{(3)}, \lambda)$$

Real part of the refractive index of the medium:

$$n_1(\lambda_0) = 1.326$$

Imaginary part of the refractive index of the medium:

$$k_1(\lambda_0) = 1.251 \times 10^{-7}$$

Relationship between imaginary refractive index and absorption coefficient is:

$$\mu_a = \frac{4 \cdot \pi \cdot k}{\lambda}$$

Properties of the scattering sphere

Refractive indices from van Staveren et al.(1991). Guesstimate at the operating wavelength.

$$n_{\text{soy}} := 1.451$$

$$J_{\text{Cauchy}} := 1.154 \cdot 10^4$$

$$K_{\text{Cauchy}} := -1.132 \cdot 10^9$$

$$n_2(\lambda) := n_{\text{soy}} + \frac{J_{\text{Cauchy}}}{\left(\frac{\lambda}{1\text{nm}}\right)^2} + \frac{K_{\text{Cauchy}}}{\left(\frac{\lambda}{1\text{nm}}\right)^4}$$

Real part of the refractive index of the scatterer:

$$n_2(\lambda_0) = 1.466$$

Imaginary part of the refractive index of the scatterer:

$$k_2 := 0.0$$

Diameters of particles and fraction of total number from (van Staveren et al. 1991). (This will vary from batch to batch and is only a good guesstimate):

$$i := 1..14$$

$$\text{dia}_i := i \cdot 50\text{nm} - 25\text{nm}$$

dia =	1	nmfr :=	0.4673
	25		0.2270
	75		0.0794
	125		0.0787
	175		0.0529
	225		0.0390
	275		0.0216
	325		0.0111
	375		0.0153
	425		3.5×10^{-3}
	475		2.1×10^{-3}
	525		1.4×10^{-3}
	575		0
	625		7×10^{-4}
	675		

$$\sum_i \text{fr}_i = 1$$

The mean diameter of the particles then is:

$$\sum_i (\text{dia}_i \cdot \text{fr}_i) = 97 \text{ nm}$$

Some other derived variables that are required

Radius of the sphere:

$$r_i := \frac{\text{dia}_i}{2}$$

Complex refractive indices:

$$m_1(\lambda) := n_1(\lambda) + i k_1(\lambda)$$

$$m_2(\lambda) := n_2(\lambda) + i k_2$$

$$m_{\text{rel}}(\lambda) := \frac{m_2(\lambda)}{m_1(\lambda)}$$

$$m_{\text{rel}}(\lambda_0) = 1.106 - 1.043i \times 10^{-7}$$

Index of refraction:

Size parameters:

$$q_1(\rho, \lambda) := \frac{2 \cdot \pi \cdot m_1(\lambda)}{\lambda} \cdot \rho$$

$$q_2(\rho, \lambda) := \frac{2 \cdot \pi \cdot m_2(\lambda)}{\lambda} \cdot \rho$$

$$q_1(r, \lambda_0) =$$

	1
1	0.13+1.228i·10 ⁻⁸
2	0.391+3.684i·10 ⁻⁸
3	0.651+6.139i·10 ⁻⁸
4	0.911+8.595i·10 ⁻⁸
5	1.172+1.105i·10 ⁻⁷
6	1.432+1.351i·10 ⁻⁷
7	1.692+1.596i·10 ⁻⁷
8	1.953+1.842i·10 ⁻⁷
9	2.213+2.087i·10 ⁻⁷
10	2.473+2.333i·10 ⁻⁷
11	2.734+2.579i·10 ⁻⁷
12	2.994+2.824i·10 ⁻⁷
13	3.254+3.07i·10 ⁻⁷
14	3.515+3.315i·10 ⁻⁷

$$q_2(r, \lambda_0) =$$

	1
1	0.144
2	0.432
3	0.72
4	1.008
5	1.296
6	1.583
7	1.871
8	2.159
9	2.447
10	2.735
11	3.023
12	3.311
13	3.599
14	3.887

Number of elements to include in sums below [5]

Last term:

$$x_{\text{max}}(\rho, \lambda) := \max(|q_1(\rho, \lambda)|, |q_2(\rho, \lambda)|)$$

$$N_{\text{max}}(\rho, \lambda) := \text{ceil} \left(\left\lfloor x_{\text{max}}(\rho, \lambda) + 4.05 x_{\text{max}}(\rho, \lambda)^{\frac{1}{3}} + 8 \right\rfloor \right)$$

Formulas for the scattering calculations

Following [6] we define in terms of Bessel functions:

$$\psi(n, \rho) := \rho \cdot j_n(n, \rho)$$

$$\psi'(n, \rho) := \frac{d}{d\rho} \psi(n, \rho)$$

$$\zeta(n, \rho) := \rho \cdot (j_n(n, \rho) + i \cdot y_n(n, \rho))$$

$$\zeta'(n, \rho) := \frac{d}{d\rho} \zeta(n, \rho)$$

The Mie coefficients then are:

$$\begin{aligned}
 \text{an}(n, \rho, \lambda) &:= \frac{m_2(\lambda) \cdot \psi'(n, q_1(\rho, \lambda)) \cdot \psi(n, q_2(\rho, \lambda)) - m_1(\lambda) \cdot \psi(n, q_1(\rho, \lambda)) \cdot \psi'(n, q_2(\rho, \lambda))}{m_2(\lambda) \cdot \zeta(n, q_1(\rho, \lambda)) \cdot \psi(n, q_2(\rho, \lambda)) - m_1(\lambda) \cdot \zeta(n, q_1(\rho, \lambda)) \cdot \psi'(n, q_2(\rho, \lambda))} \\
 \text{bn}(n, \rho, \lambda) &:= \frac{m_2(\lambda) \cdot \psi(n, q_1(\rho, \lambda)) \cdot \psi'(n, q_2(\rho, \lambda)) - m_1(\lambda) \cdot \psi'(n, q_1(\rho, \lambda)) \cdot \psi(n, q_2(\rho, \lambda))}{m_2(\lambda) \cdot \zeta(n, q_1(\rho, \lambda)) \cdot \psi'(n, q_2(\rho, \lambda)) - m_1(\lambda) \cdot \zeta(n, q_1(\rho, \lambda)) \cdot \psi(n, q_2(\rho, \lambda))} \\
 \text{cn}(n, \rho, \lambda) &:= \frac{m_2(\lambda) \cdot \zeta(n, q_1(\rho, \lambda)) \cdot \psi'(n, q_1(\rho, \lambda)) - m_2(\lambda) \cdot \zeta(n, q_1(\rho, \lambda)) \cdot \psi(n, q_1(\rho, \lambda))}{m_2(\lambda) \cdot \zeta(n, q_1(\rho, \lambda)) \cdot \psi'(n, q_2(\rho, \lambda)) - m_1(\lambda) \cdot \zeta(n, q_1(\rho, \lambda)) \cdot \psi(n, q_2(\rho, \lambda))} \\
 \text{dn}(n, \rho, \lambda) &:= \frac{m_2(\lambda) \cdot \zeta(n, q_1(\rho, \lambda)) \cdot \psi(n, q_1(\rho, \lambda)) - m_2(\lambda) \cdot \zeta(n, q_1(\rho, \lambda)) \cdot \psi'(n, q_1(\rho, \lambda))}{m_2(\lambda) \cdot \zeta(n, q_1(\rho, \lambda)) \cdot \psi(n, q_2(\rho, \lambda)) - m_1(\lambda) \cdot \zeta(n, q_1(\rho, \lambda)) \cdot \psi'(n, q_2(\rho, \lambda))} \\
 \underline{\underline{A}}(n, \rho, \lambda) &:= \frac{\lambda}{2 \cdot \pi \cdot m_2(\lambda)} \cdot \left[\begin{aligned} &(|\text{cn}(n, \rho, \lambda)|)^2 \cdot \psi(n, q_2(\rho, \lambda)) \cdot \overline{\psi'(n, q_2(\rho, \lambda))} \dots \\ &+ -(|\text{dn}(n, \rho, \lambda)|)^2 \cdot \psi'(n, q_2(\rho, \lambda)) \cdot \overline{\psi(n, q_2(\rho, \lambda))} \end{aligned} \right] \\
 \underline{\underline{B}}(n, \rho, \lambda) &:= \frac{\lambda}{2 \cdot \pi \cdot m_1(\lambda)} \cdot \left[\begin{aligned} &(|\text{an}(n, \rho, \lambda)|)^2 \cdot \zeta(n, q_1(\rho, \lambda)) \cdot \overline{\zeta(n, q_1(\rho, \lambda))} \dots \\ &+ -(|\text{bn}(n, \rho, \lambda)|)^2 \cdot \zeta(n, q_1(\rho, \lambda)) \cdot \overline{\zeta(n, q_1(\rho, \lambda))} \end{aligned} \right]
 \end{aligned}$$

The rate of energy absorbed, scattered or attenuated is

$$W_{\text{abs}}(\rho, \lambda) := \frac{\pi \cdot \lambda}{2 \cdot \pi \cdot c} \cdot \sum_{n=1}^{N_{\text{max}}(\rho, \lambda)} [(2 \cdot n + 1) \cdot \text{Im}(A(n, \rho, \lambda))]$$

$$W_{\text{sca}}(\rho, \lambda) := \frac{\pi \cdot \lambda}{2 \cdot \pi \cdot c} \cdot \sum_{n=1}^{N_{\text{max}}(\rho, \lambda)} [(2 \cdot n + 1) \cdot \text{Im}(B(n, \rho, \lambda))]$$

$$W_{\text{ext}}(\rho, \lambda) := \frac{\pi \cdot \lambda}{2 \cdot \pi \cdot c} \cdot \sum_{n=1}^{N_{\text{max}}(\rho, \lambda)} [(2 \cdot n + 1) \cdot \text{Im}(A(n, \rho, \lambda) + B(n, \rho, \lambda))]$$

When $k_1=0$ the formula for $f()$ misbehaves. We need work around that.

$$\lim_{k \rightarrow 0^+} \left[\frac{\lambda l^2}{8 \cdot \pi \cdot k^2} \cdot \frac{n l}{2 \cdot c_0} \cdot \left[1 + \left(\frac{4 \cdot \pi \cdot \rho \cdot k}{\lambda l} - 1 \right) \exp\left(\frac{4 \cdot \pi \cdot \rho \cdot k}{\lambda l} \right) \right] \right] \rightarrow \frac{\pi \cdot \rho^2 \cdot n l}{2 \cdot c_0}$$

$$I_{\text{lim}}(\rho, \lambda) := \frac{1}{2} \cdot \pi \cdot \rho^2 \cdot \frac{n_1(\lambda)}{c_0}$$

The rate of energy incident on the scatterer is

$$f(\rho, \lambda) := \begin{cases} \frac{\lambda^2}{8 \cdot \pi \cdot k_1(\lambda)^2} \cdot \frac{n_1(\lambda)}{2 \cdot c} \cdot \left[1 + \left(\frac{4 \cdot \pi \cdot \rho \cdot k_1(\lambda)}{\lambda} - 1 \right) \exp\left(\frac{4 \cdot \pi \cdot \rho \cdot k_1(\lambda)}{\lambda} \right) \right] & \text{if } k_1(\lambda) > 10^{-7} \\ I_{\text{lim}}(\rho, \lambda) & \text{otherwise} \end{cases}$$

Some results

The efficiencies and cross sections can be calculated

$$Q_{\text{abs}}(\rho, \lambda) := \frac{W_{\text{abs}}(\rho, \lambda)}{f(\rho, \lambda)}$$

$$Q_{\text{sca}}(\rho, \lambda) := \frac{W_{\text{sca}}(\rho, \lambda)}{f(\rho, \lambda)}$$

$$Q_{\text{ext}}(\rho, \lambda) := \frac{W_{\text{ext}}(\rho, \lambda)}{f(\rho, \lambda)}$$

$$\sigma_{\text{abs}}(\rho, \lambda) := \pi \cdot \rho^2 \cdot Q_{\text{abs}}(\rho, \lambda)$$

$$\sigma_{\text{sca}}(\rho, \lambda) := \pi \cdot \rho^2 \cdot Q_{\text{sca}}(\rho, \lambda)$$

$$\sigma_{\text{ext}}(\rho, \lambda) := \pi \cdot \rho^2 \cdot Q_{\text{ext}}(\rho, \lambda)$$

and the asymmetry factor

$$\text{Norm}(\rho, \lambda) := \frac{2}{N_{\text{max}}(\rho, \lambda) \sum_{n=1}^{N_{\text{max}}(\rho, \lambda)} \left[(2n+1) \left[(|a_n(n, \rho, \lambda)|)^2 + (|b_n(n, \rho, \lambda)|)^2 \right] \right]}$$

$$g(\rho, \lambda) := \text{Norm}(\rho, \lambda) \cdot \left[\sum_{n=1}^{N_{\text{max}}(\rho, \lambda)} \left[\frac{n \cdot (n+2)}{n+1} \text{Re}(a_n(n, \rho, \lambda) \cdot \overline{a_{n+1}(n+1, \rho, \lambda)} + b_n(n, \rho, \lambda) \cdot \overline{b_{n+1}(n+1, \rho, \lambda)}) \dots \right. \right. \\ \left. \left. + \frac{2n+1}{n \cdot (n+1)} \cdot \text{Re}(a_n(n, \rho, \lambda) \cdot \overline{b_n(n, \rho, \lambda)}) \right] \right]$$

$$Q_{\text{abs}}(r_i, \lambda_0) Q_{\text{sca}}(r_i, \lambda_0) = Q_{\text{ext}}(r_i, \lambda_0) = \sigma_{\text{abs}}(r_i, \lambda_0) \sigma_{\text{sca}}(r_i, \lambda_0) =$$

0	4.953·10 ⁻⁶	4.953·10 ⁻⁶	0	μm ²	2.431·10 ⁻⁹	μm ²
0	2.776·10 ⁻⁴	2.776·10 ⁻⁴	0		1.226·10 ⁻⁶	
0	2.045·10 ⁻³	2.045·10 ⁻³	0		2.51·10 ⁻⁵	
0	6.876·10 ⁻³	6.876·10 ⁻³	0		1.654·10 ⁻⁴	
0	0.016	0.016	0		6.186·10 ⁻⁴	
0	0.028	0.028	0		1.665·10 ⁻³	
0	0.043	0.043	0		3.58·10 ⁻³	
0	0.061	0.061	0		6.741·10 ⁻³	
0	0.083	0.083	0		0.012	
0	0.111	0.111	0		0.02	
0	0.143	0.143	0		0.031	
0	0.177	0.177	0		0.046	
0	0.213	0.213	0		0.065	
0	0.253	0.253	0		0.09	

$$\sigma_{\text{ext}}(r_i, \lambda_0) = g(r_i, \lambda_0) =$$

2.431·10 ⁻⁹	μm ²	2.824·10 ⁻³
1.226·10 ⁻⁶		0.025
2.51·10 ⁻⁵		0.071
1.654·10 ⁻⁴		0.141
6.186·10 ⁻⁴		0.238
1.665·10 ⁻³		0.359
3.58·10 ⁻³		0.495
6.741·10 ⁻³		0.62
0.012		0.704
0.02		0.744
0.031		0.764
0.046		0.787
0.065		0.816
0.09		0.842

We now need to consider the effect of the different sized particles. We calculate the volume fraction for 100% of Intralipid-10. The data is from Jacques (1998) which is close to our own:

	Jacques		[our numbers]
soybean oil	50 g	53.94 mL	100g
lecithin	6 g	5.82 mL	12g
glycerin	11.25 g	8.92 mL	22g
water	430.5 g	431.33 mL	
TOTAL	497.75 g	500 mL	vol := $\frac{53.94\text{mL} + 5.82\text{mL}}{500\text{mL}}$

The number density of the particles can be estimated (van Staveren et al. 1991):

$$N_0 := \frac{\text{mL10perLvol}}{\sum_i \left[\frac{4}{3} \pi \cdot (r_i)^3 \cdot \text{fr}_i \right]}$$

$$N_0 = 3.9662 \times 10^{12} \text{ cm}^{-3}$$

The scattering coefficient is:

$$\mu_s(\lambda) := N_0 \cdot \left[\sum_i \left(\sigma_{\text{sca}}(r_i, \lambda) \cdot \text{fr}_i \right) \right]$$

$$\mu_s(\lambda_0) = 2.8076 \text{ mm}^{-1}$$

The anisotropy [2]:

$$g(\lambda) := \frac{\sum_i \left(g(r_i, \lambda) \cdot \sigma_{\text{sca}}(r_i, \lambda) \cdot \text{fr}_i \right)}{\sum_i \left(\sigma_{\text{sca}}(r_i, \lambda) \cdot \text{fr}_i \right)}$$

$$g(\lambda_0) = 0.636$$

The reduced scattering coefficient:

$$\mu'_s(\lambda) := (1 - g(\lambda)) \cdot \mu_s(\lambda)$$

$$\mu'_s(\lambda_0) = 1.022 \text{ mm}^{-1}$$

REFERENCES

- Alford, K. and Y. Wickramasinghe. 2000. Phase-amplitude crosstalk in intensity modulated near infrared spectroscopy. *Review of Scientific Instruments* 71(5) 2191-5.
- Andersson-Engels, S., R. Berg, A. Persson and S. Svanberg. 1993. Multispectral tissue characterization with time-resolved detection of diffusely scattered white light. *Optics Letters* 18(20) 1697-9.
- Aronson, R. 1995. Boundary conditions for diffusion of light. *Journal of the Optical Society of America A* 12(11) 2532-9.
- Aronson, R. and N. Corngold. 1999. Photon diffusion coefficient in an absorbing medium. *Journal of the Optical Society of America A* 16(5) 1066-71.
- Arridge, S. R., M. Cope and D. T. Delpy. 1992. The theoretical basis for the determination of optical pathlengths in tissue: temporal and frequency analysis. *Physics in Medicine and Biology* 37(7) 1531-60.
- Arridge, S. R., M. Schweiger, M. Hiraoka and D. T. Delpy. 1993. A finite element approach for modelling photon transport in tissue. *Medical Physics* 20(2) 299-309.
- Arridge, S. R. and M. Schweiger. 1995. Photon measurement density functions. Part 2: Finite-element-method calculations. *Applied Optics* 34 8026-37.
- Baltes, C. and G. W. Faris. 2009. Frequency domain measurements on turbid media with strong absorption using the PN approximation. *Applied Optics* 48(16) 2991-3000.
- Bassani, M., F. Martelli, G. Zaccanti and D. Contini. 1997. Independence of the diffusion coefficient from absorption: experimental and numerical evidence. *Optics Letters* 22(12) 853-5.
- Bays, R., G. Wagnières, D. Robert, D. Braichotte, J.-F. Savary, P. Monnier and H. van den Bergh. 1996. Clinical determination of tissue optical properties by endoscopic spatially resolved reflectometry. *Applied Optics* 35(10) 1756-66.
- Becker and Hickl. 2000. How (and why not) to Amplify PMT Signals. Berlin: Becker & Hickl GmbH.
- Becker, W., A. Bergmann, G. Biscotti and A. Rück. 2004. Advanced time-correlated single photon counting technique for spectroscopy and imaging in biomedical systems. *Proceedings of SPIE* 5340 1-9.
- Begley, T. H., E. Lanza, K. H. Norris and W. R. Hruschka. 1984. Determination of sodium chloride in meat by near-infrared diffuse reflectance spectroscopy. *Journal of Agricultural and Food Chemistry* 32 984-7.

- Berg, B. A. 1998. Introduction to Multicanonical Monte Carlo Simulations. *Lecture given at the Fields Institute Workshop on Monte Carlo Methods* 1-24.
- Berg, B. A. and T. Neuhaus. 1992. Multicanonical ensemble: A new approach to simulate first-order phase transitions. *Physical Review Letters* 68(1) 9.
- Berg, R., S. Andersson-Engels, O. Jarlman and S. Svanberg. 1996. Time-gated viewing studies on tissue like phantoms. *Applied Optics* 35(19) 3432-40.
- Bernath, P. F. 2002. The spectroscopy of water vapour: Experiment, theory and applications. *Physical Chemistry and Chemical Physics* 4(3) 1501-9.
- Bevilacqua, F., A. J. Berger, A. E. Cerussi, D. Jakubowski and B. J. Tromberg. 2000. Broadband absorption spectroscopy in turbid media by combined frequency-domain and steady-state methods. *Applied Optics* 39(34) 6498-507.
- Bevilacqua, F., D. Piguet, P. Marquet, J. D. Gross, B. J. Tromberg and C. Depeursinge. 1999. In Vivo Local Determination of Tissue Optical Properties: Applications to Human Brain. *Applied Optics* 38(22) 4939-50.
- Bilenca, A., A. Desjardins, B. Bouma and G. Tearney. 2005. Multicanonical Monte-Carlo simulations of light propagation in biological media. *Optics Express* 13(24) 9822-33.
- Binzoni, T., T. S. Leung, R. Giust, D. R. fenacht and A. H. Gandjbakhche. 2008. Light transport in tissue by 3D Monte Carlo: Influence of boundary voxelization. *Computer Methods and Programs in Biomedicine* 89 14-23.
- Boas, D. A., M. A. O'Leary, B. Chance and A. G. Yodh. 1994. Scattering of diffuse photon density waves by spherical inhomogeneities within turbid media: Analytic solution and applications. *Proceedings of National Academy of Science USA* 91 4887-91.
- Bondani, M., D. Redaelli, A. Spinelli, A. Andreoni, G. Roberti, P. Riccio, R. Liuzzi and I. Rech. 2003. Photon time-of-flight distributions through turbid media directly measured with single-photon avalanche diodes. *Journal of the Optical Society of America A* 20(11) 2383-8.
- Bonner, R. F., R. Nossal, S. Havlin and G. H. Weiss. 1987. Model for photon migration in turbid biological media. *Journal of the Optical Society of America A* 4(3) 423-32.
- Bonney, R., O. Zehl, J. Rosenbaum and M. G. Price. 1984. Performance and optical characterization of efficient wideband gallium phosphide Bragg cells. *Applied Optics* 23(16) 2778-83.
- Bozkurt, A., A. Rosen, H. Rosen and B. Onaral. 2005. A portable near infrared spectroscopy system for bedside monitoring of newborn brain. *BioMedical Engineering OnLine* 4(1) 29.

-
- Brewster, M. Q. and Y. Yamada. 1995. Optical properties of thick, turbid media from picosecond time-resolved light scattering measurements. *International Journal of Heat and Mass Transfer* 38(14) 2569-81.
- Buiteveld, H., J. M. H. Hakvoort and M. Donze. 1994. The optical properties of pure water. *Proceedings of SPIE* 2258 174-83.
- Cai, W., M. Xu, M. Lax and R. R. Alfano. 2002. Diffusion coefficient depends on time, not on absorption. *Optics Letters* 27(9) 731-3.
- Calba, C., L. Méès, C. Rozé and T. Girasole. 2008. Ultrashort pulse propagation through a strongly scattering medium: simulation and experiments. *Journal of the Optical Society of America A* 25(7) 1541-50.
- Castro, M. P. P., A. A. Andrade, R. W. A. Franco, P. C. M. L. Miranda, M. Sthel, H. Vargas, R. Constantino and M. L. Baesso. 2005. Thermal properties measurements in biodiesel oils using photothermal techniques. *Chemical Physics Letters* 411(1) 18-22.
- Cerussi, A. E., A. J. Berger, F. Bevilacqua, N. Shah, D. Jakubowski, J. Butler, R. F. Holcombe and B. J. Tromberg. 2001. Sources of Absorption and Scattering Contrast for Near-Infrared Optical Mammography *Academic Radiology* 8(3) 211-8.
- Chalut, K. J., M. G. Giacomelli and A. Wax. 2008. Application of Mie theory to assess structure of spheroidal scattering in backscattering geometries. *Journal of the Optical Society of America A* 25(8) 1866-74.
- Chance, B. 1991. Optical Method *Annual Review of Biophysics and Biophysical Chemistry* 20 1-30.
- Chance, B., S. Nioka, J. Kent, K. McCully, M. Fountain, R. Greenfeld and G. Holtom. 1988. Time-resolved spectroscopy of hemoglobin and myoglobin in resting and ischemic muscle. *Analytical Biochemistry* 174(2) 698-707.
- Chandrasekhar, S. 1960. *Radiative Transfer*. New York: Dover Publications.
- Chang, I. C. 1976. Acoustooptic devices and applications. *IEEE Transactions on sonics and ultrasonics* su-23(1) 2-22.
- Chen, C., J. Q. Lu, H. Ding, K. M. Jacobs, Y. Du and X.-H. Hu. 2006. A primary method for determination of optical parameters of turbid samples and application to intralipid between 550 and 1630nm. *Optics Express* 14(16) 7420-35.
- Cheong, W. F., S. A. Prahl and A. J. Welch. 1990. A review of the optical properties of biological tissues. *IEEE Journal of Quantum Electronics* 26(12) 2166-85.

- Chernomordik, V., D. Hattery, A. H. Gandjbakhche, A. Pifferi, P. Taroni, A. Torricelli, G. Valentini and R. Cubeddu. 2000. Quantification by random walk of the optical parameters of nonlocalized abnormalities embedded within tissuelike phantoms. *Optics Letters* 25(13) 951-3.
- Chernomordik, V., D. W. Hattery, D. Grosenick, H. Wabnitz, H. Rinneberg, K. T. Moesta, P. M. Schlag and A. Gandjbakhche. 2002. Quantification of optical properties of a breast tumor using random walk theory. *Journal of Biomedical Optics* 7(1) 80-7.
- Cletus, B., R. Künnemeyer, P. Martinsen and A. McGlone. 2010. Temperature dependent optical properties of Intralipid measured with frequency domain photon migration spectroscopy. *Journal of Biomedical Optics* 15(1) in press.
- Cletus, B., R. Künnemeyer, P. Martinsen, A. McGlone and R. Jordan. 2009. Characterizing liquid turbid media by frequency-domain photon migration spectroscopy. *Journal of Biomedical Optics* 14(2) 024041-7.
- Collins, J. R. 1925. Change In the infra-red absorption spectrum of water with temperature. *Physical Review* 26(6) 771-9.
- Contini, D., A. Torricelli, A. Pifferi, L. Spinelli, F. Paglia and R. Cubeddu. 2006. Multi-channel time-resolved system for functional near infrared spectroscopy. *Optics Express* 14(12) 5418-32.
- Coquoz, O., L. O. Svaasand and B. J. Tromberg. 2001. Optical property measurements of turbid media in a small-volume cuvette with frequency-domain photon migration. *Applied Optics* 40(34) 6281-91.
- Cova, S., M. Ghioni, A. Lacaita, C. Samori and F. Zappa. 1996. Avalanche photodiodes and quenching circuits for single-photon detection. *Applied Optics* 35(12) 1956-76.
- Cubeddu, R., A. Pifferi, P. Taroni, A. Torricelli and G. Valentini. 1997. A solid tissue phantom for photon migration studies. *Physics in Medicine and Biology* 42 1971-9.
- Dam, J. S., C. B. Pedersen, T. Dalgaard, P. E. Fabricius, P. Aruna and S. Andersson-Engels. 2001. Fiber-optic probe for noninvasive real-time determination of tissue optical properties at multiple wavelengths. *Applied Optics* 40(7) 1155-64.
- Debye, P. and F. W. Sears. 1932. On the scattering of light by supersonic waves. *Proceedings of National Academy of Science USA* 18 409-14.
- Delpy, D. T. and M. Cope. 1997. Quantification in tissue near-infrared spectroscopy. *Philosophical Transactions of Royal Society of London B* 352 649-59.

-
- Delpy, D. T., M. Cope, P. vander Zee, S. Arridge, S. Wray and J. Wyatt. 1988. Estimation of optical pathlength through tissue from direct time of flight measurement. *Physics in Medicine and Biology* 33(12) 1433-42.
- Dick, V. P. 1998. Applicability limits of Beer's law for dispersion media with a high concentration of particles. *Applied Optics* 37(21) 4998-5004.
- Downing, H. D. and D. Williams. 1975. Optical constants of water in the infrared. *Journal of Geophysical Research* 80 1656-61
- Ducros, N., A. d. Silva, J.-M. Dinten and F. Peyrin. 2008. Approximations of the measurable quantity in diffuse optical problems: theoretical analysis of model deviations. *Journal of the Optical Society of America A* 25(5) 1174-80.
- Durduran, T., A. G. Yodh, B. Chance and D. A. Boas. 1997. Does the photon-diffusion coefficient depend on absorption? *Journal of the Optical Society of America A* 14(12) 3358-65.
- Emmons, R. B. 1967. Avalanche-Photodiode Frequency Response. *Journal of Applied Physics* 38(9) 3705-14.
- Fantini, S., M. A. Franceschini-Fantini, J. S. Maier, S. A. Walker, B. Barbieri and E. Gratton. 1995. Frequency-domain multichannel optical detector for noninvasive tissue spectroscopy and aximetry. *Optical Engineering* 34(1) 32-42.
- Fantini, S., M. A. Franceschini, J. B. Fishkin, B. Barbieri and E. Gratton. 1994a. Quantitative determination of the absorption spectra of chromophores in strongly scattering media: a light-emitting-diode based technique. *Applied Optics* 33(22) 5204-13.
- Fantini, S., M. A. Franceschini and E. Gratton. 1994b. Semi-infinite-geometry boundary problem for light migration in highly scattering media: a frequency-domain study in the diffusion approximation. *Journal of the Optical Society of America B* 11(10) 2128-38.
- Farrell, T. J., M. S. Patterson and B. Wilson. 1992. A diffusion theory model of spatially resolved, steady-state diffuse reflectance for the noninvasive determination of tissue optical properties in vivo. *Medical Physics* 19(4) 879-88.
- Feddersen, B. A., D. W. Piston and E. Gratton. 1989. Digital parallel acquisition in frequency domain fluorimetry. *Review of Scientific Instruments* 60(9) 2929.
- Fishkin, J. B., S. Fantini, M. J. vandeVen and E. Gratton. 1996. Gigahertz photon density waves in a turbid medium: Theory and experiments. *Physical Review E* 53(3) 2307-19.
- Fishkin, J. B. and E. Gratton. 1993. Propagation of photon-density waves in strongly scattering media containing an absorbing semi-infinite plane

- bounded by a straight edge. *Journal of the the Optical Society of America A* 10(1) 127-40.
- Fishkin, J. B., E. Gratton, M. J. vandeVen and W. W. Mantulin. 1991. Diffusion of intensity modulated near-infrared light in turbid media. *Proceedings of SPIE* 1431 122-35
- Flock, S. T., S. L. Jacques, B. C. Wilson, W. M. Star and M. J. van Gemert. 1992. Optical properties of Intralipid: a phantom medium for light propagation studies. *Lasers in Surgery and Medicine* 12(5) 510-9.
- Franken, P. A., A. E. Hill, C. W. Peters and G. Weinreich. 1961. Generation of Optical Harmonics. *Physical Review Letters* 7(4) 118.
- Fu, Q. and W. Sun. 2001. Mie Theory for Light Scattering by a Spherical Particle in an Absorbing Medium. *Applied Optics* 40(9) 1354-61.
- Furutsu, K. and Y. Yamada. 1994. Diffusion approximation for a dissipative random medium and the applications. *Physical Review E* 50(5) 3634.
- Gandhjbakhche, A. H., G. H. Weiss, F. F. Bonner and R. Nossal. 1995. Random walk and diffusion like models of photon migration in turbid media In *Progress in Optics*, ed. E. Wolf, 333-401. Amsterdam: Elsevier.
- Gerken, M. and G. W. Faris. 1999. High-precision frequency-domain measurements of the optical properties of turbid media. *Optics Express* 24(14) 930-2.
- Giangiaco, R. 2006. Study of water-sugar interactions at increasing sugar concentration by NIR spectroscopy. *Food Chemistry* 96 371-9.
- Gibson, A. P., J. C. Hebden and S. R. Arridge. 2005. Recent advances in diffuse optical imaging. *Physics in Medicine and Biology* 50(5) R1-R43.
- Giusto, A., R. Saija, M. A. Iati, P. Denti, F. Borghese and O. I. Sindoni. 2003. Optical properties of high-density dispersions of particles: application to intralipid solutions. *Applied Optics* 42(21) 4375-9.
- Gopal, V., S. Mujumdar, H. Ramachandran and A. K. Sood. 1999. Imaging in turbid media using quasi-ballistic photons. *Optics Communications* 170(4-6) 331-45.
- Graaff, R. and J. J. T. Bosch. 2000. Diffusion coefficient in photon diffusion theory. *Optics Letters* 25(1) 43-5.
- Graaff, R., M. H. Koelink, F. F. M. de Mul, W. G. Zijistra, A. C. M. Dassel and J. G. Aarnoudse. 1993. Condensed Monte Carlo simulations for the description of light transport. *Applied Optics* 32(4) 426-34.

-
- Gratton, E. and M. Limkeman. 1983. A continuously variable frequency cross-correlation phase fluorometer with picosecond resolution. *Biophysical Journal* 44 315-24.
- Hakamata, T. 2006. Photomultiplier Tubes - Basics and applications: Hamamatu Photonics K K (Electron tube division).
- Hale, G. M. and M. R. Querry. 1973. Optical Constants of Water in the 200-nm to 200- μ m Wavelength Region. *Applied Optics* 12(3) 555-63.
- Haskell, R. C., L. O. Svaasand, T. T. Tsay, T. C. Feng, M. S. McAdams and B. J. Tromberg. 1994. Boundary conditions for the diffusion equation in radiative transfer. *Journal of the Optical Society of America A* 11(10) 2727-41.
- Hirshburg, J., B. Choi, J. S. Nelson and A. T. Yeh. 2007. Correlation between Collagen Solubility and Skin Optical Clearing Using Sugars. *Lasers in Surgery and Medicine* 39 140-4.
- Hollis, V. S. 2002. Non-invasive monitoring of brain tissue by near-infrared spectroscopy. *PhD Thesis* University College London.
- Hollis, V. S., T. Binzoni and D. T. Delpy. 2001. Non-invasive monitoring of brain tissue temperature by near-infrared spectroscopy. *Proceedings of SPIE* 4250 470-81.
- Hoshi, Y. 2005. Functional near-infrared spectroscopy: potential and limitations in neuro imaging studies. *International Review of Neurobiology* 66 236-66.
- Huang, D., E. A. Swanson, C. P. Lin, J. S. Schuman, W. G. Stinson, W. Chang, M. R. Hee, T. Flotte, K. Gregory, C. A. Puliafito, et al. 1991. Optical coherence tomography. *Science* 254 1178-81.
- Huang, H., H. Yu, H. Xu and Y. Ying. 2008. Near infrared spectroscopy for on/in-line monitoring of quality in foods and beverages: A review. *Journal of Food Engineering* 87(1) 303-13.
- Huang, Y. 2004. Characterization of dense suspensions using frequency domain photon migration, PhD Thesis, Texas A&M University, Texas.
- Hull, E. L., M. G. Nichols and T. H. Foster. 1998. Quantitative broadband near-infrared spectroscopy of tissue-simulating phantoms containing erythrocytes. *Physics in Medicine and Biology* 43 3381-404.
- Hulvershorn, J., L. Bloy, J. S. Leigh and M. A. Elliott. 2003. Continuous wave optical spectroscopic system for use in magnetic resonance imaging scanners for the measurement of changes in hemoglobin oxygenation states in humans. *Review of Scientific Instruments* 74(9) 4150-7.
- Imagent™. Functional Brain Imaging System. (accessed <http://www.iss.com/products/imagent/index.html> June 2009).

- Ishimaru, A. 1978a. Diffusion of a pulse in densely distributed scatterers. *Journal of Optical Society of America* 68 1045-50.
- Ishimaru, A. 1978b. *Wave Propagation and Scattering in Random Media. Vol 1: Single Scattering and Transport Theory* New York: Academic Press
- ISOMET Corporation. All about Bragg angle errors in AO modulators & deflectors. In *Application Note IM1022*: ISOMET Corporation, www.ISOMET.com
- Iwata, T., T. Inoue and T. Araki. 2004. Pseudo-Lock-in Light Detection Method for a Sinusoidally-Gain-Modulated Photomultiplier Tube. *Optical Review* 11(1) 19-23.
- Jacques, S. L. 1998. Optical properties of "Intralipid®", an aqueous suspension of lipid droplets. (accessed <http://omlc.ogi.edu/spectra/intralipid/index.html> 2008).
- Jacques, S. L. 2008. Modelling tissue optics using Monte Carlo modelling: A tutorial. *Proceedings of SPIE* 6854 1-9.
- Jacques, S. L., C. A. Alter and S. A. Prahl. 1987. Angular dependence of HeNe laser light scattering by human dermis. *Lasers in the Life Sciences* 1 309-33.
- Jacques, S. L., A. Gutsche, J. Schwartz, L. Wang and F. K. Tittel. 1993. Video reflectometry to extract optical properties of tissue in vivo *SPIE Institute Series ISII* 211-26.
- Jacques, S. L. and B. W. Pogue. 2008. Tutorial on diffuse light transport. *Journal of Biomedical Optics* 13(4) 041302-1-19.
- Jeffrey, J. K., A. K. Katherine and H. B. Clyde. 1995. Tissue temperature by near-infrared spectroscopy. *Proceedings of SPIE* 2389 818-28.
- Jiang, H., J. Pierce, J. Kao and E. Sevick-Muraca. 1997. Measurement of particle-size distribution and volume fraction in concentrated suspensions with photon migration techniques. *Applied Optics* 36(15) 3310-8.
- Jobsis-vanderVliet, F. F. 1999. Discovery of the Near-Infrared Window into the Body and the Early Development of Near-Infrared Spectroscopy. *Journal of Biomedical Optics* 4(4) 392-6.
- Joseph, J. H., W. J. Wiscombe and J. A. Weinman. 1976. The Delta-Eddington Approximation for Radiative Flux Transfer. *Journal of the Atmospheric Sciences* 33(12) 2452-9.
- Kakuta, N., H. Arimoto, H. Momoki, F. Li and Y. Yamada. 2008. Temperature measurements of turbid aqueous solutions using near-infrared spectroscopy. *Applied Optics* 47(13) 2227-33.

-
- Kaltenbach, J. P. and M. Kaschke. 1993. Frequency and Time-Domain Modelling of Light Transport in Random Media. In *Medical optical tomography : functional imaging and monitoring* ed. G. J. Muller, 65-86. Bellingham: SPIE Optical Engineering Press.
- Karagiannes, J. L., Z. Zhang, B. Grossweiner and L. I. Grossweiner. 1989. Applications of the 1-D diffusion approximation to the optics of tissues and tissue phantoms. *Applied Optics* 28(12) 2311-7.
- Kawano, S., T. Fujiwara and M. Iwamoto. 1993. Nondestructive determination of sugar content in satsuma mandarin using near infrared (NIR) transmittance. *Journal of the Japanese Society for Horticultural Science* 62(465-470).
- Khalil, O. S. 1999. Spectroscopic and Clinical Aspects of Noninvasive Glucose Measurements. *Clinical Chemistry* 45(2) 165-77.
- Kienle, A., L. Lilge, M. S. Patterson, R. Hibst, R. Steiner and B. C. Wilson. 1996. Spatially resolved absolute diffuse reflectance measurements for noninvasive determination of the optical scattering and absorption coefficients of biological tissue. *Applied Optics* 35(13) 2304-14.
- Kienle, A. and M. S. Patterson. 1996. Determination of the optical properties of turbid media from a single Monte Carlo simulation. *Physics in Medicine and Biology* 41(10) 2221-7.
- Knight, K. L. and D. O. Draper. 2008. *Therapeutic Modalities: The Art and Science*. Baltimore, MD Lippincott Williams & Wilkins
- Kocsis, L., P. Herman and A. Eke. 2006. The modified Beer–Lambert law revisited. *Physics in Medicine and Biology* 51(5) N91-N8.
- Kohl, M., M. Cope, M. Essenpreis and D. Böcker. 1994. Influence of glucose concentration on light scattering in tissue-simulating phantoms. *Optics Letters* 19(24) 2170-2.
- Korpel, A. 1988. *Acousto-Optics* New York: Marcel Dekker
- Kou, L., D. Labrie and P. Chylek. 1993. Refractive indices of water and ice in the 0.65- to 2.5- μm spectral range. *Applied Optics* 32 3531-40.
- Kubelka, P. 1948. New contribution to the optics of intensely light-scattering materials. Part I. *Journal of the Optical Society of America* 38 448-57.
- Kubelka, P. and F. Munk. 1931. Ein Beitrag zur Optik der Farbanstriche. *Z. Tech. Physik* 12 593-601.
- Künnemeyer, R. 2008. Mathcad-Intralipd® Mie scattering. *personal communication* 1-14.

- Langford, V. S., A. J. McKinley and T. I. Quickenden. 2001. Temperature Dependence of the Visible-Near-Infrared Absorption Spectrum of Liquid Water. *Journal of Physical Chemistry* 105(39) 8916-21.
- Lapidus, L. and G. F. Pinder. 1999. *Numerical solutions of partial differential equations in science and engineering*. New York: Wiley Inter-Science
- Laufer, J., R. Simpson, M. Kohl, M. Essenpreis and M. Cope. 1998. Effect of temperature on the optical properties of ex vivo human dermis and subdermis. *Physics in Medicine and Biology* 43(9) 2479-89.
- Liu, F., K. M. Yoo and R. R. Alfano. 1993. Should the photon flux or the photon density be used to describe the temporal profiles of scattered ultra short laser pulses in random media? *Optics Letters* 18(6) 432-4.
- Lompado. Mathematica code. *University of Alabama* Dept. of Physics(LompadoA@email.uah.edu) Huntsville, AL.
- Lucas, R. and P. Biquard. 1932. Proprietes optiques des milieux solides et liquides soumis aux vibrations elastiques ultrasonores. *Journal Physics (Paris)* 71 464-77.
- Madsen, S. J., E. R. Anderson, R. C. Haskell and B. J. Tromberg. 1994. Portable, high-bandwidth frequency-domain photon migration instrument for tissue spectroscopy. *Optics Letters* 19(23) 1934-6.
- Maier, J. S., S. A. Walker, S. Fantini, M. A. Franceschini and E. Gratton. 1994. Possible correlation between blood glucose concentration and the reduced scattering coefficient of tissues in the near infrared. *Optics Letters* 19(24) 2062-4.
- Martelli, F., M. Bassani, L. Alianelli, L. Zangheri and G. Zaccanti. 2000. Accuracy of the diffusion equation to describe photon migration through an infinite medium: numerical and experimental investigation. *Physics in Medicine and Biology* 45(5) 1359-73.
- Martelli, F. and G. Zaccanti. 2007. Calibration of scattering and absorption properties of a liquid diffusive medium at NIR wavelengths - CW method. *Optics Express* 15(2) 486-500.
- Martí-López, L., J. Bouza-Domínguez and J. C. Hebden. 2004. Interpretation of the failure of the time-independent diffusion equation near a point source. *Optics Communications* 242 23-43.
- McGlone, V. A., P. Martinsen, R. Künnemeyer, R. Jordan and B. Cletus. 2007. Measuring optical temperature coefficients of Intralipid®. *Physics in Medicine and Biology* 52(9) 2367-78.
- Michels, R., F. Foschum and A. Kienle. 2008. Optical properties of fat emulsions. *Optics Express* 16(8) 5907-25.

-
- Mie, G. 1908. Contributions to the optics of turbid media, particularly of colloidal metal solutions. *Ann. Phys. (Leipzig)* 25(3) 377-445.
- Millikan, G. A. 1942. The Oximeter, an instrument for measuring continuously the oxygen saturation of arterial blood in man. *Review of Scientific Instruments* 13 434-44.
- Morgan, S. P. and K. Y. Yong. 2001. Elimination of amplitude-phase crosstalk in frequency domain near-infrared spectroscopy. *Review of Scientific Instruments* 72(4) 1984-7.
- Mourant, J. R., T. Fuselier, J. Boyer, T. M. Johnson and I. J. Bigio. 1997. Predictions and measurements of scattering and absorption over broad wavelength ranges in tissue phantoms. *Applied Optics* 36(4) 949-57.
- Mudgett, P. S. and L. W. Richards. 1971. Multiple Scattering Calculations for Technology. *Applied Optics* 10(7) 1485-502.
- Nichols, M. G., E. L. Hull and T. H. Foster. 1997. Design and testing of a white-light, steady-state diffuse reflectance spectrometer for determination of optical properties of highly scattering systems. *Applied Optics* 36(1) 93-104.
- O'Leary, M. A., D. A. Boas, B. Chance and A. G. Yodh. 1992. Refraction of diffuse photon density waves. *Physical Review Letters* 69(18) 2658-61.
- Palmer, G. 2003. Report on the practical Semester 2003. *The University of Waikato* Hamilton, NZ 1-19.
- Palmer, G. M. and N. Ramanujam. 2006. Monte Carlo-based inverse model for calculating tissue optical properties. Part I: Theory and validation on synthetic phantoms. *Applied Optics* 45(5) 1062-71.
- Palmer, G. M., C. Zhu, T. M. Breslin, F. Xu, K. W. Gilchrist and N. Ramanujam. 2006. Monte Carlo-based inverse model for calculating tissue optical properties. Part II: Application to breast cancer diagnosis. *Applied Optics* 45(5) 1072-8.
- Palmer, K. F. and D. Williams. 1974. Optical properties of water in the near infrared. *Journal of the Optical Society of America A* 64 1107-10.
- Pellion, D., V. Borrel, D. Esteve, F. Therez, F. Bony, A. R. Bazer-Bachi and J. P. Gardou. 2006. APD photodetectors in the Geiger photon counter mode. *Nuclear Instruments and Methods in Physics Research A* 567 41-4.
- Pham, T. H., O. Coquoz, J. B. Fishkin, E. Anderson and B. J. Tromberg. 2000. Broad bandwidth frequency domain instrument for quantitative tissue optical spectroscopy. *Review of Scientific Instruments* 71(6) 2500-13.
- Pifferi, A., A. Torricelli, A. Bassi, P. Taroni, R. Cubeddu, H. Wabnitz, D. Grosenick, M. Möller, R. Macdonald, J. Swartling, et al. 2005. Performance

- assessment of photon migration instruments: the MEDPHOT protocol. *Applied Optics* 44(11) 2104-14.
- Pifferi, A., A. Torricelli, P. Taroni, D. Comelli, A. Bassi and R. Cubeddu. 2007. Fully automated time domain spectrometer for the absorption and scattering characterization of diffusive media. *Review of Scientific Instruments* 78(5) 053103-10.
- Pogue, B. W. and M. S. Patterson. 1994. Frequency-domain optical absorption spectroscopy of finite tissue volumes using diffusion theory. *Physics in Medicine and Biology* 39 1157-80.
- Pogue, B. W. and M. S. Patterson. 2006. Review of tissue simulating phantoms for optical spectroscopy, imaging and dosimetry. *Journal of Biomedical Optics* 11(4) 041102-1-16.
- Prahl, S. 1998. Tabulated Molar Extinction Coefficient for Hemoglobin in Water. (accessed <http://omlc.ogi.edu/spectra/hemoglobin/summary.html> June 2009).
- Prahl, S. A., M. Keijzer, S. L. Jacques and A. J. Welch. 1989. A monte carlo model of light propagation in tissue. In *Dosimetry of Laser Radiation in Medicine and Biology*: SPIE Institute Series.
- Qin, J. and R. Lu. 2008. Measurement of the optical properties of fruits and vegetables using spatially resolved hyperspectral diffuse reflectance imaging technique. *Postharvest Biology and Technology* 49 355-65.
- Raman, C. V. and N. S. N. Nath. 1935. The diffraction of light by high frequency sound waves: Part I. *Proceedings of the Indian Academy of Sciences* 2 406-12.
- Renker, D. 2006. Geiger-mode avalanche photodiodes, history, properties and problems. *Nuclear Instruments and Methods in Physics Research A* 567 48-56.
- Reynolds, L., C. Johnson and A. Ishimaru. 1976. Diffuse reflectance from a finite blood medium: applications to the modeling of fiber optic catheters. *Applied Optics* 15(9) 2059-67.
- Rinzema, K., L. H. P. Murrer and W. M. Star. 1998. Direct experimental verification of light transport theory in an optical phantom. *Journal of Optical Society of America A* 15(8) 2078-88.
- Rogers, D. W. O. 2006. Fifty years of Monte Carlo simulations for medical physics. *Physics in Medicine and Biology* 51(13) R287-R99.
- Rolfe, P. 2000. In vivo near-infrared spectroscopy. *Annual Review of Biomedical Engineering* 2 715-54.
- Sardar, D. K., R. M. Yow and R. J. Thomas. 2006. Experiments, Computation, and Modeling for Temperature Dependence of Absorption, Scattering, Reflection, Transmission, and Index of Refraction of Optical Radiation in Biological Tissues. *Technical Report*.

-
- Sassaroli, A. and S. Fantini. 2004. Comment on the modified Beer-Lambert law for scattering media. *Physics in Medicine and Biology* 47(7) N255-N7.
- Sassaroli, A., F. Martelli, D. Imai and Y. Yamada. 1999. Study on the propagation of ultra-short pulse light in cylindrical optical phantoms. *Physics in Medicine and Biology* 44(11) 2747-63.
- Schmitt, J. M., A. Kniittel and J. R. Knutson. 1992. Interference of diffusive light waves. *Journal of Optical Society of America A* 9(10) 1832-43.
- Schweiger, M. and S. R. Arridge. 1997. The finite-element method for the propagation of light in scattering media: Frequency domain case. *Medical Physics* 24(6) 895-902.
- Schweiger, M., S. R. Arridge, M. Hiraoka and D. T. Delpy. 1995. The finite element method for the propagation of light in scattering media: Boundary and source conditions. *Medical Physics* 22(11) 1779-92.
- Scofield, J. H. 1994. Frequency-domain description of a lock-in amplifier. *American Journal of Physics* 62(2) 129-33.
- Scott, C. R. 1992. *Field Theory of Acousto-Optic Signal Processing Devices*. Norwood, MA: Artech House
- Segelstein, D. J. 1981. The complex refractive index of water. PhD thesis, University of Missouri, Kansas City.
- Seo, I., C. K. Hayakawa and V. Venugopalan. 2008. Radiative transport in the delta-P1 approximation for semi-infinite turbid media. *Medical Physics* 35(2) 681-93.
- Sevick-Muraca, E. M., E. Kuwana, A. Godavarty, J. P. Houston, A. B. Thompson and R. Roy. 2003. Near-infrared fluorescence imaging and spectroscopy in random media and tissues. In *Biomedical photonics handbook*, ed. T. Vo-Dinh. Boca Raton, Florida: CRC Press.
- Shen, H., W. Cong, X. Qian, K. Durairaj and G. Wang. 2007. Numerical study on the validity of the diffusion approximation for computational optical biopsy. *Journal of Optical Society of America A* 24(2) 423-9.
- Shore, S. N. 2002. Blue Sky and Hot Piles: The Evolution of Radiative Transfer Theory from Atmospheres to Nuclear Reactors. *Historia Mathematica* 29(4) 463-89.
- Simon, R. E. and B. F. Williams. 1968. Secondary-Electron Emission. *IEEE Transactions on Nuclear Science* 15(3) 167-70.
- Smith, R. C. and K. S. Baker. 1981. Optical properties of the clearest natural waters (200-800 nm). *Applied Optics* 20(2) 177-84.

- Spichtig, S., R. Hornung, D. W. Brown, D. Haense and M. Wolf. 2009. Multifrequency frequency-domain spectrometer for tissue analysis. *Review of Scientific Instruments* 80(2) 024301-7.
- Spinelli, L., F. Martelli, A. Farina, A. Pifferi, A. Torricelli, R. Cubeddu and G. Zaccanti. 2007. Calibration of scattering and absorption properties of a liquid diffusive medium at NIR wavelengths. Time-resolved method. *Optics Express* 15(11) 6589-603.
- Splinter, R. and B. A. Hooper. 2007. Numerical and Deterministic Methods in Light-Tissue Interaction Theory. In *An introduction to biomedical optics* 181-218. Boca Raton Taylor & Francis.
- Sudiarta, I. W. and P. Chylek. 2001. Mie-scattering formalism for spherical particles embedded in an absorbing medium *Journal of Optical Society of America A* 18(6) 1275-8.
- Sun, Z., Y. Huang and E. M. Sevick-Muraca. 2002. Precise analysis of frequency domain photon migration measurement for characterization of concentrated colloidal suspensions. *Review of Scientific Instruments* 73(2) 383-93.
- Svensson, J., A. Johansson, K. Svanberg and S. Andersson-Engels. 2005. Tissue temperature monitoring during interstitial photodynamic therapy. *Proceedings of SPIE* 5698 126-36.
- Swartling, J., J. S. Dam and S. Andersson-Engels. 2003. Comparison of Spatially and Temporally Resolved Diffuse-Reflectance Measurement Systems for Determination of Biomedical Optical Properties. *Applied Optics* 42(22) 4612-20.
- Tam, W. G. and A. Zardecki. 1982. Multiple scattering corrections to the Beer-Lambert law. 1: Open detector. *Applied Optics* 21(13) 2405-12.
- Tøgersen, G., T. Isaksson, B. N. Nilsen, E. A. Bakker and K. I. Hildrum. 1999. On-line NIR analysis of fat, water and protein in industrial scale ground meat batches. *Meat Science* 51 97-102.
- Tromberg, B. J., O. Coquoz, J. B. Fishkin, T. Pham, E. R. Anderson, J. Butler, M. Cahn, J. D. Gross, V. Venugopalan and D. Pham. 1997. Non-invasive measurements of breast tissue optical properties using frequency-domain photon migration. *Philosophical Transactions of the Royal Society B* 352 661-8.
- Tromberg, B. J., N. Shah, R. Lanning, A. Cerussi, J. Espinoza, T. Pham, L. Svaasand and J. Butler. 2000. Non-Invasive In Vivo Characterization of Breast Tumors Using Photon Migration Spectroscopy. *Neoplasia* 2(1-2) 26-40.
- Tromberg, B. J., L. O. Svaasand, T. T. Tsay and R. C. Haskell. 1993. Properties of photon density waves in multiple-scattering media. *Applied Optics* 32(4) 607-16.
- Tuchin, V. V. 2005. Optical clearing of tissues and blood using the immersion method. *Journal of Physics D: Applied Physics* 38 2497-518.

-
- van de Hulst, H. C. 1981. *Light Scattering by Small Particles*. New York: Dover
- van Staveren, H. J., C. J. M. Moes, J. van Marle, S. A. Prahl and M. J. C. van Gemert. 1991. Light scattering in Intralipid-10% in the wavelength range of 400-1100 nanometers. *Applied Optics* 30(31) 4507-14
- Vargas, W. E. and G. A. Niklasson. 1997. Applicability conditions of the Kubelka-Munk theory. *Applied Optics* 36(22) 5580-6.
- Wang, L. H., S. L. Jacques and L. Q. Zheng. 1995. MCML - Monte Carlo modeling of photon transport in multi-layered tissues. *Computer Methods and Programs in Biomedicine* 47 131-46.
- Wang, L. V. and H.-i. Wu. 2007. *Biomedical Optics: Principles and Imaging*. Hoboken, N.J: Wiley
- Welch, A. J. and M. J. C. vanGemert. 1995. *Optical-Thermal Response of Laser-Irradiated Tissue*. New York: Plenum Press
- Weng, J., M. Z. Zhang, K. Simons and B.Chance. 1991. Measurement of biological tissue metabolism using phase modulation spectroscopic technology. *Proceedings of SPIE* 1431 161-72.
- Whateley, T. L., G. Steele, J. Urwin and G. A. Smail. 2008. Particle size stability of Intralipid and mixed total parenteral nutrition mixtures. *Journal of Clinical Pharmacy and Therapeutics* 9(2) 113-26.
- Williams, R. 1960. Becquerel Photovoltaic Effect in Binary Compounds. *The Journal of Chemical Physics* 32(5) 1505-14.
- Wilson, B. C. and M. S. Patterson. 2008. The physics, biophysics and technology of photodynamic therapy. *Physics in Medicine and Biology* 53(9) R61-R109.
- Xu, H., T. J. Farrell and M. S. Patterson. 2006. Investigation of light propagation models to determine the optical properties of tissue from interstitial frequency domain fluence measurements. *Journal of Biomedical Optics* 11(4) 041104-18.
- Xu, H. and M. S. Patterson. 2006. Determination of the optical properties of tissue simulating phantoms from interstitial frequency domain measurements of relative fluence and phase difference. *Optics Express* 14(14) 6485-501.
- Xu, M. and L. V. Wang. 2006. Photoacoustic imaging in biomedicine. *Review of Scientific Instruments* 77(4) 041101-22.
- Yang, L. and B. Kruse. 2004. Revised Kubelka-Munk theory. I. Theory and application. *Journal of Optical Society of America A* 21(10) 1933-41.
- Yang, L. and S. J. Miklavcic. 2005. Revised Kubelka-Munk theory. III. A general theory of light propagation in scattering and absorptive media. *Journal of Optical Society of America A* 22(9) 1866-73.

- Yokoyama, S., A. Okamoto, T. Araki and N. Suzuki. 1995. Examination to eliminate undesirable phase delay of an avalanche photodiode (APD) for intensity-modulated light. *Review of Scientific Instruments* 66(11) 5331-6.
- You, J. S., C. K. Hayakawa and V. Venugopalan. 2005. Frequency domain photon migration in the δ -P1 approximation: Analysis of ballistic, transport, and diffuse regimes. *Physical Review E* 72(2) 021903 - 13.
- Zaccanti, G., S. D. Bianco and F. Martelli. 2003. Measurements of optical properties of high-density media. *Applied Optics* 42(19) 4023-30.
- Zaoui, W. S., H.-W. Chen, J. E. Bowers, Y. Kang, M. Morse, M. J. Paniccia, A. Pauchard and J. C. Campbell. 2009. Frequency response and bandwidth enhancement in Ge/Si avalanche photodiodes with over 840GHz gain-bandwidth-product. *Optics Express* 17(15) 12641-9.
- Zhao, Z. and R. Myllylä. 2001. Photo acoustic blood glucose and tissue measurements based on optical scattering effect. *Proceedings of SPIE* 4707(153-157).
- Zhu, S. 1990. Birefringent filter with tilted optic axis for tuning dye lasers: theory and design. *Applied Optics* 29(3) 410-5.